Chapter 2

Spatiotemporal Calibration of Electron Microscopes

Abed Malti

Additional information is available at the end of the chapter

http://dx.doi.org/10.5772/61947

Abstract

This chapter presents a method of calibration for scanning electron microscopes (SEMs). The described calibration method is a twofold step. The first step evaluates the dynamical drift parameters. The second step estimates the parameters of the geometric projection and the static distortion. Both steps process the calibration parameters across the range of magnification scales, thanks to a representation with partial differential equations. The chapter is provided with an example of calibration of the JEOL JSM 820 and an example of application in metrology. The presented method is not the unique way of calibrating an SEM and can be a good start to inspire other methods of calibration.

Keywords: Calibration of microscopes, Drift calibration, Distortion calibration, Projection calibration

1. Introduction

SEM calibration is required in many applications: 3D reconstruction of microscale and nanoscale specimens [1–3], deformation measurement [4], nanomaterial tracking [3, 5, 6], positioning and handling [7], mobile robot positioning [8], etc. The image acquisition process of a standard SEM has usually three stages: *(i)* The conditioning of the electron beam from the electron gun to the area of the observed specimen. In this stage, the electron beam goes through condensation process by magnetic lenses and a final deflection coils that move the beam in a raster fashion over a rectangular area of the specimen. *(ii)* The interaction between the deflected beam and the observed object, usually called specimen. When the deflected beam hits the specimen, it results in an emission of energy that can be amplified and detected by specific electronic detectors. *(iii)* The conversion of the emitted energy to pixel intensity. In this process, each position of the deflected beam that hits the specimen

corresponds to a pixel in the image. An appropriate transform between the detected energy and the gray-scale values is then applied to obtain the corresponding pixel intensity. In the case of a distortion-free imaging process, the obtained image would be the result of the projection of the 3D rastered area onto the image plane. According to an increasing magnification scale, this projection goes from the perspective for small magnification to the weak perspective for average magnification and ends up with orthographic projection with high magnification. However in reality, stages *(i)* and *(ii)* bring some distortion artifacts to these projection transforms. Indeed, the hysteresis effect of the magnetic coils distorts the deflected beam during the observation process. These distortions cause some drifts of the pixels from their original projected positions. For instance, these drifts can exceed tenth of pixels (hundreds of microns) in an hour at 10 k× magnification with a JEOL JSM 820. These drifts can be modeled as a combination of static (spatial) and dynamic (spatiotemporal) mappings which will be composed with the projection mapping to obtain the acquired image.

State-of-the-art studies have established that dynamical drift is time dependent and magnification dependent but space independent [9]. Among estimation methods, the drift was estimated in full field based on digital image correlation (DIC) in [9–12]. In [13], it was estimated in the frequency domain using FFT. The trajectory flow of the drift over time has been modeled using of B-spline curve fitting [9]. A second-order dynamical system embedded in a Kalman filter was tested and validated to model a thermal drift calibration in scanning probe microscopy [14]. The spatial calibration which involves both static distortion calibration and projection calibration was modeled similarly as with classic optical imaging systems [15, 16]. Some state-of-the-art works assumed a non-radial behavior of the static distortion and address this problem using B-splines to fit the spatial evolution of distortion and then warp it to a 3D-to-2D projection. Other works considered a perspective projection in the case of low magnifications (up to 5 k×) and an orthographic projection in the case of high magnifications (more than 5 k×) [1, 9, 17, 18].

In this chapter, we go through an empirical calibration method to fit a system of partial differential equations (PDEs). The partial derivatives of the calibration parameters are estimated with respect to time and magnification. These parameters include the amount of drift in pixel, the amount of static distortion, the focal length, and the principal point. This modeling provides a systematic and flexible solution to this calibration problem. It allows us to smoothly update calibration parameters across the variation of magnification scales and to continuously compensate pixel drifts during experiments.

1.1. Notations

Two-dimensional points in homogeneous coordinates are denoted by symbols in typewriter font (e.g., $\mathtt{u} = (u_x, u_y, 1)^T$). Three-dimensional points are indicated by plain letters (e.g., $\mathbf{C} = (C_x, C_y, C_z)^T$). Matrices are denoted by uppercase sans serif font (e.g., A). This notation is also adopted for n-dimensional vectors. However, vectors providing a direction in 3D are represented using plain lowercase topped by an arrow (e.g., $\vec{l}$). For convenience, and given two 3×1 vectors $\vec{l}$ and $\vec{m}$, the dot product is indicated either using $< ., . >$ or using regular matrix/vector multiplication (e.g., $< \vec{l}, \vec{m} > = \vec{l}^{\,\mathsf{T}}\, \vec{m}$), and the cross product is carried either using the symbol $\times$ or using the skew symmetric matrix (e.g., $\vec{l} \times \vec{m} = [\vec{l}]_\times\, \vec{m}$). $||.||_2$ denotes the vector 2-norm in any real vector space $\mathbb{R}^n$ of finite dimension n. The symbols μm and nm designate, respectively, micrometer and nanometer unit distances. The abbreviation "w.r.t." stands for "with respect to."

http://dx.doi.org/10.5772/61947

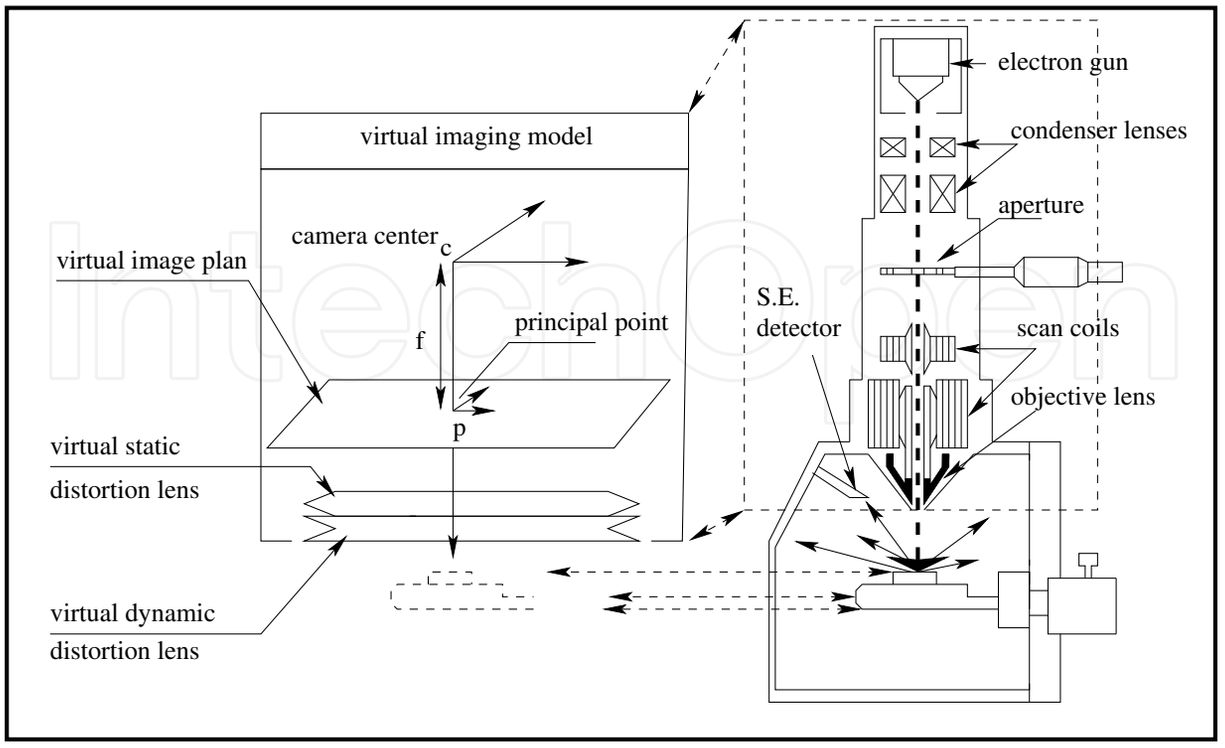

Figure 1. Scanning electron microscope with the corresponding imaging model.

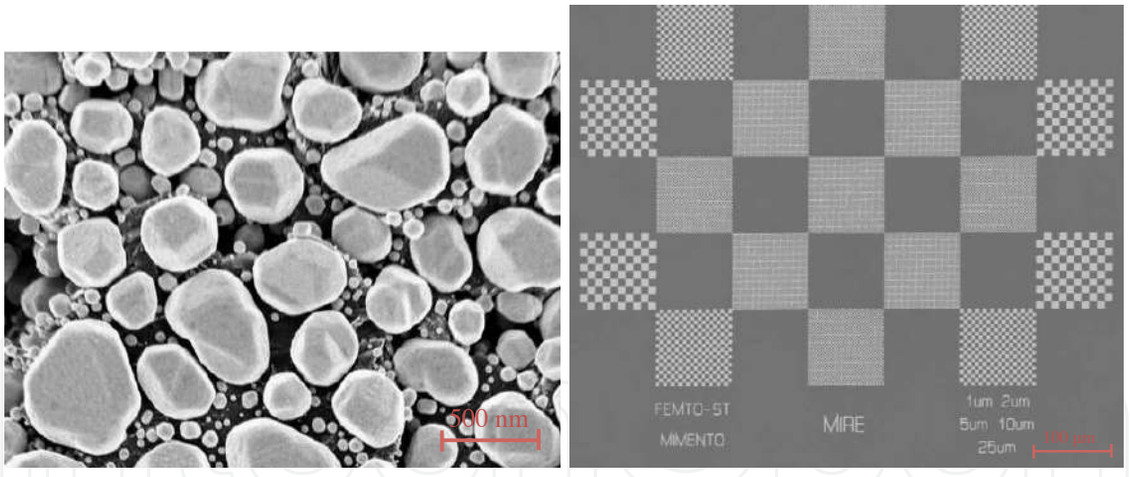

Figure 2. Left figure: Gold-on-carbon specimen. Right figure: Multi-scale calibration grid designed at FEMTO-ST lab.

2. Formulation of the imaging model

The imaging model of a SEM is the composition of three mappings [19, 20] which are depicted in Figure 1:

1. A pixel-drift mapping from drifted to non-drifted image. It is both magnification and time dependent. To experimentally quantify this drift, we acquire images of a usual specimen (see Figure 2 left) at different times and for different magnifications. Correlation in the

frequency domain of successive pairs of images is used to estimate the drift [13]. The dynamic of the drift with respect to time t and magnification g is modeled by two partial differential equations (PDEs) whose coefficients are estimated by means of the principal differential analysis (PDA) approach [21].

2. A spatial distortion mapping which is magnification dependent. It may concern both radial and tangential distortions [22]. In this chapter, we consider only radial distortions.
3. A 3D-to-2D projection mapping. The type of projection to be applied depends on the magnification. For low magnifications, it can be considered as central perspective projection. But for magnifications above 1000×, it should be interpreted as parallel projective [9]. A specific calibration specimen is used [20]; see Figure 2 right. It contains squares of various sizes, enabling the calibration over a wide range of magnification. Images of this specimen are acquired for various magnifications and poses. An image-centered radial and tangential model that expresses the distorted points w.r.t. the undistorted points is developed. PDEs with respect to magnification of the evolution of the static distortion parameters are established. The estimation of the projection matrix where the magnification factor is embedded is proposed. A bundle-adjustment optimization [23] of the reprojection error between 3D points and their corresponding image pixels allows us to refine the estimated parameters.

Mathematically speaking, the above description can be formalized as:

$$\hat{\mathbf{q}} = \mathtt{T}^{d}_{t,g}(\mathtt{T}^{s}_{g}(\Pi_g\,\mathbf{Q})), \tag{1}$$

where $\mathbf{Q}$ is a 3D point of the observed specimen. $\hat{\mathbf{q}}$ is the corresponding acquired image pixel. $\mathtt{T}^{d}_{t,g} : \mathbb{R}^2 \to \mathbb{R}^2$ and $\mathtt{T}^{s}_{g} : \mathbb{R}^2 \to \mathbb{R}^2$ are two-dimensional mappings (images x-axis and y-axis) which respectively represent the dynamical drift and the static distortion. Π_g is the 3D-to-2D projective mapping. To retrieve a 3D ray incident from a 3D point of scanned scene, the corresponding pixel is first corrected from the drift effect; then it is statically undistorted and finally back-projected. In the following, we show how to estimate these mappings. Also, we provide examples of application on a JEOL JSM 820 SEM in secondary electron (SE) imaging mode for time ranging from 0 to 30 min and magnification ranging from 100× to 10 k×.

3. Magnification-smooth dynamical drift modeling and calibration

3.1. Drift modeling

The dynamical drift of an image frame at a time t can be represented as a trajectory flow $(x(t), y(t))^T$ of pixels with respect to time:

$$\hat{I}_t(x_0 + x(x_0, y_0, t), y_0 + y(x_0, y_0, t)) = I_t(x_0, y_0), \tag{2}$$

where $\hat{I}_t$ is the intensity of the acquired image which is submitted to drift. I_t is the ideal image without drift effects. $(x_0, y_0)^T$ is the non-drifted pixel position and $(x(t), y(t))^T$ is the amount of drift. As described previously, SEM images are produced pixel by pixel with

http://dx.doi.org/10.5772/61947

a rastering process. An exact identification of the drift should be to follow the amount of drift flow in a pixel-wise manner $(x(x_0,t),y(y_0,t))^T$. In [10, 19], a full-field correction of the image drift is proposed. For SEMs where the acquisition time t_F of one frame is faster than the pixel-wise dynamic of the drift, it can be assumed as being a global pixel drift between frames especially at low magnification (less than 5000×). This global drift displacement can be easily assessed using image cross-correlation computation between frames. In this case, the first acquired image is considered as the ideal one at $t = 0$. Taking into account this assumption, equation (2) can be reconsidered as

$$\hat{I}_0(x_0,y_0) = I_0(x_0,y_0), \tag{3}$$

$$\hat{I}_t(x_0+\delta x(t), y_0+\delta y(t)) = \hat{I}_{t+1}(x_0,y_0). \tag{4}$$

From now on, we drop the hat symbol on the notation of acquired image unless it is worth to mention it. If two successive image frames I_{t-1} and I_t contain the same view at different pixel positions, the cross-correlation integral has a large value at the vector $(\delta x(t),\delta y(t))^T$ which corresponds to the drift of the features.

$$(\delta x(t),\delta y(t)) = \arg\max_{x,y}\left\{\mathcal{C}_{I_{t-1},I_t}(x,y)\right\}, \tag{5}$$

with

$$\mathcal{C}_{I_{t-1},I_t}(x,y) = \sum_i\sum_j I_{t-1}(i,j)\, I_t(i+x,j+y), \tag{6}$$

where $i+x$, $j+y$, x, and y are pixel coordinates running over the image domain. According to [10], at magnification higher than 5000×, the dynamical drift varies even during the scanning process. It showed that the amount of drift variation within an image ranged from 0.3 to 0.9 pixels at 10 k×. In this chapter, the use of an EKF allows us to face this amount of single pixel drift by assuming a Gaussian noise of 1 pixel in the state model [19].

For a given magnification range from g_0 to g_f with a step G and a time interval from t_0 to t_f with an image acquisition at each sample time T, the image drifts are estimated as follows:

for $g = g_0$ *to* g_f *with step* G **do**
  for $t = t_0$ *to* t_f *with step* T **do**
    acquire images of the specimen pattern;
    estimate drift elements δx and δy between frame t_0 and current frame;
  end
end

Algorithm 1: Processing of Drift Data.

At the end of this step, two data matrices $\Delta_x(t,g)$ and $\Delta_y(t,g)$ of $\frac{t_f-t_0}{T}$ rows and $\frac{g_f-g_0}{G}$ columns are obtained. The next step is to use this data drift and PDA to evaluate the dynamics of the drift trajectory functions $\Delta_x(t,g)$ and $\Delta_y(t,g)$.

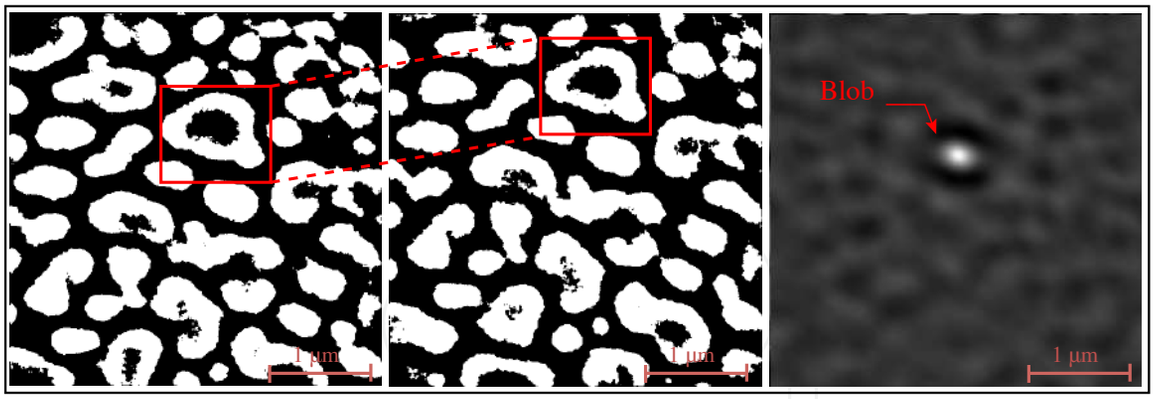

Figure 3. An example of drift behavior. The image size is of 512 × 512 pixels. Left figure: The initial figure. Middle figure: After 15 min, the enclosed feature and all the image features have moved. Right figure: The results of the intercorrelation between the two images. The distance between the blob and the center of the image represents the amount of drift.

3.2. Estimating PDEs of the dynamical drift

When describing PDA for linear PDE models, Ramsay and Silverman [24] view the system dynamics as a linear differential operator (LDO) acting upon the process variables. For example, let $\Delta_x(t, g_i)$ be the observed data drift which varies w.r.t. the time parameter t at sampled time T from $t = t_0$ until $t = t_f$. Let $D^m x_i$ be the m^{th} derivative of the function $\Delta_x(t, g)$ w.r.t. t. The function $\Delta_x(t, g)$ is assumed to be square integrable. In this chapter, we consider the identification of a second-order LDO which determines the first (speed)- and second (acceleration)-order parameters of the dynamic of the drift [19]:

$$L = w_0^x + w_1^x D + D^2 \tag{7}$$

that comes as close as possible to satisfy the homogeneous linear differential equation:

$$L \,.\, \Delta_x = 0 \tag{8}$$

In other words, if we estimate the first and second derivatives $D\Delta_x$ and $D^2\Delta_x$ of $\Delta_x(t, g_i)$ w.r.t. time using finite differences, we wish the operator L to annihilate the drift function $\Delta_x(t, g)$ as nearly as possible. Thus, we seek a linear differential equation model so that our data satisfies:

$$D^2\Delta_x = -w_0^x(g_i)\,\Delta_x - w_1^x(g_i) D\,\Delta_x \tag{9}$$

to the best possible degree of approximation. To carry out PDA, we adopt a least squares approach to the fitting of the differential equation model. The fitting criterion is to minimize, over $\left(w_0^x(g_i)\ w_1^x(g_i)\right)$, the sum of squared norms:

$$J = \left\| \mathsf{A} \begin{pmatrix} w_0^x(g_i) \\ w_1^x(g_i) \end{pmatrix} + \mathsf{b} \right\|^2 \tag{10}$$

http://dx.doi.org/10.5772/61947

where

$$\mathsf{A} = \begin{pmatrix} \Delta_x(t_0, g_i) & D\Delta_x(t_0, g_i) \\ \vdots & \vdots \\ \Delta_x(t_f, g_i) & D\Delta_x(t_f, g_i) \end{pmatrix}, \ \mathsf{b} = \begin{pmatrix} D^2\Delta_x(t_0, g_i) \\ \vdots \\ D^2\Delta_x(t_f, g_i) \end{pmatrix} \tag{11}$$

A is a matrix of $\frac{t_f - t_0}{T}$ rows and 2 columns and is always of rank 2. b is a vector of $\frac{t_f - t_0}{T}$ elements. The solution of such an overdetermined least square problem is given as

$$\begin{pmatrix} w_0^x(g_i) \\ w_1^x(g_i) \end{pmatrix} = (\mathsf{A}^\top \mathsf{A})^{-1} \mathsf{A}\mathsf{b} \tag{12}$$

Solving equation (12) for each $g_i = g_0,\ g_0 + G, \ldots, g_f$ gives rise to the following weight matrix:

$$\mathsf{W} = \begin{pmatrix} w_0^x(g_0) & w_0^x(g_0 + G) & \cdots & w_0^x(g_f) \\ w_1^x(g_0) & w_1^x(g_0 + G) & \cdots & w_1^x(g_f) \end{pmatrix} \tag{13}$$

W is a matrix of 2 rows and $\frac{g_f - g_0}{G}$ columns. The first row represents a discrete sampling of the function $w_0^x(g)$ and the second row a discrete sampling of $w_1^x(g)$. Once again, computing the first- and second-order derivatives of the first and the second row using finite differences on the variation of the magnification gives rise to two differential equations, driving w_0^x and w_1^x variation w.r.t. magnification:

$$D_g^2 w_i = -\alpha_{0i} w_i - \alpha_{1i} D_g w_i, \quad i = 0, 1 \tag{14}$$

The two real valued vectors $(\alpha_{0i}\ \alpha_{1i})$, $i = 0, 1$ are estimated as in equation (12) after constructing the corresponding matrix A and vector b by using matrix W, the first and second finite differences of each row w.r.t. g. Equation (14) becomes then a PDE of second order that can be easily solved.

Henceforth, the differential equation related to drift function Δ_x can be expressed w.r.t. smooth magnification-dependent weight functions:

$$D^2\Delta_x = -w_0^x(g)\,\Delta_x - w_1^x(g) D\,\Delta_x, \quad g \in [g_0, g_f] \tag{15}$$

Finally, equation (15) can be solved as a second-order PDE giving rise to a smooth drift function $\Delta(t, g)$. The development conducted to represent Δ_x can be easily followed to represent Δ_y:

$$D^2\Delta_y = -w_0^y(g)\,\Delta_y - w_1^y(g) D\,\Delta_y, \quad g \in [g_0, g_f] \tag{16}$$

In order to take into account the noise in the data estimation and the finite differences computation, we choose to embed the differential equations (15) and (16) related to Δ_x and Δ_y in an EKF using a state modeling of the drift function.

3.3. Embedding PDEs of the drift in an EKF

If we assume that $x(g,t)$ and $y(g,t)$ are corrupted by a zero mean Gaussian noise $\omega_x(g,t)$ and $\omega_y(g,t)$ with covariance $\mathsf{Q}_x(g)$ and $\mathsf{Q}_y(g)$, then the stochastic state model can be written as

$$\begin{aligned} \mathsf{x}(g,t+T) &= \underbrace{\begin{pmatrix} 0 & 1 \\ -w_0^x(g) & -w_1^x(g) \end{pmatrix}}_{\mathsf{A}_x(g)} \mathsf{x}(g,t) + \omega_x(g,t) \\ x(g,t) &= \underbrace{\begin{pmatrix} 1 & 0 \end{pmatrix}}_{\mathsf{C}} \mathsf{x}(g,t) + \gamma_x(g,t) \end{aligned} \tag{17}$$

$$\begin{aligned} \mathsf{y}(g,t+T) &= \underbrace{\begin{pmatrix} 0 & 1 \\ -w_0^y(g) & -w_1^y(g) \end{pmatrix}}_{\mathsf{A}_y(g)} \mathsf{y}(g,t) + \omega_y(g,t) \\ y(g,t) &= \underbrace{\begin{pmatrix} 1 & 0 \end{pmatrix}}_{\mathsf{C}} \mathsf{y}(g,t) + \gamma_y(g,t) \end{aligned} \tag{18}$$

where $\mathsf{x}(g,t) = \big(x(g,t),\, v_x(g,t)\big)^\top$ and $\mathsf{y}(g,t) = \big(y(g,t),\, v_y(g,t)\big)^\top$ are the state vectors with v_x and v_y the speeds of the drift. The observed variable being the displacement flow $x(g,t)$ and $y(g,t)$, they are assumed to be corrupted by zero mean Gaussian noises $\gamma_x(g,t)$ and $\gamma_y(g,t)$ of covariances $\mathsf{R}_x(g)$ and $\mathsf{R}_y(g)$. This space model representation allows us to write the EKF time update and prediction equations:

$$\begin{aligned} &\hat{\mathsf{x}}(g,t+T|t) = \mathsf{A}_x(g)\hat{\mathsf{x}}(g,t+T|t) && \textbf{(predicted state drift)}, \\ &\mathsf{P}_x(g,t+T|t) = \mathsf{A}_x(g)\mathsf{P}_x(g,t|t)\mathsf{A}_x^\top(g) + \mathsf{Q}_x(g) && \textbf{(predicted covariance drift)}, \end{aligned} \tag{19}$$

$$\begin{aligned} &\mathsf{K}_x(g,t) = \mathsf{P}_x(g,t|t-T)\mathsf{C}\left(\mathsf{C}\mathsf{P}_x(g,t|t-T)\mathsf{C}^\top + \mathsf{R}_x(g,t)\right)^{-1} && \textbf{(optimal Kalman gain)}, \\ &\hat{\mathsf{x}}(g,t|t) = \hat{\mathsf{x}}(g,t|t-T) + \mathsf{K}_x(t)\left(\tilde{x}(g,t) - \mathsf{C}\hat{\mathsf{x}}(g,t|t-T)\right) && \textbf{(updated state drift)}, \\ &\mathsf{P}_x(g,t|t) = (\mathsf{I} - \mathsf{K}_x(t)\mathsf{C})\mathsf{P}_x(g,t|t-T) && \textbf{(updated covariance drift)}, \end{aligned} \tag{20}$$

The same EKF equations can be stated for the drift flow $y(g,t)$.

3.4. The multi-scale drift calibration algorithm

In summary, the multi-scale drift flow is characterized in both magnification axis and time axis. Therefore, using the PDA approach, the PDEs w.r.t. time and the PDEs w.r.t. magnification are assessed. Assume a calibration through the range $[g_0, g_f]$ of magnifications. A calibration pattern with random shapes is positioned upon the stage inside the chamber.

http://dx.doi.org/10.5772/61947

The scene is static, and a set of images are taken at each sample time T. The different steps of the dynamical drift calibration can be summarized in Algorithm 2.

Data: $\Delta_x(t,g),\ \Delta_y(t,g)$
for $g = g_0$ *to* g_f *with step* G **do**
  estimate $w_0^x(g_i)$, $w_1^x(g_i)$ with equation (10);
  estimate $w_0^y(g_i)$, $w_1^y(g_i)$ with equation (10);
end
estimate α_{00} and α_{10} as in equation (10);
estimate α_{01} and α_{11} as in equation (10);
embed equations (13) and (14) in an EKF as explained in Section 3.3;

Algorithm 2: Dynamical drift calibration

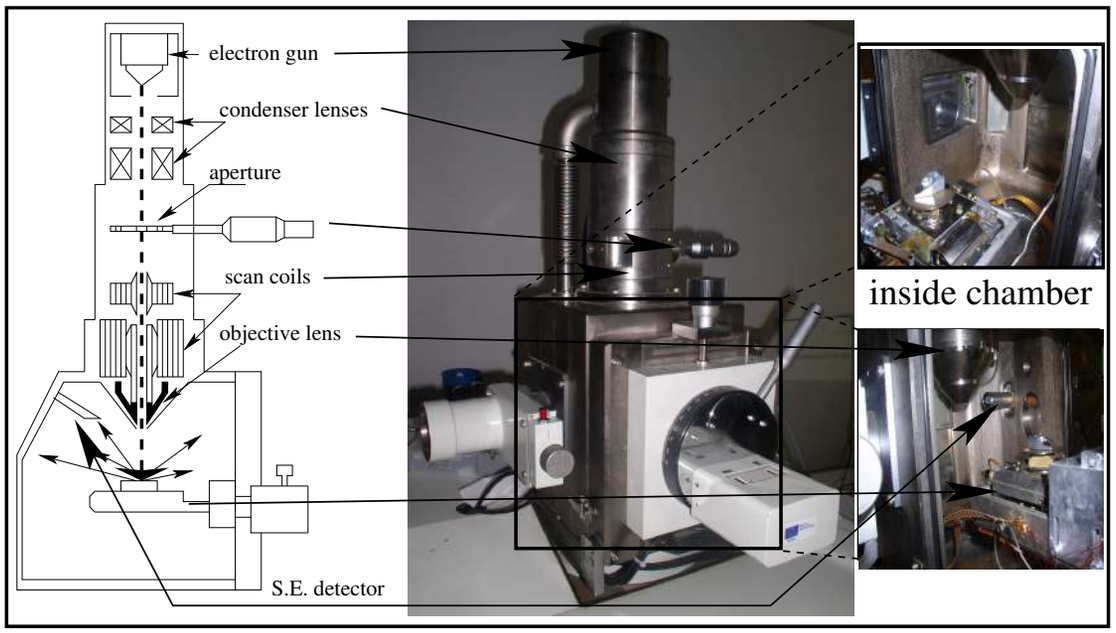

Figure 4. The *JSM 820* SEM manufactured by *JEOL*.

3.5. An example of dynamical drift calibration of the JEOL JSM 820

In this paragraph, we show how to use the method developed so far to calibrate the dynamical drift of the *JSM 820*, a SEM manufactured by *JEOL* (see Figure 4 for an illustration). The electron gun is equipped with a tungsten filament that can support from 0.3 kV up to 30 kV of acceleration voltage. The acquired images have a size of 512×512 pixels. The acceleration voltage is 15 kV, the scan rate is 15 frames per second, and the number of scans average is 8. The calibration is done for magnifications from $g_0 = 100\times$ up to $g_f = 30$ k$\times$.

3.5.1. Data drift estimation

To assess the pixel displacement between two frames, a specimen of particles of gold deposed above a layer of carbon is used (Figure 2 left). The particles are randomly positioned and have random shapes of different sizes so that the maximum of cross-correlation images of

such a sample can be calculated with less errors [10]. According to the cross-correlation theorem [25], the cross-correlation can be calculated using the Fourier transform. The widely used FFTW3 [26] library is applied for Fourier transform calculations. In order to improve the accuracy of the peak calculation, the cross-correlation is combined with the frequency filtering. A set of 55 images per magnification scale are taken every 30 s. The magnification scale is tuned from 100× until 10 k×. Some of these images are shown in Figure 5 with an illustration of the cross-correlation, resulting peaks between the first frame and the following frames. The pixel displacement vector of all images across time and magnification is depicted in Figure 6. It can be shown that at higher magnification, the drift is more important and can reach up to $(20, 90)^T$ pixel after 20 min of image acquisition. Now, the multi-scale calibration method of Section 3.4 can be applied. The first 30 images of each scale are used to construct the PDA model, and the 25 last images are used as validation data.

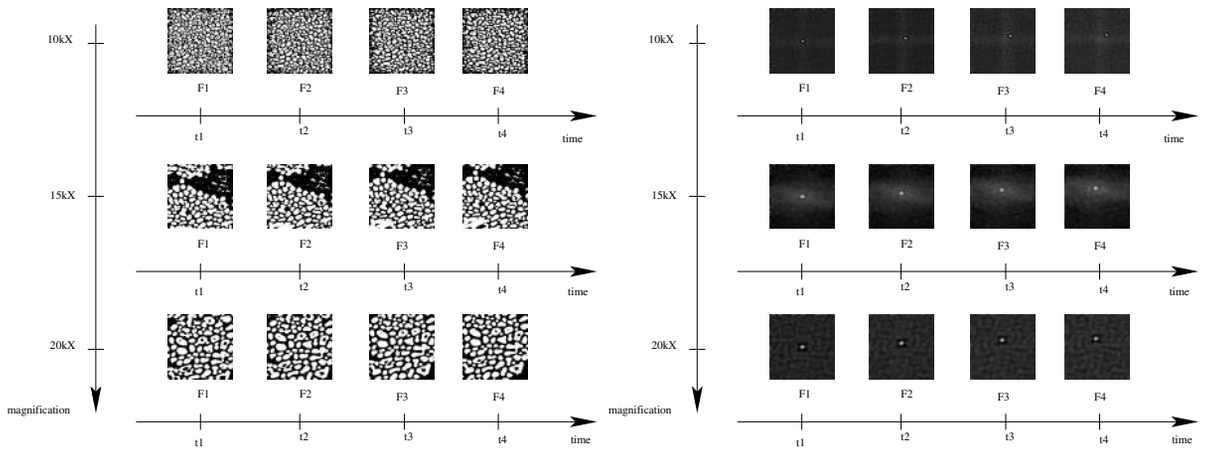

Figure 5. Left figure: A sample of images at four successive times along three magnification scales. Right figure: The bright point shows the maximum of the cross-correlation function between the first frame and the following frames. It can be seen that it moves after some acquisition time.

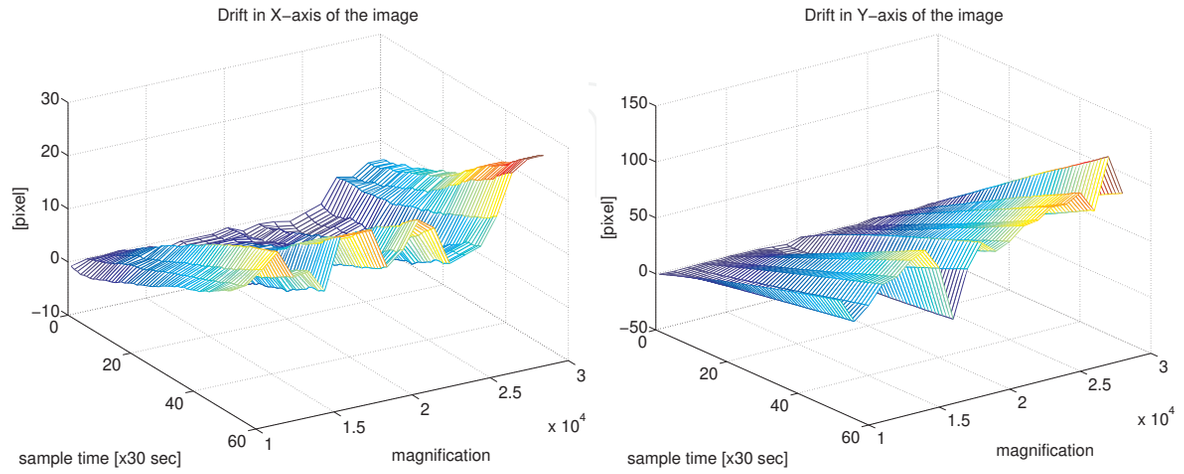

Figure 6. The pixel drift across time and magnification (left, image x-axis; right, image y-axis).

http://dx.doi.org/10.5772/61947

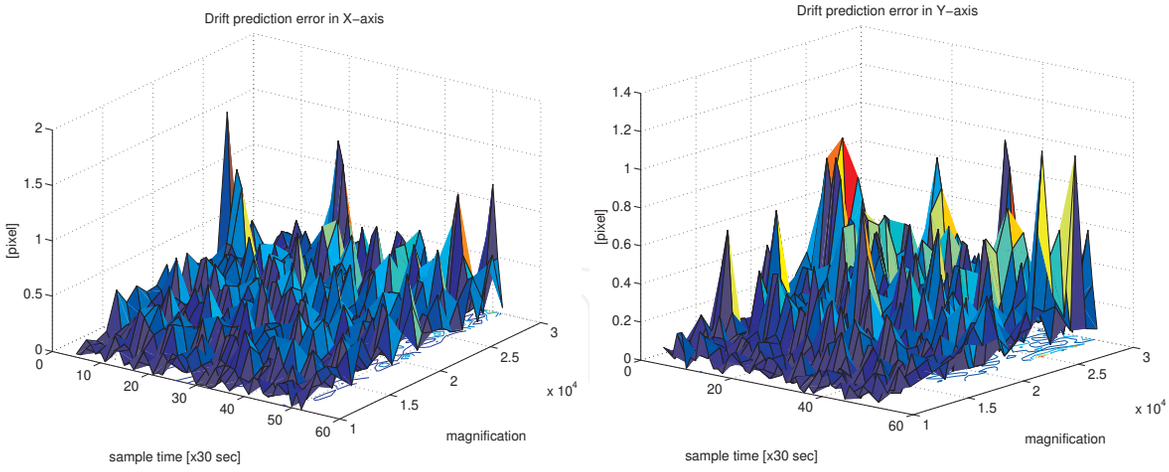

Figure 7. The Kalman filter prediction absolute error across time and magnification (left, image x-axis; right, image y-axis). Less than 0.9 pixel error in the x-axis and less than 1 pixel error in the y-axis. 0.28 pixel of global RMS error in the x-axis and 0.23 pixel of RMS error in the y-axis can be observed.

3.5.2. PDE estimation of the dynamical drift and EKF embedding

Using PDA, the estimated differential equations associated to w_0^x and w_1^x are

$$\begin{aligned} D_g^2 w_0^x &= -169.31\, w_0^x + 0.55 \cdot 10^{-2} D_g w_0^x \\ w_0^x(g_0) &= -1.27 \cdot 10^{-7}, \quad w_0^x(g_f) = -1.91 \cdot 10^{-5}, \end{aligned} \tag{21}$$

$$\begin{aligned} D_g^2 w_1^x &= 9.61\, 10^4\, w_1^x - 0.17 D_g w_1^x \\ w_1^x(g_0) &= 3.01 \cdot 10^{-4}, \quad w_1^x(g_f) = 0.04, \end{aligned} \tag{22}$$

Similarly, the weights $w_0^y(g)$ and $w_1^y(g)$ describing the ODE of $\Delta_y(t,g)$ are the solution of the two following differential equations:

$$\begin{aligned} D_g^2 w_0^y &= -169.31\, w_0^y + 0.0055 D_g w_0^y \\ w_0^y(g_0) &= -1.20 \cdot 10^{-6}, \quad w_0^y(g_f) = -1.44 \cdot 10^{-6}, \end{aligned} \tag{23}$$

$$\begin{aligned} D_g^2 w_1^y &= 9.61\, 10^4\, w_1^y - 0.17 D_g w_1^y \\ w_1^y(g_0) &= 0.16 \cdot 10^{-2}, \quad w_1^y(g_f) = 0.14 \cdot 10^{-2}, \end{aligned} \tag{24}$$

The PDA study of the collected data shows that the time dependence is more likely to be a second-order differential equation and so is for the magnification dependence. This order may not be accurate because of the noise in the data. Thus, to take into account this noise, the two dynamical models of equations (15) and (16) are embedded in an EKF. The Gaussian noise associated to the state model and observation of Δ_x and Δ_y has a zero mean and 0.25 pixels of standard deviation. The plots of the prediction error are shown in Figure 7. Less

than 0.9 pixel error in the x-axis and less than 1 pixel error in the y-axis can be observed. Also, 0.28 pixel of global RMS error in the x-axis and 0.23 pixel of RMS error in the y-axis can be observed.

4. Multi-scale static calibration

The multi-scale static calibration concerns the estimation of the static distortion parameters as well as the projection parameters. They are independent of time, but they are magnification dependent.

4.1. Static distortion calibration

In contrast with the dynamical drift, at low magnification, the static distortion is much more significant than at high magnification. This is due to the fact that at high magnification, the scanned area is much smaller than at low ones.

4.1.1. The static distortion model

The most commonly used distortion model represents this physical phenomenon as a decentered distortion which has both a radial and tangential component [27]:

$$\mathbf{q}^d - \mathsf{e} = \underbrace{\frac{2}{1+\sqrt{1-4\,\xi_r\,r_u^2}}(\mathbf{q}^u - \mathsf{e})}_{\text{radial}} + \underbrace{\xi_t(r_u^2 + 2(x^d - x^u)^2)}_{\text{tangential}}, \tag{25}$$

where ξ_r, ξ_t are, respectively, the radial and tangential distortion parameters. e is the center of distortion and
$\lambda = 2/1 + \sqrt{1-4\,\xi_r\,r_u^2}$ is called the factor of distortion.

4.1.2. Estimation of the center of distortion

The estimation of the center of distortion requires the use of a geometrically structured calibration pattern as the one shown in Figure 8. It consists on a planar grid of vertices $\{\mathbf{q}_i^c\}_{i\in\mathbb{N}}$. The positions of the points $\mathbf{q}_i^c$ are assumed to be known in a Euclidean coordinate frame attached to the grid. If $\mathbf{q}_i^d$ are the corresponding points in the distorted image, then each pair of points $(\mathbf{q}_i^c, \mathbf{q}_i^d)$ is linked by the epipolar relation proposed in [28] and stated as

$$\mathbf{q}_i^d \underbrace{[\mathsf{e}]_\times \mathsf{H}}_{\mathsf{F}} \mathbf{q}_i^c = 0. \tag{26}$$

$[\mathsf{e}]_\times$ is the skew-symmetric 3×3 matrix representing the cross product. H is the homography between the planar grid and the image plane. The matrix F may be called the fundamental matrix for radial distortion. It may be estimated using state-of-the-art methods [15], and the center of radial distortion can be estimated as the left epipole. In the case of no presence of radial distortion, the estimation of the fundamental matrix is unstable, and the value of

http://dx.doi.org/10.5772/61947

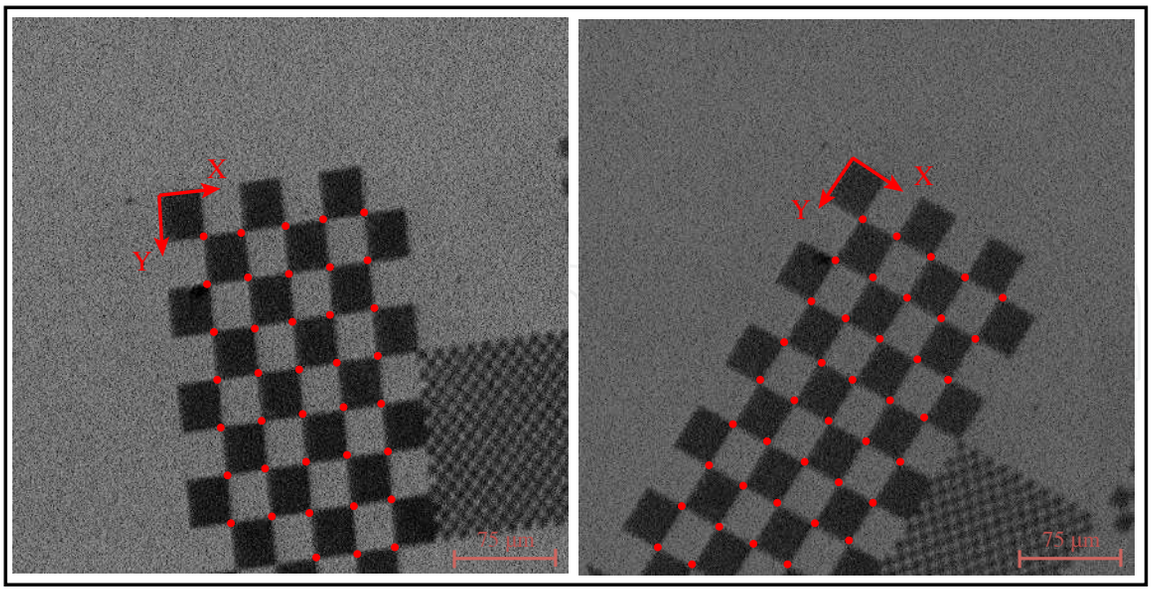

Figure 8. An example of static distortion at 400× of magnification. The image size is of 512 × 512 pixels, and the size of the squares is of 25 µm per side. The estimated center of distortion is at $\sim (290, 300)^T$ pixels.

e is meaningless. This situation can be detected during the estimation of the fundamental matrix.

The estimation of the distortion parameters ξ_r and ξ_t is processed iteratively. It is first assumed that $\xi_t = 0$ and estimate e. Then ξ_t and ξ_r are initialized to zero and estimated using bundle adjustment methods [23].

4.2. Projection model

The 3D-to-2D projection mapping can vary from perspective to orthographic. State-of-the-art works [18, 29] use either a perspective model at low magnification or an orthographic projection for high magnification with projection switch at the magnification of transition which is experimentally determined (usually 5 k×). In this chapter, a magnification-dependent projection model which smoothly switches from a perspective projection to an orthographic projection is detailed [20]. A perspective camera model can be written as

$$\mathsf{P}_0 = \mathsf{K}\mathsf{R}[\mathsf{I} \; -\mathbf{C}] = K \begin{pmatrix} \vec{r}_1^{\,T} & -\vec{r}_1^{\,T}\mathbf{C} \\ \vec{r}_2^{\,T} & -\vec{r}_2^{\,T}\mathbf{C} \\ \vec{r}_3^{\,T} & -\vec{r}_3^{\,T}\mathbf{C} \end{pmatrix}, \tag{27}$$

where $\mathbf{C} \in \mathbb{R}^3$ is the position of the projection center. $\mathsf{R} \in \mathbb{SO}(3)$ is the orientation of the projection frame. $\vec{r}_i$ is the i-th row of R, and K is the matrix of intrinsics of the form

$$\mathsf{K} = \begin{pmatrix} af & s & p_x \\ 0 & a^{-1}f & p_y \\ 0 & 0 & 1 \end{pmatrix}. \tag{28}$$

f, a, and s are, respectively, the focal length, the ratio factor, and the skew parameter. $(p_x, p_y)^T$ are the coordinates of the principal point e_0. The principal ray of the imaging system is in the direction of the vector $\vec{r_3}$, and the value $d_0 = -\vec{r_3}^T\mathbf{C}$ is the distance of the planar grid origin from the camera center in the direction of the principal ray.

Multiplying the magnification by a scale factor g acts similarly as moving the camera center backward along the principal ray. The center of the camera is then moved to $\mathbf{C} - g\vec{r_3}$. Replacing $\mathbf{C}$ by $\mathbf{C} - g\vec{r_3}$ in equation (27) gives the projection matrix at magnification g:

$$P_g = \mathsf{K}_g \begin{pmatrix} \vec{r_1}^T & -\vec{r_1}^T(\mathbf{C} - g\vec{r_3}) \\ \vec{r_2}^T & -\vec{r_2}^T(\mathbf{C} - g\vec{r_3}) \\ \vec{r_3}^T & -\vec{r_3}^T(\mathbf{C} - g\vec{r_3}) \end{pmatrix} = \mathsf{K}_g \begin{pmatrix} \vec{r_1}^T & -\vec{r_1}^T\mathbf{C} \\ \vec{r_2}^T & -\vec{r_2}^T\mathbf{C} \\ \vec{r_3}^T & d_g \end{pmatrix}, \tag{29}$$

where the terms $\vec{r_i}^T\vec{r_3}$ are zeros for $i = 1, 2$ because R is a rotation matrix. The scalar $d_g = -\vec{r_3}^T\mathbf{C} + g$ is the depth of the world origin with respect to the imaging system center in the direction of the principal ray $\vec{r_3}$. The effect of zooming by a factor g is to move an image point $\mathbf{q}^u$ on a line radiating from the principal point e_0 to the point $\mathbf{q}'^u = g\mathbf{q}^u + (1-g)e_0$. From similar triangles, we obtain that

$$g = \frac{f_g}{f_0} = \frac{d_g}{d_0} \tag{30}$$

The resulting projection matrix at a magnification g is

$$\begin{aligned} P_g &= \mathsf{K} \begin{pmatrix} g & 0 & 0 \\ 0 & g & 0 \\ 0 & 0 & 1 \end{pmatrix} \begin{pmatrix} \vec{r_1}^T & -\vec{r_1}^T\mathbf{C} \\ \vec{r_2}^T & -\vec{r_2}^T\mathbf{C} \\ \vec{r_3}^T & d_g \end{pmatrix} \\ &= g\mathsf{K} \begin{pmatrix} \vec{r_1}^T & -\vec{r_1}^T\mathbf{C} \\ \vec{r_2}^T & -\vec{r_2}^T\mathbf{C} \\ \vec{r_3}^T g^{-1} & d_0 \end{pmatrix} \end{aligned} \tag{31}$$

When $g \to \infty$, the projection mapping tends to an orthographic projection.

4.3. The static calibration method

Let us consider a calibration at the interval of magnification $[g_0, g_t]$. This range is uniformly discretized at a sampling step of δg. The different steps of the static calibration can be outlined by Algorithm 3.

To estimate $f(g)$, $a(g)$, and $s(g)$, we use second-order PDEs and we drive the same reasoning as the computation of drift PDEs in Section 3.4. Since f, a, and s are time independent, only one PDE of second-order is estimated for each parameter.

for $g = g_0$ *to* g_f *with step* G **do**
  Data: A set of N image with grid points
  calibrate the projection matrix assuming $\xi_r(g_i) = 0$ and $\xi_t(g_i) = 0$ [15];
  comptue $f(g_i)$, $s(g_i)$ and $a(g_i)$. estimate distortion center $e(g_i)$ as explained in Section 4.1.2;
  if $e(g_i)$ *is not degenerate* **then**
    initialize ξ_t and ξ_r to zero and estimate them using bundle adjustment method[23];
  else
    set $e(g_i)$ to the principal point and $\xi_r = 0$;
    initialize ξ_t to zero and estimate it using bundle adjustment method[23];
  end
end
estimate $f(g)$, $a(g)$ and $s(g)$ using PDA;

Algorithm 3: Static calibration

4.4. Static calibration of the JEOL JSM 820

This calibration is done with a multi-scale planar grid; see Figure 2 right [20]. This grid contains multiple chessboards of different sizes: 25 μm, 10 μm, 5 μm, 2 μm, and 1 μm; see Figure 9. The grid calibration points $\{\mathbf{Q}_i^c\}_{i\in\mathbb{N}}$ are selected, and three images are taken for each magnification scale g. This calibration is done for magnifications from $g_0 = 100\times$ up to $g_f = 10$ k$\times$ with a step of $500\times$. The static calibration follows the procedure explained in Section 4.3. The following results were obtained [20]:

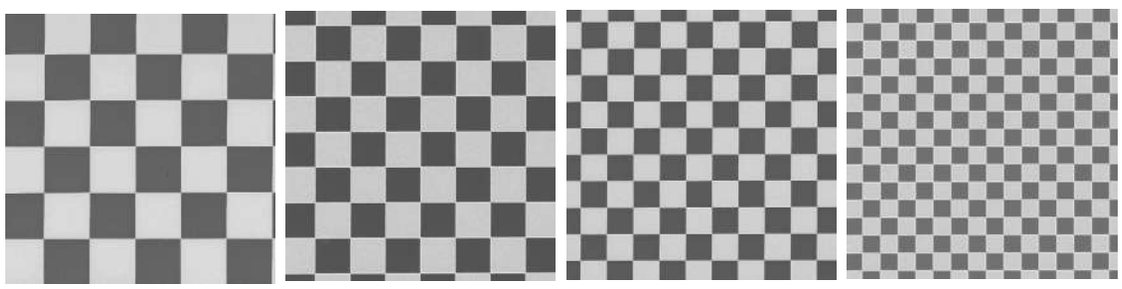

Figure 9. From left to right: Square side sizes are, respectively, of 25 μm, 10 μm, 5 μm, and 1 μm.

	PDE	$g_1 = 100\times$	$g_2 = 10$ k$\times$	solution
e_x	$\ddot{e}_x = -0.02e_x$	230.21	225.08	$e_x(g) = 230 + 10(1 - \exp(2\frac{g}{10^6}))$
e_y	$\ddot{e}_y = -0.02e_y$	270.34	265.10	$e_y(g) = 270 + 10(1 - \exp(2\frac{g}{10^6}))$

	PDE	$g_1 = 100\times$	$g_2 = 10$ k$\times$
ξ_r	$\ddot{\xi}_r = -0.0086\dot{\xi}_r + 0.015\xi_r$	0.003	0.002
ξ_t	$\ddot{\xi}_t = -0.0042\dot{\xi}_r + 0.0007\xi_r$	$-7 \cdot 10^{-7}$	$-59 \cdot 10^{-8}$

and solutions are

$$\begin{aligned} \xi_r(g) &= 0.003 - 13 \cdot 10^{-12} g - 6 \cdot 10^{-9} g^2 \\ \xi_t(g) &= -7 \cdot 10^{-7} - 13 \cdot 10^{-13} g + 6 \cdot 10^{-13} g^2 \end{aligned} \tag{32}$$

	PDE	$g_1 = 100\times$	$g_2 = 10\ \mathrm{k}\times$
focal length	$\dot{f} - 0.35 \cdot 10^{-4} = 0$	$0.35 \cdot 10^4$	
aspect ratio	$10^{13}\ddot{a} = -0.2225\,\dot{a} + 0.0017\,a$	1	1.1
skew	$10^{13}\ddot{s} = -0.2059\,\dot{s} + 0.0016\,s$	10^{-3}	$1.9 \cdot 10^{-3}$

and solutions are

$$\begin{aligned} f(g) &= 0.35 \cdot 10^{-4}\, g \\ a(g) &= 0.05(g \cdot 10^{-4}) + 0.95(g \cdot 10^{-4})^2 \\ s(g) &= \frac{-0.05 + 0.65(g \cdot 10^{-4}) + 0.40(g \cdot 10^{-4})^2}{10^3} \end{aligned} \tag{33}$$

The calibration results show variations of 10 pixels at most around a median principal point of $(245, 260)^T$ pixel. Finally, Figure 10 shows the RMS reprojection error between image points and back-projected planar grid points. It corresponds to a median value of 7 pixels without any correction and to 3 pixels after drift compensation, and without distortion correction, it decreases down to 1.45 pixel with both drift and distortion correction.

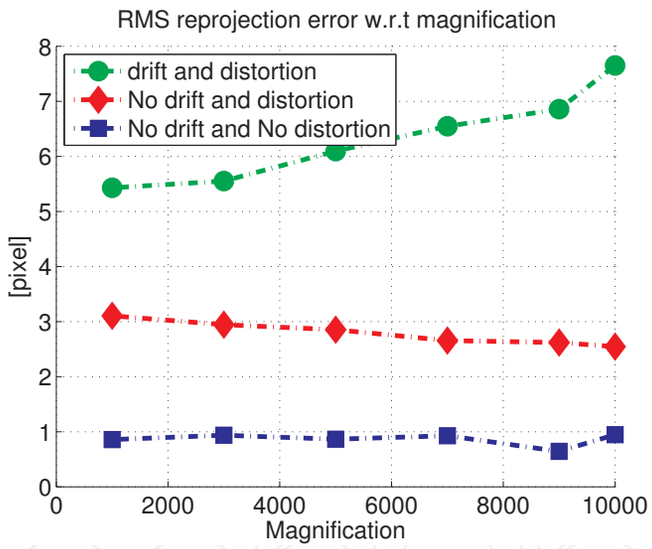

Figure 10. The RMS reprojection error through magnification scales. The average RMS error is about 0.9 pixel.

5. A small toy application: Cantilever deformation measurement

As a simple application to conclude this chapter, we propose to quantify the deformations of a cantilever that we deform with a micromanipulator. The cantilever is 35 µm long, 3.5 µm wide, and 300 nm thick. The micromanipulator is the *Kleindiek MM3A-EM* with a rigid tool mounted on the tip. The cantilever is fixed within a holder and is deformed by the moving of the tool tip; see Figure 11. Such an experiment may have several applications in the mechanical characterization of cantilevers [30], of biological deformable objects [31], etc. To check the accuracy of the calibration process, a simple test can be made. We estimate the repeatability of the measures for three different magnifications: 190×, 230×,

http://dx.doi.org/10.5772/61947

and 260× [20]. The deformation measures which evaluate our calibration method use the magnification-smooth calibration parameters described in the previous section. It is worth to notice that these parameters were not estimated directly at these three magnification scales, but the estimated magnification-smooth functions allow us to find the calibration parameters at any magnification factor in the range $[100\times, 10\,\mathrm{k}\times]$. A set of 11 configurations are taken for each magnification factor (11×3 images). Initially the cantilever is straight and free from any contact with the planar surface. Then, it comes close to the tip of the cantilever which is progressively pushed forward by the *MM3A-EM*. After 7×3 acquired images at different configurations of the deformation, the cantilever is progressively dragged backward to the initial contact-free configuration; see Figure 12. Through the whole experiment, a time tracking frame acquisition is automatically processed using the PC processor's clock trigger. This time acquisition is important to retrieve the amount of pixel by which the acquired images have drifted. The acquired images are undrifted and undistorted with the estimated calibration parameters. We assume that during the deformation, the cantilever sweeps a virtual plane. The affine homography between image pixels and this deformation plane is estimated [16] by taking into account the estimated parameters of the projection model. The Euclidean stratification is done using the length of the cantilever provided by the manufacturer. The stratified homography gives us the mapping between distances in the image and their corresponding metric values in the deformation plane. The amount of deformation is measured as the distance between the tip of the cantilever at rest and its position after deformation. The measured deformation reaches a maximum of 250 nm. After drift and distortion correction, the standard deviation of the error among the three scales is of about 10 nm which is an acceptable amount of error at this scale of magnification.

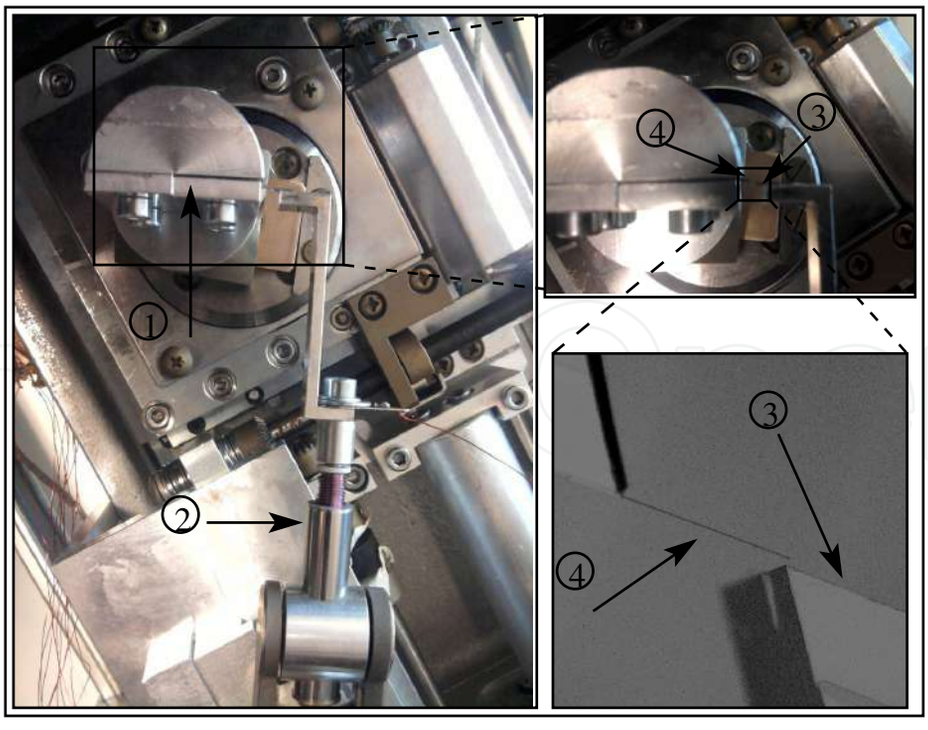

Figure 11. The setup of the example: 1. Holder of the cantilever; 2. *Kleindiek MM3A-EM*; 3. deforming tool; and 4. cantilever.

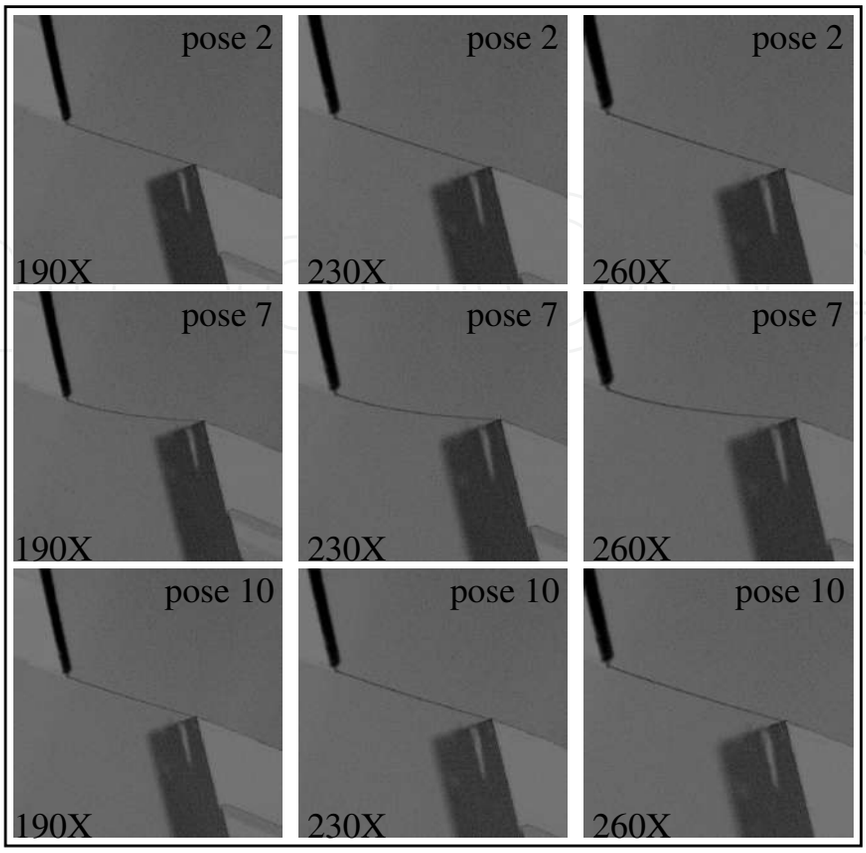

Figure 12. Three configurations of deformation (pose: 2, 7 and 10) at the three different magnification factors. The maximum of the deformation is at pose 7. Poses: 1 and 11 are contact-free between the cantilever and the plan.

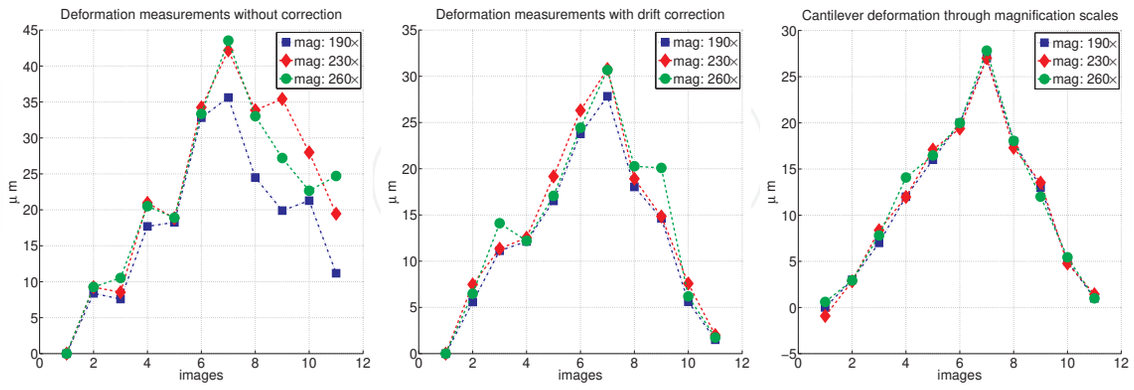

Figure 13. Left figure: Measured deformation without neither drift compensation nor static distortion correction. Middle figure: Measured deformation after drift compensation but without static distortion correction. Right figure: Deformation measures for the three magnification scales with drift and static distortion correction. The repeatability 10 nm. It can be seen that the drift and distortion correction improve considerably the repeatability of the measurements for the three scales.

6. Conclusion

In this chapter, a spatiotemporal calibration model for SEM imaging systems was presented. This model has the advantage of being smooth with respect to magnification scales. Both dynamic (temporal) and static (spatial) mappings are treated. The evolution over time and magnification of the pixel drifts and of the spatial distortion and projection matrices are modeled by mean of PDA.

Author details

Abed Malti*

*Address all correspondence to: abed.malti@gmail.com

INRIA, France

References

[1] F. Vignon, G. Le Besnerais, D. Boivin, J.L. Pouchou, and L. Quan. 3D reconstruction from scanning electron microscopy using stereovision and self-calibration. In *Physics in Signal and Image Processing*, Marseille, pages 23–24, 2001.

[2] M. Jaehnisch and S. Fatikow. 3-d vision feedback for nanohandling monitoring in a scanning electron microscope. *International Journal of Optomechatronics*, 1:4–26, 2007.

[3] S. Fatikow, C. Dahmen, T. Wortmann, and R. Tunnel. Visual feedback methods for nanohandling automation. *International Journal of Information Acquisition*, 6(3):159–169, 2009.

[4] M.A. Sutton, N. Li, D. Garcia, N. Cornille, J.J. Orteu, S.R. McNeill, H.W. Schreier, X. Li, and A.P. Reynolds. Scanning electron microscopy for quantitative small and large deformation measurements part II: Experimental validation for magnifications from 200 to 10,000. *Experimental Mechanics*, 47:789–804, 2007.

[5] T. Sievers and S. Fatikow. Real-time object tracking for the robot-based nanohandling in a scanning electron microscope. *Journal of Micromechatronics*, 3(3–4):267–284, 2006.

[6] B.E. Kratochvil, L. Dong, and B.J. Nelson. Real-time rigid-body visual tracking in a scanning electron microscope. *International Journal of Robotics Research*, 28:498–511, 2009.

[7] T. Kasaya, H.-T. Miyazaki, S. Saito, K. Koyano, T. Yamaura, and T. Sato. Image-based autonomous micromanipulation system for arrangement of spheres in a scanning electron microscope. *Review of scientific instruments*, 75(6):2033–2042, 2004.

[8] T. Sievers and S. Fatikow. Visual servoing of a mobile microrobot inside a scanning electron microscope. In *2005 IEEE/RSJ International Conference on Intelligent Robots and Systems*, Edmonton, 2005.

[9] M.A. Sutton, N. Li, D. Garcia, N. Cornille, J.J. Orteu, S.R. McNeill, H.W. Schreier, and X.D. Li. Metrology in a scanning electron microscope: Theoretical developments and experimental validation. *Measurement Science and Technology*, 17:2613–2622, 2006.

[10] M.A. Sutton, N. Li, D. Garcia, N. Cornille, J.J. Orteu, S.R. McNeill, H.W. Schreier, X. Li, and A.P. Reynolds. Scanning electron microscopy for quantitative small and large deformation measurements part I: Sem imaging at magnification from 200 to 10,000. *Experimental Mechanics*, 47:755–788, 2007.

[11] N. Li, M.A. Sutton, X. Li, and H.W. Schreier. Full-field thermal deformation measurements in a scanning electron microscope by 2d digital image correlation. *Experimental Mechanics*, 48(5):635–646, 2008.

[12] T. Zhu, M.A. Sutton, N. Li, J.-J. Orteu, N. Cornille, X. Li, and A.P. Reynolds. Quantitative stereovision in a scanning electron microscope. *Experimental Mechanics*, 51(1):97–109, 2011.

[13] P. Cizmar, A.E. Vladar, and M.T. Postek. *Real-Time Image Composition with Correction of Drift Distortion*. Technical Report, arXiv:0910.0213, Oct 2009.

[14] B. Mokaberi and A.A.G. Requicha. Towards automatic nanomanipulation: Drift compensation in scanning probe microscopes. In *Proceedings of the 2004 IEEE International Conference on Robotics and Automation (ICRA 2004)*, New Orleans, pages 416–421, 2004.

[15] R.I. Hartley and A. Zisserman. *Multiple View Geometry in Computer Vision*, 2nd ed. Cambridge: Cambridge University Press, 2004.

[16] Y. Ma, S. Soatto, J. Kosecka, and S.S. Sastry. *An Invitation to 3-D Vision: From Images to Geometric Models*. New York: Springer, 2003.

[17] O. Sinram, M. Ritter, S. Kleindiek, A. Schertel, H. Hohenberg, and J. Albertz. Calibration of an sem, using a nano positioning tilting table and a microscopic calibration pyramid. In *ISPRS Commission V Symposium*, Corfu, pages 210–215, 2002.

[18] N. Cornille. *Accurate 3D Shape and Displacement Measurement using a Scanning Electron Microscope*. PhD thesis, University of South Carolina and Institut National des Sciences Appliquées, 2005.

[19] A. Malti, S. Dembélé, N. Piat, C. Arnoult, and N. Marturi. Toward fast calibration of global drift in scanning electron microscopes with respect to time and magnification. *International Journal of Optomechatronics*, 6(1):1–16, 2012.

[20] A. Malti, S. Dembélé, N.L. Fort-Piat, P. Rougeot, and R. Salut. Magnification-continuous static calibration model of a scanning-electron microscope. *Journal of Electronic Imaging*, 21:1–16, 2012.

[21] J.O. Ramsay. Principal differential analysis: Data reduction by differential operators. *Journal of the Royal Statistical Society, Series B*, 58:495–508, 1996.

[22] A.W. Fitzgibbon. Simultaneous linear estimation of multiple view geometry and lens distortion. In *2001 IEEE Computer Society Conference on Computer Vision and Pattern Recognition (CVPR 2001)*, Kauai, pages 125–132, 2001.

[23] I. Lourakis and A. Argyros. Sba: A software package for generic sparse bundle adjustment. *ACM Transactions on Mathematical Software*, 36:2:1–2:30, 2009.

[24] J.O. Ramsay and B.W. Silverman. *Functional data analysis*, 2nd ed. New York: Springer, 2005.

[25] G.B. Folland. *Fourier Analysis and Its Applications*. The Wadsworth and Brooks/Cole Mathematics Series. Pacific Grove: Wadsworth & Brooks/Cole Advanced Books & Software, 1992.

[26] M. Frigo and S.G. Johnson. The design and implementation of FFTW3. *Proceedings of the IEEE*, 93(2):216–231, 2005. Special issue on "Program Generation, Optimization, and Platform Adaptation".

[27] J. Heikkila and O. Silven. A four-step camera calibration procedure with implicit image correction. In *Proceedings of the 1997 Conference on Computer Vision and Pattern Recognition (CVPR '97)*, Washington, DC, page 1106. IEEE Computer Society, 1997.

[28] R.I. Hartley and S.B. Kang. Parameter-free radial distortion correction with center of distortion estimation. *Pattern Analysis and Machine Intelligence*, 29(8):1309–1321, Aug 2007.

[29] M. Ritter, M. Hemmleb, P. Faber, B. Lich, and H. Hohenberg. Sem/fib stage calibration with photogrammetric methods. In *ISPRS Image Engineering and Vision Metrology*, Dresden, 2006.

[30] G. Ionascu, E. Manea, C. D. Comeaga, N. Alexandrescu, I. Cernica, and L. Bogatu. Silicon cantilever beam micromachining and structure geometry characterization. In *International Conference on Semiconductor*, Kobe, 2009.

[31] M. Boukallel, M. Gauthier, M. Dauge, E. Piat, and J. Abadie. Smart microrobots for mechanical cell characterization and cell convoying. *IEEE Transactions on Biomedical Engineering*, 54(8):1536–1540, 2007.

IntechOpen

Chapter 3

Scanning Electron Microscopy with a Retarded Primary Beam

Luděk Frank

Additional information is available at the end of the chapter

http://dx.doi.org/10.5772/62054

Abstract

The general trend for reducing the energies of primary electrons in electron microscopy has been faced with a gradual deterioration of the image resolution. Biasing the sample to a high negative voltage and making the electrons arbitrarily slow solely on and inside the sample has shown itself to be far more feasible than originally expected. The fundamental aberration coefficients (spherical and chromatic) of a combination of an objective lens and an immersion electrostatic lens formed by the biased sample decrease with the decreasing landing energy of the electrons. As a result, the spot size in scanning systems may become nearly independent of the landing energy of the electrons. The requirements placed on samples are strict but feasible, and detection of signal electrons is greatly facilitated by the acceleration of both reflected and transmitted electrons in the field of the biased sample and their collimation toward the optical axis. The interaction of slow electrons is not only more intensive than that at standard energies but even scattering phenomena appear which are not otherwise observed. Several application examples are presented. The benefits of very low energy EM are still being uncovered after its having been in routine use for several years.

Keywords: Scanning electron microscopy, scanning transmission electron microscopy, slow electrons, electron microscopy of materials, biomedical electron microscopy

1. Introduction

Historically, progress in electron microscopy and its applications in virtually all branches of science and technology, including health care, was "instrument driven" in the initial decades until around the end of the previous millennium. During this time, efforts in developing instrumentation and methodology were concentrated primarily on improving the image resolution up to its physical limitations. If we restrict ourselves to scanning microscopy

techniques, the goal was to minimize the dimensions of the spot of the primary beam incident on a sample. A second aim was to seek possibilities of combining the basic electron optical imaging tool with various analytical attachments. Tailoring the ultimate solution of the instrument to a specific microstructure- or nanostructure-bound task was not unfamiliar but certainly did not predominate. Progressively enhanced tools for the computer-aided simulation of the properties of electron optical elements and systems up to the complete simulation of the imaging process enabled the community of instrumentation scientists to turn to the design of a device according to the quantities and processes that are to be monitored and measured. A concentration on the deeper understanding of the collection of the image signal via identification of those parts of the energy and angular distributions of the emitted species that are acquired by detectors goes hand-in-hand with this. To put it more simply, understanding and interpretation of the image begins to overshadow the problems of generating and shaping the exciting primary electron beam. This kind of activity is surely facilitated if the energy of the electrons incident on the sample can be freely chosen in such a way that this degree of freedom can be fully utilized.

The range of energies of the primary electron beam available for the formation of sufficiently sharp beams in the scanning electron microscope (SEM) was for a long time limited by the practical obstacles that emerge when lowering the beam energy. These include the decreasing efficiency of extraction of electrons from the gun cathode, the increasing undesired manifestation of external spurious influences in proportion to the time of flight of the beam, and, most importantly, the enlargement of the size of the disks of confusion due to chromatic and diffraction aberrations making the primary spot dimension steeply extending toward low energies. However, since the very beginning of the electron microscopy era, the possibility of having an electron energy very low at the sample and sufficiently high in the column was known from devices using immersion objective lenses [1,2]. These traditionally appear in emission electron microscopes, where the sample itself is the source of electrons, mostly excited by incident photons, which are usually emitted at units or tens of electronvolts and strongly accelerated immediately above the sample surface biased to a high negative potential. Moreover, the idea of reverting the ray path and using the sample bias to retard the impinging primary beam generated and formed at a high energy in a standard electron gun and column is similarly old [3]. This idea appeared in the literature several times in the following years, though without serious attempts at implementation, with the exception of a study presenting the very first experimental results but nevertheless not at a convincing quality [4]. Surprisingly, the first successful implementation of the idea of retarding the electron beam just on the sample was not conditioned by preliminary simulation studies or the assembly of a dedicated device; enough courage to take on a task generally considered to have little prospects was sufficient [5,6]. The crucial objection met at the very beginning was the anticipated existence of various lateral fields close to the sample surface that would destroy the image by smearing both the primary and signal fluxes when they are so slow. Practical experience proved much less critical, and the first series of micrographs of a quality consistent through the full energy range down to 1 eV was published in 1993 [7].

http://dx.doi.org/10.5772/62054

The first decade of collecting experience with this innovative SEM mode was summarized in a review [8], and shorter reviews were then published at intervals of a few years [9,10]. More specific reviews concerning materials science and nanotechnology applications have appeared recently [11,12]. Here, we are to extend the series of reviews presenting in brief the instrumental and methodological fundamentals and listing the recent successful application examples.

2. Motivation

When operating the scanning electron microscope (SEM) between, say, 5 and 10 keV, we enjoy an optimum compromise between conditions governing the primary beam formation and those characterizing the beam-sample interaction. We are able to extract sufficient electron current from all main types of sources and transport the beam over a column of tens of centimeters in length at a constant energy with a reasonable impact of spurious influences. Similarly, the corresponding wavelength of electrons and the energy spread of the beam in tenths of electronvolts, together with main aberration coefficients in millimeters, enable us to get a spot size of 1 nm or even slightly less. At the same time, the interaction volume of electrons of this speed in solids varies between units and hundreds of nanometers in size according to the sample material, although the true image resolution might be nearer to the spot size, provided sufficiently sharp structure details are present on the sample surface. Total yields of secondary and backscattered electrons are more or less comparable and can be easily separated as image signals. Conventional detectors acquire a part of the secondary electron (SE) emission attracted to a side-attached assembly with a front bias or a hollow cone of straight trajectories of backscattered electrons (BSE) with a ring-shaped diode or scintillator. The relief contrast of SE and material and channeling contrasts of BSE dominate routine SEM practice.

The observation of thin samples in a scanning transmission electron microscope (STEM) is traditionally performed at around 200 keV in dedicated instruments and around 30 keV in SEM devices equipped with a STEM attachment. While tissue sections for the former microscopes are prepared at hundreds of nanometers in thickness and samples containing heavier elements are correspondingly thinner, at tens of kiloelectronvolts, we have to go down to 100 nm and below. Detectors of transmitted electrons are split into several concentric rings so that the signal species can be sorted according to the scattering angle from the optical axis. This helps in obtaining sufficient contrasts from samples providing larger differences in local thickness or in atomic numbers of constituting elements. Of utmost importance here are the challenges of sample preparation, mainly as regards the aims of highlighting certain structure details considered interesting. Thanks to the concentrated illumination of primary electrons, samples for STEM can be somewhat thicker than those for TEM, but otherwise the experimentation issues are similar.

The traditional arrangement characterized above suffers from several drawbacks. Fast primary electrons interact mainly with atom cores, elastic forward scattering dominates, and inelastic scattering is weak. Scattering phenomena can be mostly explained within the laws of classical physics and the emitted signals do not respond to the quantum mechanical interior of the

samples. The interaction volume of the beam in solid targets is too large, for which reason embedded structures such as precipitates are imaged fuzzy and both thin surface films and a great many relief details are invisible. The majority of signal species generated in depth do not penetrate to the surface to be emitted. Nonconductive materials charge up negatively to a surface potential in the kilovolt range. The edge effect, i.e. overbrightening of steeply inclined surface facets, impedes the measurement of distances and dimensions in SEM images. Fast BSE move along straight trajectories and the majority of them escape detection and impinge on the chamber walls. The main problems of STEM at standard energies include low contrasts, particularly with samples of living matter that need to be prepared with salts of heavy metals that highlight some but not all structure details, and the averaging of structure details across the sample thickness, which may hide some of them completely.

When decreasing the primary beam energy well below 5 keV or even to hundreds, tens, or units of electronvolts, we enter a different world of imaging conditions. Scattering events are increasingly dependent on the complete 3D potential distribution inside the target, i.e. they sense truncation of atomic potential by electrons and electron-electron interactions in general. Inelastic scattering and elastic backscattering become more important, so the crystallinity contribution to image contrast is enhanced. Below about 30 to 40 eV, electrons entering the target start behaving as Bloch waves, so their penetration inside is conditioned by the presence of unoccupied electron states in the particular direction and slow electron reflectivity can serve as a measure for the density of states and, therefore, can serve to fingerprint the orientation of grains in polycrystals, for example [13–15]. Interaction volume diminishes and information carried by emitted electrons is better localized laterally, while the surface sensitivity also increases, enabling one to observe all surface details and coverage. The edge effect disappears when the penetration depth stops exceeding the escape depth of signal species. Surface charging is reduced with increasing yield of SE, and at the "critical energy", at which the fluxes of incident and outgoing electrons are identical, no charge is dissipated and noncharging microscopy is possible under any vacuum conditions. The total yield of signal electrons reaches its maximum somewhere in the range of hundreds of electronvolts, exceeding the unit level with minor exceptions. In this range, nonconductive samples charge positively, although charge balance is again achieved at the even lower first critical energy. The positive charging is moderate only, thanks to the partial retraction of the slowest emitted electrons by the field of the surface potential. The wavelength of electrons extends, and when it becomes similar to interatomic distances at units of electronvolts, interference of waves reflected on both sides of surface atomic steps (divided wavefront interference) or on both surfaces of ultrathin surface coatings (divided amplitude interference) becomes a new contrast mechanism. As in LEED, backscattering in the range of tens of electronvolts concentrates BSE to diffracted spots that may reveal the surface crystallinity when selectively detected. Moreover, electrons leaving the sample close above the surface barrier are partially reflected, so the height and shape of the barrier contribute to the imaging signal.

When reducing the primary beam energy in a STEM, we obtain, first and foremost, higher contrast. The differential cross-sections governing both the elastic and the inelastic scattering mechanisms are inversely proportional to the energy of electrons, mostly to energy squared.

For this reason, the spatial density of the generation of the image information steeply increases so that, below 1 keV, we can get, for example, on tissue sections containing no agents with heavy metal salts not only very high contrast but also all structure details visualized, including those normally not highlighted with postfixation or staining media [16]. Naturally, the sections have to be thinner. For the range of hundreds of electronvolts, thicknesses below 10 nm are desirable. The production of such sections is, however, already feasible [17]. Moreover, thanks to reduced in-depth averaging of image layers, we get the chance of revealing tiny details unknown to date. With true 2D crystals of a single atom thickness, such as graphene, we can get nonnegligible electron penetration down to 1 eV [18] and obtain data that is extremely valuable for applications in nanoelectronics, for example.

The reasons for reducing the energy of electron incidence on targets in the scanning devices down to the lowest values, including the principle of implementation described below, have existed in the historical literature from the very beginning of the electron microscopy era and have been permanently demonstrated and supported more recently with indisputable results from the beginning of the 1990s. Starting from the 12th EUREM in Brno in 2000, the method was discussed at all large microscopy conferences and congresses in dedicated sessions. Still, the first commercially available SEMs allowing operation at tens of electronvolts did not appear until 2006/2007, and even then, the volume of application results in the literature remained extremely limited. Only quite recently, in the last 3 or 4 years, the "cathode lens" method has become a widely used standard tool in SEM practice. This circumstance starts erasing reasons for compiling review texts addressing just the method and transfers the observation material to reviews devoted to families of specimens. Nevertheless, the aim of this chapter is to summarize the fundamentals of the method, although it also features a list of successful applications in which very low energy SEM provides an important added value.

3. Implementation

The problem of having very slow electrons on the sample surface and fast electrons in the column outside the sample was solved as early as 1932 with the immersion objective lens [1]. The first considerations counted on the sample as the source of electrons, but since 1942 a design has existed for an electron microscope delivering fast electrons toward the sample biased to a high negative potential in order to retard the electrons immediately before their impact on the sample surface [3]. The leading idea at that time was to reach energies of impact that produce the maximum yield of secondary electrons. For these reasons, there was really nothing new in the attempts to revitalize the principle that appeared sporadically over the following 50 years, though without convincing experimental results. With hindsight, we can now say that past attempts were probably not initiated with sufficient seriousness because of doubts connected with the necessity of heavy biasing of the specimen, which indicated conditions that were later shown to be not so strict, such as the necessity of having the sample surface very finely polished, similarly to the electrodes of electrostatic lenses.

The principle of implementation of very low energy SEM and STEM is simply as follows: the sample is biased to a high negative potential similar to the negative potential of the cathode

in the electron gun of the microscope. The energy of electron impact on the sample is then given by the difference between the two potentials. An adverse factor here is the fact that, while the potential values are subtracted, their fluctuations are added, which amplifies the noise at the lowest impact energies quite substantially. It is much better to implement a "low voltage booster", i.e. a positively biased axial tube insulated from the surrounding column that accelerates electrons just behind the gun anode and returns them to their original energy at the end of the objective lens [19,20]. The impact energy is then simply provided by another supply connected between the gun cathode and the sample. If we close the booster field at the end of the objective lens, we get a compound lens consisting of a (usually magnetic) focusing lens and an electrostatic retarding lens, an assembly long known [21] and incorporated into many commercially available electron microscopes under the name the Gemini lens.

The core concern is to know the electron optical parameters of the combination of the objective lens of the SEM with the electrostatic field above the sample. This field is, in fact, generated in a two-electrode immersion electrostatic lens with the sample serving as the cathode; this assembly is often called the "cathode lens" (CL). The anode of this lens has to have a central bore of some kind passing the primary beam so its field can be seen to be composed of a homogeneous retarding field and a field penetrating through the anode bore. On a three-electrode arrangement (cathode/grid/anode), Recknagel [2] derived an image formation theory employing expansion in ε/U, where ε is the electron energy in the surface plane of the sample and U is the acceleration voltage inside the lens. The analysis by Lenc and Müllerová [22,23], considering the anode field approximated with a second-order polynomial within a thin transition region in the anode plane, is more transparent. The main quantities, i.e. the spherical C_S and chromatic C_C aberration coefficients, were written (for large ratios E_P/E) as [23]

$$C_S \cong \frac{l}{E_P}E + \left(\frac{l^2}{D} + \frac{81}{16}{C_S}^f\right)\frac{1}{{E_P}^{3/2}}E^{3/2} + \ldots, \quad C_C \cong -\frac{l}{E_P}E + \frac{9}{4}\frac{{C_C}^f}{{E_P}^{3/2}}E^{3/2} + \ldots \tag{1}$$

where E is the landing energy of electrons, E_P is the primary energy before retardation in the cathode lens, l is the length of the cathode lens field, D is the diameter of the anode bore, and C_S^f and C_C^f are the relevant aberration coefficients of the focusing objective lens. Obviously, the lower the landing energy of the electrons, the smaller the aberration coefficients, which is a relationship opposite to that valid for standard configurations without immersion, i.e. with energy independent aberrations. When decreasing the landing energy down to units of electronvolts, the aberration coefficients tend to fall in the micrometer range, which compensates very efficiently for other influences adverse from the point of view of image resolution. In Figure 1, we see typical energy dependences of the spot size for the sample bias switched on and off, in both cases with the beam aperture tailored separately to each landing energy, together with a particular case of the beam aperture before retardation fixed to a value optimum for a certain landing energy. At very low energies, the spot size deteriorates proportionally to $E^{-3/4}$ in the standard SEM, while the cathode lens reduces this slope to $E^{-1/4}$. For larger aberrations of the focusing lens, we can even get an energy-independent spot size [8].

http://dx.doi.org/10.5772/62054

We should mention here that, in the case of the Gemini compound lens, the working distance of the immersion electrostatic lens is nonzero (in contrast to the CL), so the basic aberration coefficients do not keep decreasing proportionally to the landing energy E without limitations, but the relevant equations contain an "absolute" member proportional to the working distance [24] so the spot size remains acceptable only down to a certain energy threshold. A comparison of the Gemini and cathode lenses is discussed in great detail in Ref. [25].

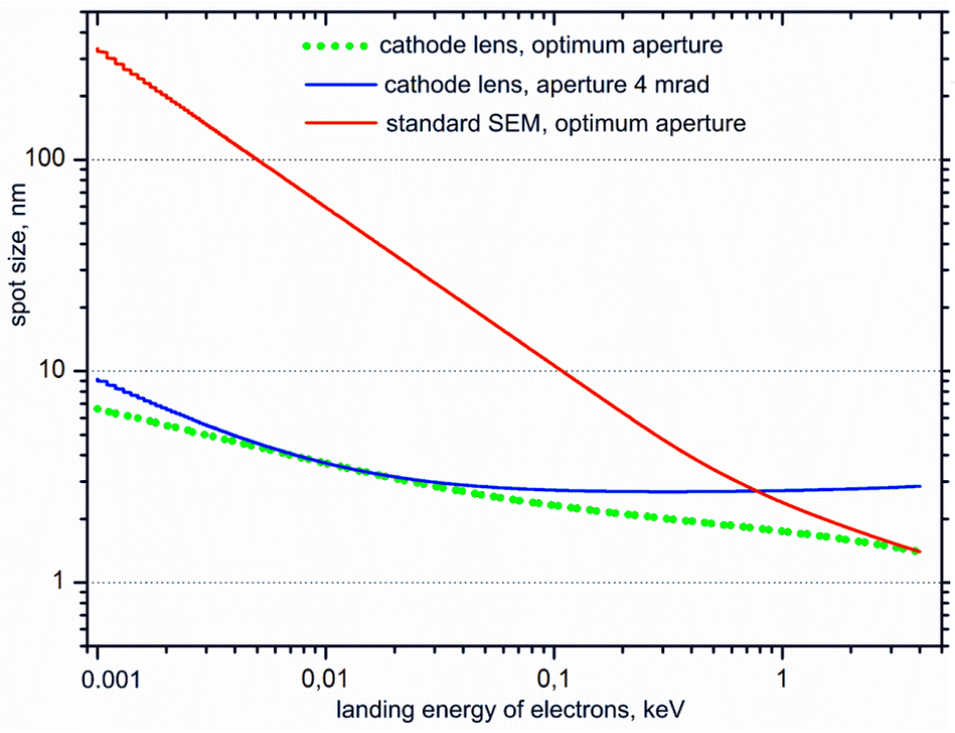

Figure 1. Energy dependences of the spot size for a typical magnetic focusing lens combined with a cathode lens.

The advantages of an assembly containing a cathode lens include the landing energy of electrons easily adjustable by the sample bias with the alignment of the microscope column untouched. Nevertheless, by altering the bias, we also vary the optical parameters of the electrostatic lens, first and foremost, the object distance of the sharp spot size and the dimensions of the field of view currently adjusted with scanning coils or electrodes. Approximate analytical calculations have shown these variations to be only moderate: at very low landing energies, the final magnification ranges between 1/2 and 2/3 of that with the CL off, in dependence on the position of the pivot point of the scanning system [7]. As regards the underfocusing necessary to compensate the cathode lens action, this amounts to units of micrometers per electronvolt at very low energies [7]. Algorithms suitable for correction of magnification and focusing in dependence on the cathode lens excitation can be found in Ref. [26]. Variations in the beam aperture and the beam impact angle with the landing energy are more important. In well-adjusted CL, we decrease only the axial component of the velocity of electrons, so the beam aperture enlarges, roughly in proportion to $(E_P/E)^{1/2}$. Similarly, amplification always occurs to the angle of impact of the primary beam on the sample surface when

the rocking style of scanning is employed with a pivot point above the sample. Although the impact angle normally grows toward the margin of the field of view quite negligibly, after this "amplification", it has to be considered, particularly when imaging crystalline samples exhibiting channeling contrast. At very low energies, we also have the field of view restricted by the total reflection of electrons taking place at a distance from the optical axis at which the glancing impact of electrons is achieved.

The cathode lens is aligned when the above-sample field is homogeneous and the nondeflected primary beam impacts normally on the sample. If any sample tilt is required, we have to count on some smearing of the primary spot due to the lateral field generated by the tilt. Moreover, the inclination of the beam by the mechanical tilt angle is again multiplied by the ratio of axial velocities before and after retardation. In this case, multiplication of the impact angle might prove advantageous. Practical experience has shown that all these apparent drawbacks of an assembly containing a cathode lens are manageable in practice without placing a great burden on the operator.

The alignment of the cathode lens consists of placing the anode bore on the optical axis and adjusting the sample by means of slight tilts to a parallel position with respect to the anode. Both these conditions are easily controllable with an anode made from a scintillator plate, preferably single crystal, sensitive on both sides. We then "see" the upper surface of the anode/detector and, at low magnification, can align its bore laterally to the screen center. At very low energies, we begin observing the above-sample assembly by means of electrons backscattered from the sample surface near the total reflection. Electrons emitted from individual sites on the sample are collimated in the strong field into narrow bundles so those emitted around the center of the field of view mostly escape through the anode bore. For this reason, we see the same anode bore dark from the bottom, and when both these circles are made concentric, the CL field is homogeneous. Reliable adjustment requires a sample stage equipped with two independent, mutually perpendicular sample tilts. A combination of sample tilt and rotation may also be helpful. The alignment is illustrated in Figure 2. The same approach may also be successful for other versions of the anode if the anode bore can be made visible around the view-field center.

The adverse external influences typical of the SEM include stray fields, primarily an external magnetic field. The deflection of the primary beam due to such a field depends on the time of flight of the beam, which decreases when reducing the range of flying at low energy. This is minimized in the case of zero working distance of the immersion lens, i.e. the cathode lens. When comparing the deflection at 20 keV and 200 eV, we get a ratio of 1:10 without the cathode lens but just 1:1.5 if the landing energy of 200 eV is obtained by retardation from 20 keV in the CL [25].

A strong electric field around the sample affects the primary electrons, although it affects the signal species even more because of their widely varying energy and directions of motion. Now, let us consider the negatively biased sample inserted between two grounded detectors, of which the upper one is either the CL anode or any detector above the anode to which electrons are passing through the anode bore and the lower detector is of an arrangement typical for the scanning transmission electron microscope (STEM) instrument. The homoge-

http://dx.doi.org/10.5772/62054

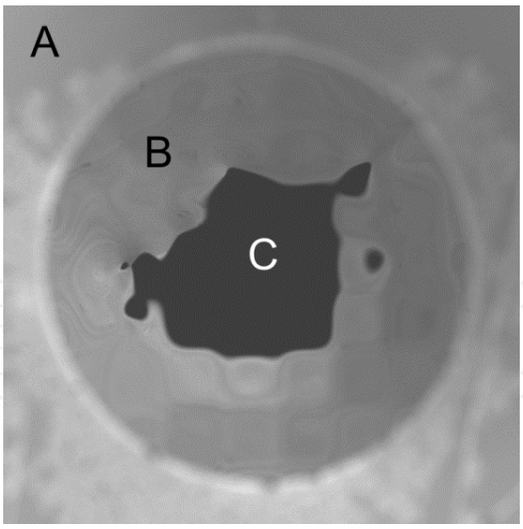

Figure 2. Illustration of a well-aligned cathode lens: the bored scintillator disc of the BSE detector also serving as the anode (A), sample surface biased to a mirroring voltage (exceeding the acceleration voltage in the gun) (B), and mirror image of detector bore (the irregular contour is due to the unevenness of the sample consisting of a foil deposited on a mesh) (C).

neous field of the CL accelerates the backscattered or transmitted electrons off the sample surface and collimates them into a bundle of a width decreasing with increasing field strength. The complete angular distribution for the full polar angle range (0, $\pi/2$) is concentrated in a circle of diameter [8].

$$d = \frac{4l}{\sqrt{k_e - 1}} \tag{2}$$

where k_e is the ratio of the final and initial energies of the emitted electrons. Generally, electrons are emitted at energies ranging between zero and the landing energy E, and although this interval may be quite short in comparison to the final energy, the factor k_e may vary widely. We then get the signal electrons in the anode plane sorted according to their emission energy, which enables a certain energy filtering. In particular, secondary electrons (SE), if released at a low landing energy, are usually collimated to within a diameter of tenths of millimeters so they mostly escape through the anode bore, and if the anode also serves as the detector, we get an image signal composed almost exclusively of backscattered electrons (BSE). It is important that the complete BSE emission is usually collimated to a diameter in units of millimeters so we also acquire BSE emitted at large angles with respect to the surface normal that are usually omitted in conventional SEMs. As we will see later, SE also contribute to the transmitted electron (TE) signal acquired with a below-sample situated detector because they are accelerated similarly as TE passing the sample with various energy losses. Having the TE detector composed of traditional concentric sensitive detector rings for acquisition of bright-field (BF), dark-field (DF) and high-angle annular dark-field (HAADF) signal components, we should get SE in the BF channel only.

In modern SEMs, the sample is often immersed in a strong magnetic field of an open objective lens in order to improve the electron optical parameters of the column. When combining the open magnetic focusing lens with the CL, we face the question of the trajectories of signal electrons, particularly as regards the interpretation of their initial angular distribution on the basis of currents obtained in detector channels. As Figure 3 shows, the mismatch in the angular distribution normally appearing with the sample in a magnetic field is nearly fully eliminated by means of the electric field for $k_e = 11$.

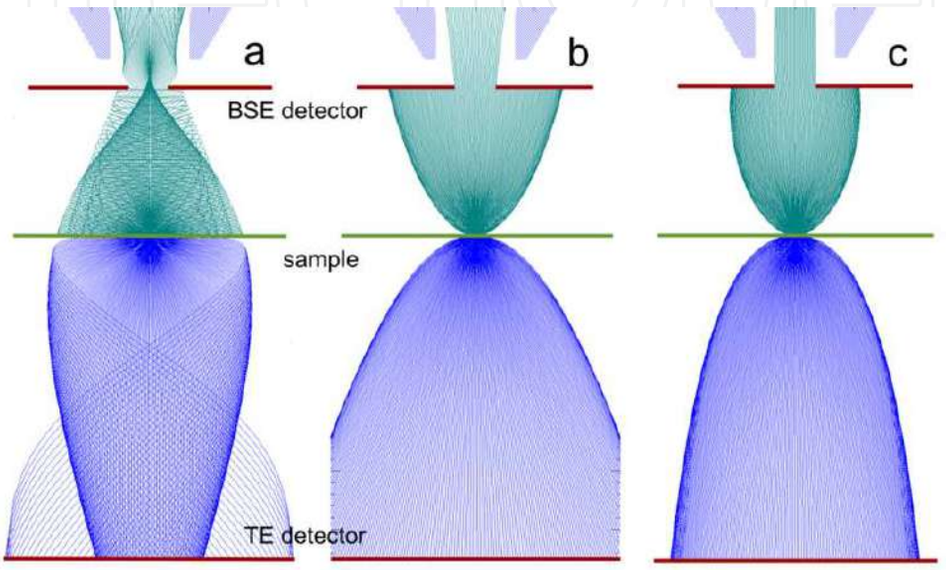

Figure 3. Trajectories of elastically backscattered and transmitted electrons from a sample immersed in the magnetic field of an open magnetic lens (a), from a sample to which the primary electrons are retarded 11 times (b), and from a sample surrounded by both fields (c).

As regards the detectors themselves, they are impacted by electrons accelerated approximately to the energy of electrons acquired in the microscope gun. The standard BSE detectors of SEMs, whether scintillator-based or semiconductor, are tailored to this energy, so no special precautions regarding detection are needed; every BSE detector installed in a particular SEM will work when we bias the sample and create a CL in its surroundings. Alternatives are listed in Ref. [8].

Slower electrons penetrate more shallowly into targets so the information depth of low-energy electron imaging shortens. Increased surface sensitivity provides enhanced information about the topography and possible coating of the surface, naturally including any contamination that may have concealed the surface to be examined. At hundreds of electronvolts and below, we enter the branch of instrumentation normally employed by surface physics methods such as low-energy electron diffraction, photoelectron, or Auger electron spectroscopy, in which ultrahigh vacuum (UHV) conditions are used and any sources of hydrocarbons have to be avoided. Experience has confirmed this assumption, although there is still the chance of improving surface cleanliness even under standard high (though dry) vacuum conditions where we have to remove primarily the adsorbed hydrocarbons loaded with the sample.

http://dx.doi.org/10.5772/62054

Electrons at energies below 50 eV have proven themselves in removing the hydrocarbon molecules instead of decomposing them and creating the well-known carbonaceous contamination marking previous fields of view in the SEM [18,27,28]. This kind of cleaning caused, for example, the transmissivity of single-layer graphene to increase 2.5 times after bombardment with a dose of 1.3 Ccm^{-2} of 40 eV electrons [18].

Here we should provide answers to two frequently asked questions: How flat/smooth should the sample surface be? The CL field strength is usually about 2 or 3 kV/mm, i.e. 2 or 3 V/μm. Similarly strong lateral fields are generated with steeply inclined facets of surface unevenness details, with protrusions being more critical than dips. The tolerable relief height then depends on the landing energy we want to use. Protrusions in units of micrometers in height are well acceptable down to tens of electronvolts, whereas, at units of electronvolts, we can observe certain image deformations around surface steps around 1 μm in height. However, gently undulating surface structures with a p-p distance in units of micrometers are usually not apparent at all as disruptive damage to the image but are visible as surface topography details.

Can we image nonconductive samples? When placing a slab made from an insulating material on the conductive base of the sample holder and biasing the holder with respect to the surrounding ground, we get a situation equivalent to a capacitor with multilayer dielectric, composed here of a vacuum and a nonconductive sample slab. The potential drop then splits to both media according to their dielectric constants, so we get a somewhat lower negative bias on the sample surface than that led to the holder. However, when applying "good practice" in calibrating the landing energy scale, which consists of identifying its zero according to the disappearance of all topography details on a sample area as flat as available, we do not need to know the potential drop over the sample. What remains is to consider the landing energy scale modified according to the division between the sample and vacuum of every volt added to the holder bias, thereby giving the sample surface potential changed by less than 1 V. The potential drop across the sample can be detected when also checking the zero landing energy on the holder aside from the sample and the difference in both holder biases so determined can be used to correct the landing energy scale.

Since around a decade ago, the main producers of electron microscopes have been offering a cathode lens mode in their new instrument types, calling it beam deceleration, gentle beam, or decelerating optics. However, advances in the collection of new application results have been slow and seem to have been accelerating only quite recently as the Microscopy and Microanalysis Meeting 2015 has indicated. Owners of older SEMs are not completely excluded from enjoying the advantages of the CL mode in their instruments: simpler microscopes, more feasible adaptation; see Ref. [7]. The detection issue is solved by any functional BSE detector. All that is necessary is to insulate the sample from the stage and to connect it to a high-voltage feedthrough into the sample chamber. It is usually sufficient to insert the sample into a capsule made from a good insulating material and then load this capsule onto the stage. What remains is to connect the sample to the feedthrough in a way that does not cause havoc in the sample movements. More obstacles appear, of course, if the sample is loaded via an airlock. Nevertheless, plenty of positive experience was gathered with such adaptations in the 1990s.

4. Applications

Since the CL mode was first used for the practical examination of SEM samples, we have continued to map various families of samples in order to identify possible added value introduced by this mode. If the results of such a survey are to be efficiently demonstrated, it would seem to be natural to compare side-by-side micrographs taken at conventional energies at several kiloelectronvolts or more, with CL mode images differing not only in terms of the significantly reduced landing energy of electrons but usually also in terms of the collection of a broader or even complete angular distribution of backscattered electrons. In this chapter, we will follow this style of presentation for a selection of sample types often appearing in SEM practice.

4.1. Surfaces

The most straightforward expectation connected with decreasing the landing energy of primary electrons on the sample is their reduced penetration into the sample. Shortened information depth, along with reduced lateral diffusion, produces enhanced surface sensitivity, i.e. improved visibility of topographic details such as tiny dips, protrusions, and ridges, and also the sudden appearance of very thin surface coverage that is fully transparent and invisible at conventional energies. When comparing the two frames in Figure 4, we can identify examples of both these types of differences. Here, the penetration depth of primary electrons is the main factor; however, as shown below, the contribution of signal electrons from a broad range of polar angles of emission also plays a role.

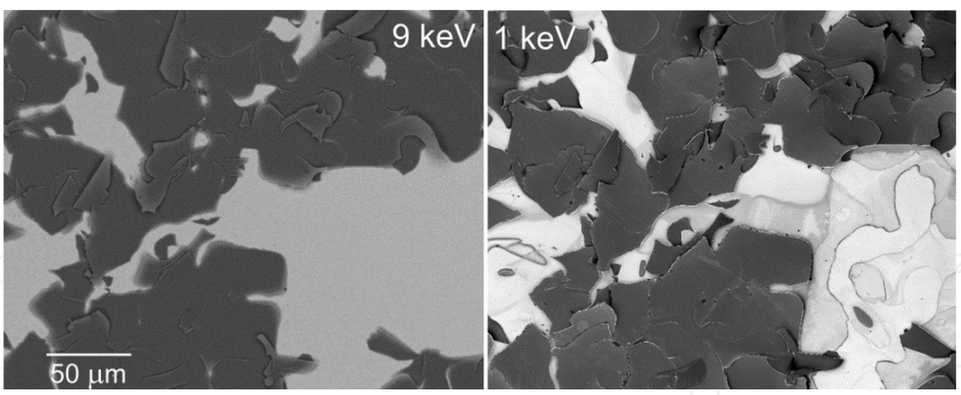

Figure 4. Carbon nitride film 200 nm in thickness deposited on a silicon substrate covered by around 5-nm-thick native SiO_x, delaminated due to compressive stress, CL mode, primary energy 9 keV.

The example shown in Figure 5 addresses a typical three-dimensional (3D) sample in which imaging of a highly complex surface structure requires the dimensions of the interaction volume of primary electrons in the material not exceeding the dimensions of the 3D details to be observed. The averaging of information over the volume from which BSE are capable of reaching the surface to be emitted smears out details smaller than, for example, hundreds of nanometers at 10 keV. Nevertheless, the interfaces between "bubbles" and vacuum are

http://dx.doi.org/10.5772/62054

reproduced relatively sharply because the signal in pixels situated closely outside these bubbles does not include electrons diffusing through the material, so that the averaging is abruptly terminated at the margin.

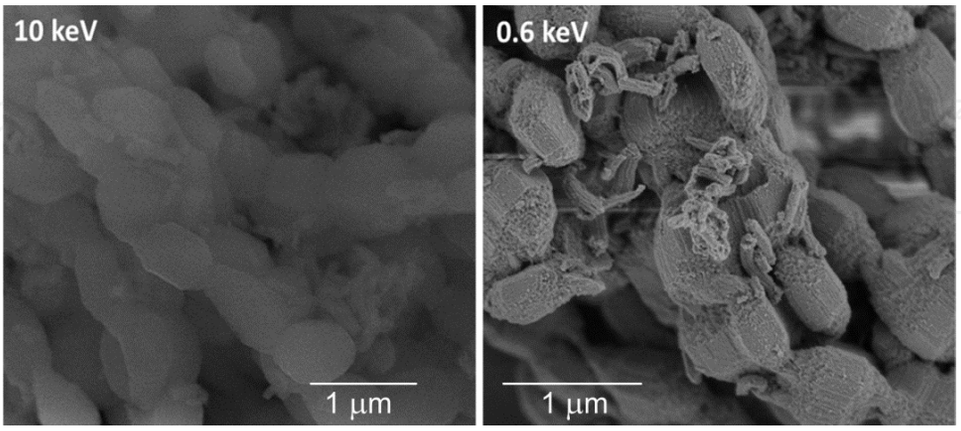

Figure 5. Mesoporous carbon nitride foam as a carrier for catalytic gold nanoparticles, CL mode, primary energy 10 keV.

We might complete the paragraph concerning surface imaging with one problematic issue often mentioned where low electron energies are concerned. It has been said many times that decreasing the energy of incident electrons leads to reduced radiation damage of the sample. On one hand, every electron brings less energy, so certain inelastic events may no longer take place. On the other hand, the penetration depth shortens with decreasing energy faster than linearly, so dissipation of the delivered energy takes place in significantly shallower subsurface layer at growing spatial density of the dissipated power. From this point of view, the radiation damage connected with mechanisms active down to any particular low energy grows downward this energy. A well-known example is the creation of "black rectangles" marking the fields of view bombarded for a longer time with illuminating electrons. This carbonaceous contamination comes from the decomposition of adsorbed hydrocarbons under the impact of electrons. The more intense frames of these rectangles are caused by diffusion of the hydrocarbon molecules from the surrounding, so the phenomenon might be partly suppressed if we first immobilize the hydrocarbons around the next field of observation by electron impact. It is easy to verify that the intensity of this kind of contamination increases down to 100÷200 eV, i.e. to the fuzzy threshold of the shortest inelastic mean free path of electrons in solids, and only then fades out. Below some 50 eV, the radiation damage may usually be neglected.

4.2. Immersed objects

In the previous paragraph, we presented samples with a heterogeneous or buckled or discontinuous surface coating and with a ragged spatial structure containing tiny protrusions and depressions. However, even when the sample is ideally flat and smooth and not covered with any thin layer, we may be confronted with imaging issues in cases in which very small objects are immersed just below the surface with the object tops lying on the same level as the

neighboring surface. Good examples are precipitates in alloys prepared with an overall flat and smooth surface as shown in Figure 6. Here, we compare standard SEM micrographs at 10 keV in the BSE and SE signals. Precipitates are apparent in both frames, but most appear fuzzy. In the BSE image, the main contrast contribution comes from the atomic number difference, i.e. "material contrast". The precipitates are composed of either Mg_2Si or Mg_3Si [30,31], so the difference of the mean atomic number with respect to that of Al is only 0.33 or 0.5, which is obviously sufficient for good contrast. The relatively sharp edges of the precipitates indicate an in-depth thickness much smaller than the information depth of the imaging, which reveals the margin information borne only by the BSE scattered in the narrow upper part of the pear-shaped interaction volume. In contrast to this, the SE appearance of the precipitates is fuzzier due to the contribution of the SE2 species released by BSE returning from the sample depth in a broad flux. The CL mode frame, thanks to much smaller interaction volume, not only shows quite sharp edges of the precipitates but also reveals their internal structure with a bright frame and dark core. The explanation of the internal structure obviously also has to incorporate the crystal structure of the precipitates, providing a specific contrast contribution when a sufficiently broad angular range of BSE is acquired, as we will show below.

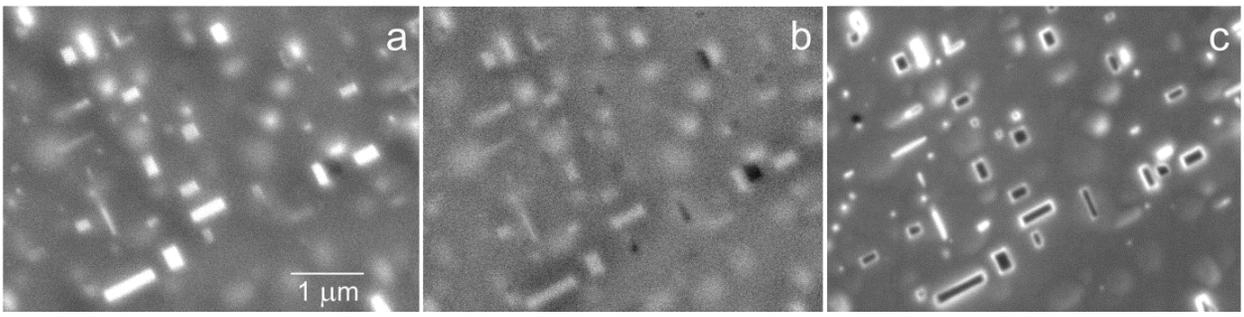

Figure 6. Precipitates in Al-1.0 mass% Mg_2Si with 0.4% excess Mg alloy, annealed, quenched, and age hardened: standard BSE image at 10 keV taken with a coaxial detector (a), SE image at 10 keV taken with a side-attached Everhart-Thornley detector (b), and the cathode lens image at 1,500 eV for 10 keV primary energy (c).

4.3. Local crystallinity

At high or medium electron energies, i.e. down to hundreds of electronvolts, the local crystallinity of the sample manifests itself in the channeling contrast. Incoming electrons are scattered at a rate proportional to the density of atomic planes they face, and if dense planes are inclined or even perpendicular to the surface, electrons penetrate into depth along interatomic channels and the probability of their backscattering decreases. For this reason, we get a BSE signal dependent on the local crystallinity. At hundreds of electronvolts, the scattering on atom cores begins to be combined with interaction with electrons in the target [32], and at even lower energies, below some 30 or 40 eV, the scattering is on a pure electron basis. If the incident electrons are of an energy close above the vacuum level, after gaining the inner potential, they appear within unoccupied energy bands that are already modified with the internal 3D potential distribution from the parabolic bands of free electrons and hence acquire a dispersion characteristic to the crystal system and its spatial orientation. Effectively,

the impinging electrons convert into Bloch waves and move preferentially in directions of a high density of states. The reflectivity of electrons this slow then depends on the local density of states in the direction of impact of electrons on the crystal, i.e. electron states coupled to the incident electron wave. These have a surface-parallel wave vector component equal to that of the incident wave or differing in any surface reciprocal lattice vector [13,15,33].

We have already mentioned the enhanced crystal information contained in the BSE signal acquired at angles further from the surface normal. As we see in Figure 7, the polar-angle-sorted BSE imaging is composed of multiple contributions. The sample shown in this figure does not exhibit any local material contrast of details distinguishable at the given magnification, so we can compare contrasts of the grain orientation, grain boundaries, and the surface topography. Visibility of the grain boundaries dominates nearest to the optical axis; at higher angles and at angles near to 90°, we get the topography, whereas, between these angular intervals, the signal dependence on the grain orientation is most pronounced. Possible material contrast would appear at angles near to the optical axis. When assessing this figure, we should take into account that SE are also accelerated in the cathode lens field and then appear detectable very near to the optical axis. Their contribution is responsible for the edge effect visible in Figure 7a. Thus, as follows from Figure 7, the crystal contrast is best acquired at emission angles above 40° or 50° that are abandoned in conventional configurations of BSE detectors.

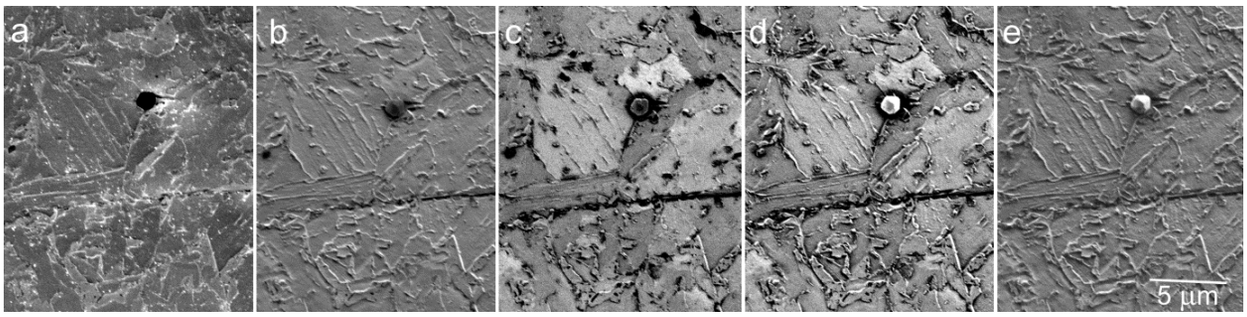

Figure 7. TRIP-aided bainitic ferrite (TBF) steel, imaged in the CL mode at 500 eV with primary energy of 4.5 keV, micrographs taken within the polar angle ranges of backscattered electrons: 0°–15° (a), 17°–26° (b), 28°–42° (c), 44°–61° (d), and 63°–90° (e).

Now, let us turn to the electron energy dependence of the crystal contrast. As Figure 8 shows, the acicular martensite structure is best visible around 500 eV, whereas, at kiloelectronvolt energies and also at tens of electronvolts, this kind of contrast is much weaker. The proposed explanation is as follows: at units of kiloelectronvolts, the image information is averaged within the depth range exceeding 100 nm, so the thin martensitic whiskers variously rotated with respect to the electron impact direction are averaged as regards their channeling ability, which reduces the resulting contrast. Moreover, this micrograph was taken with the cathode lens off, so only the BSE moving along straight trajectories within a rather narrow angular interval were acquired and the high-angle BSE providing more crystal contrast were abandoned. An optimum balance between the information depth and the thickness of the contrast producing structure details appears somewhere around 500 eV, and here, the full emission of

the BSE is also detected. At 50 eV, the information depth falls below 1 nm, to which subsurface layer the structure features responsible for the contrast obviously do not raise. Having the information depth incorporating only two to three atomic layers, we may see only the surface reconstructed crystal that tends to convert differently oriented grains to rather unified structure. Another view might be based on a general fading of the channeling contrast at these energies.

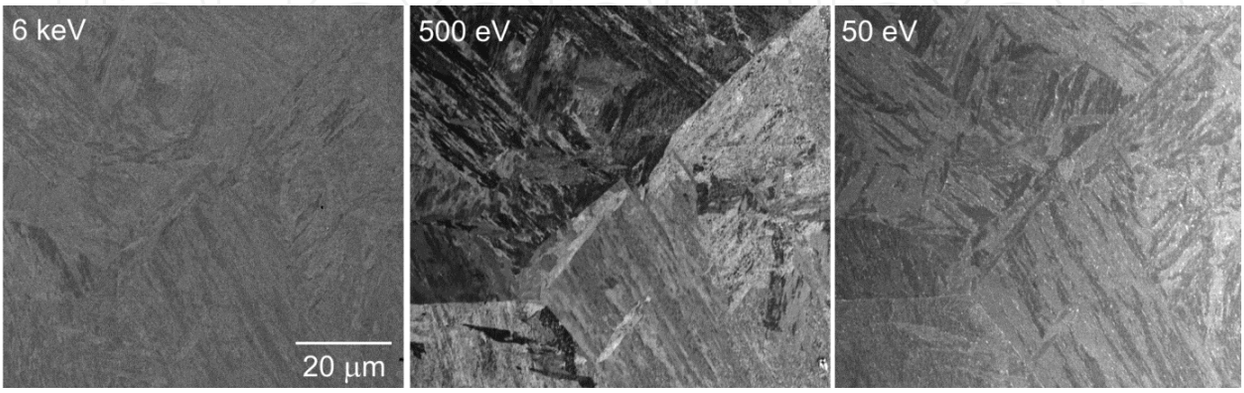

Figure 8. Martensitic steel imaged in the CL mode with a primary energy of 6 keV.

Figure 9 refers to the above-mentioned contrast mechanism connected with the local density of electron states. We have to restrict ourselves to energies at which the absorption of hot electrons, proportional to the imaginary part of the crystal potential, is sufficiently low in order not to overwhelm the expected phenomenon [34]. As we see in the EBSD map, two of the Al grains in Figure 9, grains A and B, are near the orientation (111). Their reflectivity curves in Figure 9d are really quite similar, at least as regards the positions of the maxima and minima. The orientation of grain C is nearer to the middle of the color-coding stereographic triangle and the corresponding reflectivity dependence differs mainly below 20 eV. Grain D with an orientation near to (100) has a very different reflectivity. Obviously, having available reference curves for fundamental orientations of a particular crystal, we may be able to identify orientations of grains in a polycrystal of the same material [15]. As a potential alternative to the commonly used EBSD method, this approach would require an investment of decades of effort in data processing algorithms and tools, as was made during EBSD development. In principle, the low-energy reflectivity method offers better spatial resolution available at lower energy with a nontilted sample and faster data acquisition, thanks to only one-dimensional data collected for every pixel.

4.4. Internal stress

In heavily deformed materials, some residual internal stress remains even after any deforming action is terminated. Consequently, elastic or plastic deformation of the crystal or of the grains in a polycrystal exists and should be observable in view of the importance of this parameter for material development and diagnostics. In relaxed grains, the BSE signal level revealing the penetration of primary electrons along the interatomic channels is constant over the grain area

http://dx.doi.org/10.5772/62054

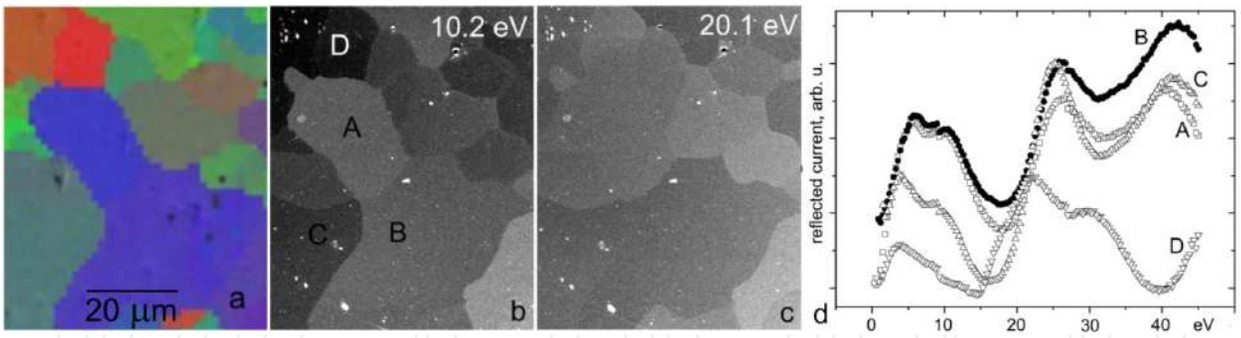

Figure 9. Identification of crystal grains in Al on the basis of reflectivity of very slow electrons: EBSD map (a), CL mode micrographs (b and c), and energy dependence of the reflectivity of selected grains (d) (reproduced from Ref. [29]).

up to the grain boundary where dislocations and other defects are normally clustered. If microscopic deformations exist inside a grain, the conditions for the channeling of electrons vary even inside the grain, which leads to signal variations proportional to the extent of deformation and correspondingly distributed. Gradual signal variations without abrupt changeovers are characteristic, as Figure 10 demonstrates on a margin of the Vickers indent. On the inclined wall of the indent, we may observe plastically deformed grains of internally varying brightness owing to changes in crystallographic orientation, whereas, outside the indent, the grains are of a constant signal over their full area.

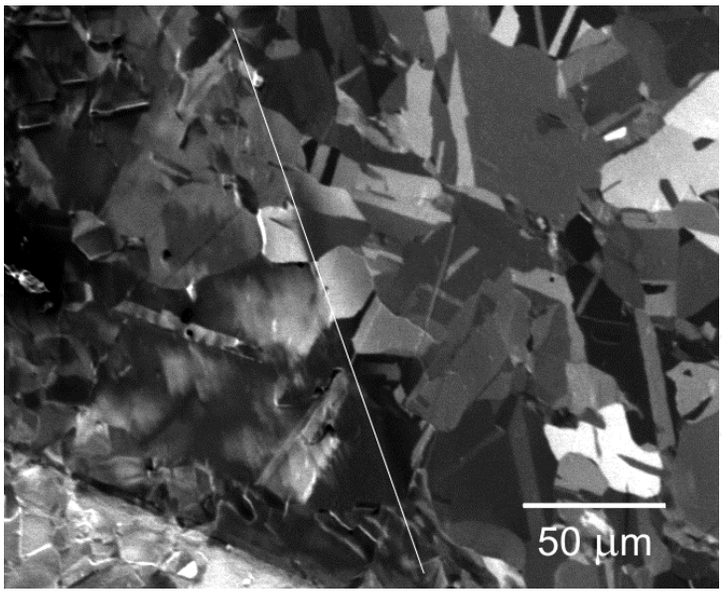

Figure 10. Margin of a Vickers indent in an annealed polycrystalline Cu sample, CL mode at 500 eV showing the residual stress distribution inside the indent (left) and relaxed grains (right).

Figure 11 demonstrates the dependence of the visibility of grain deformation on the energy of electrons. Similarly as in Figure 8, we have the contrast culminating around 500 eV and nearly invisible at the nonreduced primary beam energy or at 50 eV. The reasons for this phenomenon

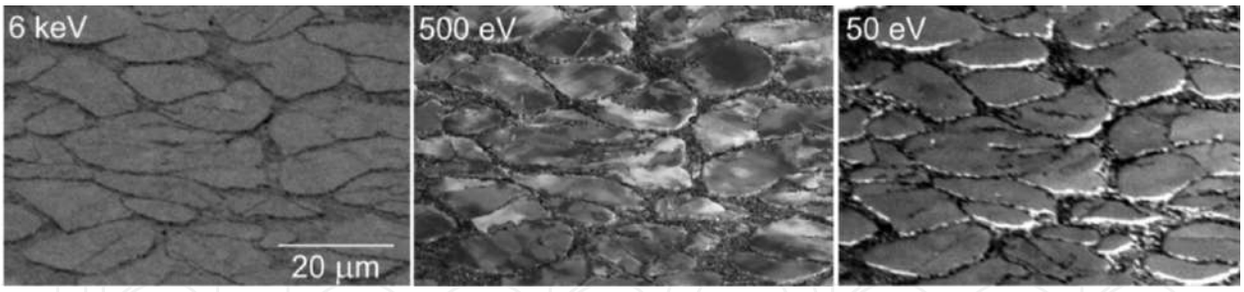

Figure 11. X210Cr12 ledeburitic steel heated to a semisolid state, heavily deformed and cooled, CL mode micrographs for the primary energy of 6 keV.

are very probably identical to those regarding contrasts between relaxed grains, as discussed in the previous paragraph.

4.5. Semiconductors

The measurement of the local density of active dopants in semiconductors is of crucial importance for semiconductor technology in its all versions and phases, particularly as regards integrated circuits. While silicon wafers recently began achieving 45 cm in diameter, the characteristic dimensions of circuit structure details have been stepwise diminished from 45 to 32 nm and then to 22 nm, allegedly with 16 nm as the future prospect. The gigantic number of doped patterns excludes any true interoperational checks during production, but the possibility of measuring both the critical dimensions and true local density of a dopant still poses a difficult task for instrumentation designers. Thanks to its nondestructive application, the flexible size of the field of observation, resolution below 1 nm, and possible response to all sample characteristics including topography, chemistry, crystallinity, and electronics, SEM is traditionally considered the most suitable diagnostic method. However, important obstacles have hindered the development of this SEM application. The measurement of the critical dimensions of patterns faces the edge effect, i.e. overbrightening of the margins of surface steps imaged with secondary electrons that are also emitted from the sidewall as an extended surface. The edge effect disappears when the penetration depth of primary electrons drops beneath the escape depth of SE; with silicon sample, this happens at a landing energy of around 300 eV [35], which requires the use of the CL mode. Although the visibility of doped patterns was verified long ago [36], the explanation of dopant contrast has fluctuated between a great many alternatives. A review of this topic up to 2000 [37] considered the governing factor to be the difference in ionization energy between p- and n-types and its balancing by above-surface electric "patch fields". Later works incorporated below-surface fields on the junction between semiconductor and carbonaceous contamination [38] and the filtering action of the surface potential barrier [39]. The first observations of doped semiconductors in the CL mode [40] provided data about the contrast dependence on the external electric field of the CL and on vacuum conditions and the configuration of the detector. An explanation of these observations relied on the influence of surface passivation and the CL field causing the dopant contrast enhanced with respect to conventional SEM imaging.

This chapter does not aim to make a decision about the proposed models of the dopant contrast mechanism but merely to gather the most important experimental data. In order to avoid the

http://dx.doi.org/10.5772/62054

low repeatability of data recorded in the past on series of samples with only one density of dopant per sample, which was to a certain extent the result of nonidentical surface treatment causing differences in the potential barrier, our samples were prepared with patterns doped by four different dopant densities. Figure 12 confirms the main relation known for a long time, namely, the higher imaging signal from p-type patterns compared to n-type patterns. As we see, the dopant contrast increases from 4 keV to 1 keV. At 4 keV (and primary energy 7 keV), SE are accelerated to 3 keV before detection, which is not sufficient to obtain a high signal from a scintillator covered with a metallic layer. This change of landing energy also causes acquisition of a broader flux of BSE, which are collected completely at 1 keV. Simultaneously, the slowest SE escape detection through the central detector bore, although faster SE still contribute to the image. However, this finding indicating an increase in contrast due to the loss of the slowest SE somewhat contradicts the measurement of the p/n contrast made with energy filtering of the SE in which the contrast carried by SE up to 10 eV was higher than that for the full SE emission [41]. In our case, SE below 3 eV escape detection fully, whereas, at higher energies, the central parts of the collimated SE flux are not detected. An important factor is that, at around 1 keV, the image contrast is reliably proportional to the dopant density and can be quantified for the sake of density measurement.

When going down with landing energy of electrons, the dopant contrast in Figure 12 diminishes and at tens of electronvolts inverts, giving the p-type patterns darker than the n-type background. No explanation has yet been proposed for this phenomenon, connected solely with the BSE emission because SE completely escape through the detector bore. Down to units of electronvolts, this inversed contrast is enhanced, but its dependence on the dopant density is much weaker. Near to zero energy, one more contrast inversion appears and we again get brighter p-type silicon. This effect is discussed below.

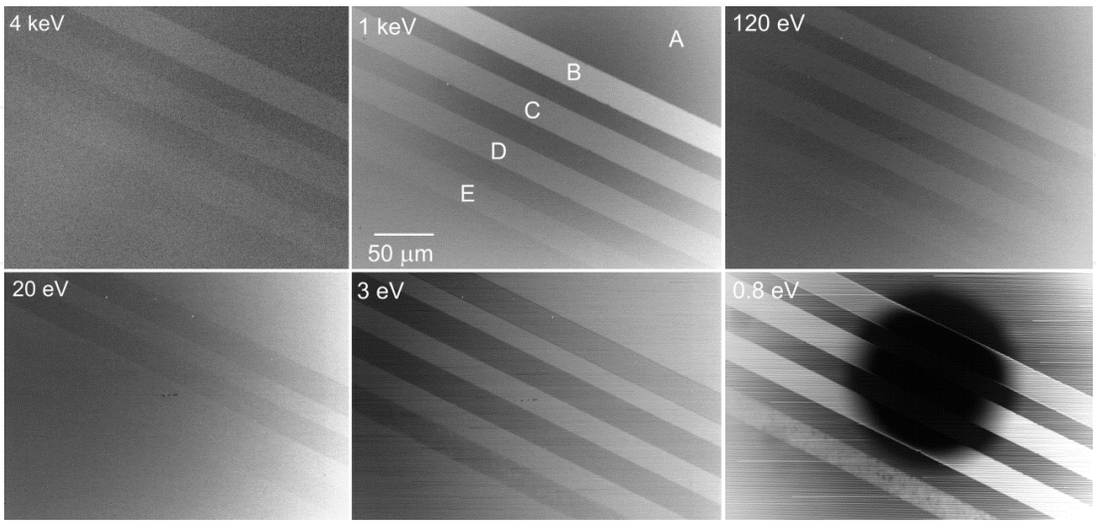

Figure 12. p-type doped patterns of dopant concentrations: 10^{19} cm^{-3} (B), 10^{18} cm^{-3} (C), 10^{17} cm^{-3} (D), and 10^{16} cm^{-3} (E) on an n-type substrate (10^{15} cm^{-3}, A), etched in the Buffered Oxide Etch, CL mode, primary beam energy 7 keV, current 500 pA.

It is no great surprise that the "opposite" structure of n-type patterns on a p-type substrate in Figure 13 exhibits an opposite brightness relation with darker strips. Again, we have the contrast increasing toward 1 keV, now with a less pronounced proportionality between the contrast and the dopant density. At tens of electronvolts, the contrast inverts again and becomes more dependent on the dopant density. No important change takes place near the mirror image.

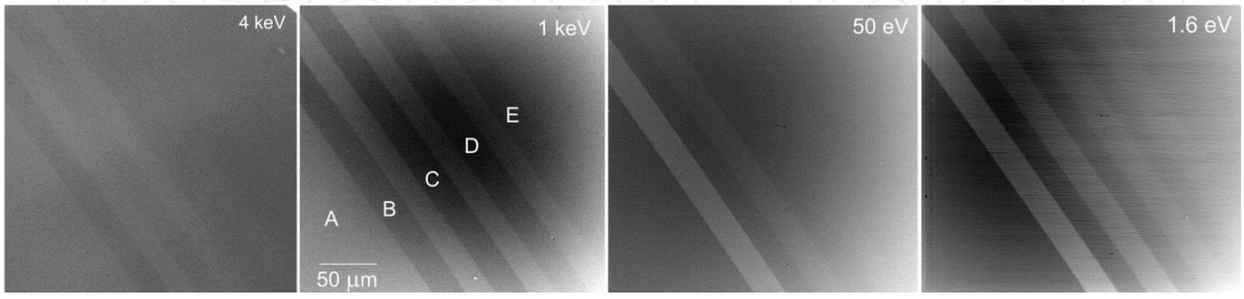

Figure 13. n-type doped patterns of dopant concentrations: 10^{19} cm^{-3} (B), 10^{18} cm^{-3} (C), 10^{17} cm^{-3} (D), and 10^{16} cm^{-3} (E) on a p-type substrate (10^{15} cm^{-3}, A), etched in the Buffered Oxide Etch, CL mode, primary beam energy 6 keV, current 500 pA.

Important findings concern the influence of the surface status on the observed contrasts. Particularly, under standard vacuum conditions, when carbonaceous contamination is always present, we observe contrast dependence on the rate of contamination, impact angle of primary electrons, electron dose, detector geometry and position, etc. [42]. However, even the mere storage of an originally etched sample in air for several weeks leads to inversion of the contrast in the UHV microscope (see Figure 14).

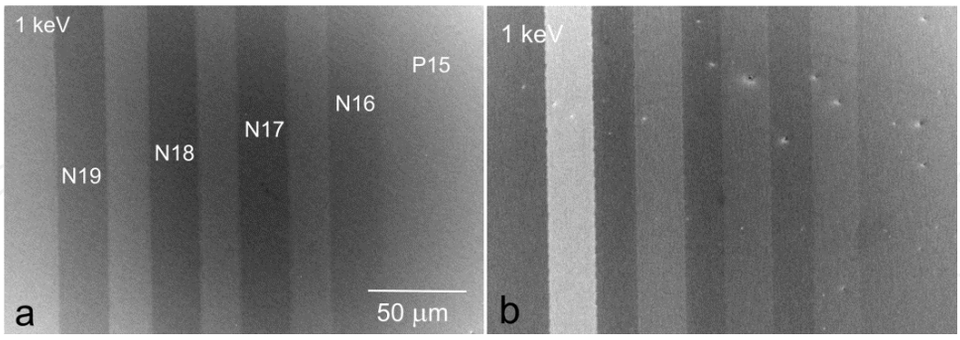

Figure 14. n-type patterns on a p-type substrate (see Figure 13) after etching in the Buffered Oxide Etch (a) and after several weeks in air (b).

Now, let us return to the ultimate inversion of the p/n contrast on a p-type pattern/n-type substrate sample near zero landing energy. Here, we obtain an extremely high signal from p-type patterns though with variously shaped black dots (Figure 15). The measurement shows that we are getting a "full" contrast here between the total beam current and no current. The explanation was based on the injection of electrons in the p-type patterns and their recombi-

http://dx.doi.org/10.5772/62054

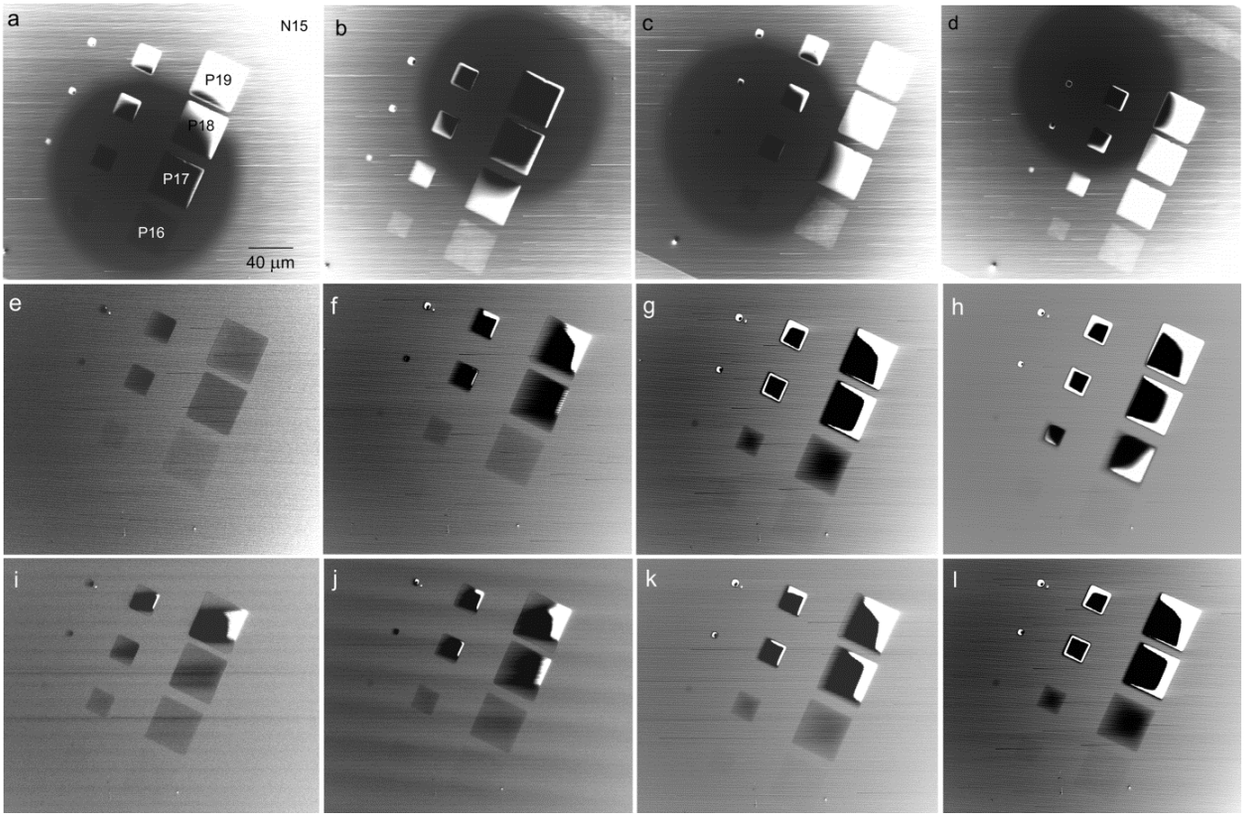

Figure 15. Total reflection phenomena on p-type doped patterns: lateral shifts of the pattern group influencing which pixels illuminate the active detector area around the central bore (a–d); dependence of pattern charging on the landing beam current: 30 pA (e); 100 pA (f); 600 pA (g); and 1.5 nA (h); and dependence on the electron dose proportional to the pixel dwell time: 560 ns (i); 1.76 μs (j); 5.36 μs (k); and 48.56 μs (l).

nation and on the ability of the small surface charge around 1 V thereby created to decrease the very low landing energy of incident electrons near enough conditions of total reflection [43]. The total reflection of the primary electron beam is directed toward the above-sample detector based on the bored scintillator disc, so we get white pixels where the reflected ray hits the scintillator surface and a black area where it hits the bore.

In Figure 15, we see the phenomenon dependent on the mutual position of the group of patterns and the detector and also on the beam current and dose. Obviously, the emergence of this phenomenon depends on a certain relationship between the electron dose sufficient to cause it and dopant density, which may offer another tool for measuring this density.

4.6. Thin sections

An extremely important family of microscopic samples consists of thin sections of tissues or more generally of live matter and various organic materials. These samples are usually amorphous and composed of light elements. For microscopic observation, they are cut into layers of submicrometer thicknesses and observed in TEM or STEM, traditionally using electrons in a range of hundreds of kiloelectronvolts and more recently of tens of kiloelectron-

volts. An exception to this is low-voltage TEM operated at around 5 keV [44,45]; the success of this instrument is based on partially overcoming difficulties with the achievement of a sufficient image contrast in structures composed of light elements. In order to get good image contrast, sophisticated preparation procedures have been elaborated, particularly for tissue sections. These include fixation in various agents, immersion in resins, postfixation with osmium tetroxide, and staining with agents such as uranyl acetate or lead citrate. High contrast is then obtained where the heavy metal species from the chemicals used in preparation are located. Unfortunately, only some details of the structure are highlighted in this way, mainly with staining. When using STEM equipped with a CL mode and decreasing the landing energy of electrons, we observe a dramatic increase in contrast even when no heavy metal-containing substances are used in preparation [16] (see Figure 16).

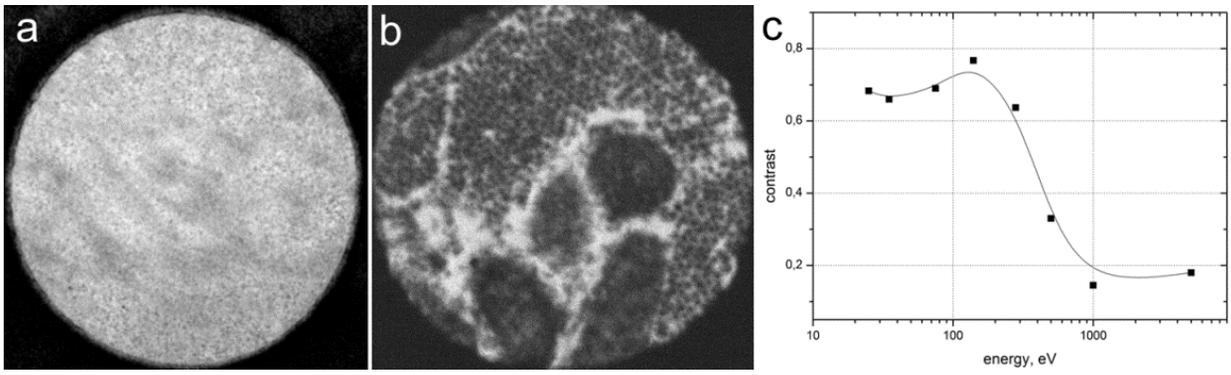

Figure 16. Section of mouse heart muscle, not fixed with osmium tetroxide and not stained: 10 nm section imaged by conventional TEM at 80 keV (a), CL mode micrograph taken at 500 eV with a primary energy of 4.5 keV (b), and energy dependence of the contrast of this sample in the CL mode (c).

An important finding made in a pioneering study [16] concerns changes in the embedding resin. It has been known that the resin is partially "radiation damaged" under electron bombardment with the consequence of the increased electron transmissivity of sections, but this increase was moderate only. The rate of this effect was compared at various electron energies, and whereas 5 keV STEM increases the transmitted flux two times after a dose of about 5×10^{-3} Ccm^{-2}, at 500 eV, the increase was 20× at a doubled dose [16]. The idea is that, under electron impact, the resin is partly depolymerized and monomers are then released from the surface; no losses in the observable structure details have been discovered after this "ultimate" preparation step performed in situ.

Sections for ultralow-energy STEM have to be very thin, preferably below 10 nm [17]. These are transparent down to 500 eV if "electron bombardment thinning" is utilized and micrographs have even been taken at tens of electronvolts. The advantages here include averaging of image details over a much shorter trajectory across the layer, which may reveal some features, usually bright spots, not observable in thicker sections at any electron energy.

The application of ultralow-energy STEM in polymers, polymer blends, and composites forms a branch to be examined next.

4.7. 2D crystals

Intuitively, crystalline layers should be more transparent for slow electrons than amorphous sections because of the expected possibility of channeling among atomic planes or columns. For this reason, ultralow-energy STEM with the cathode lens mode has been applied to 2D crystals, firstly to graphene. The first results were achieved when comparing the Raman spectroscopy identification of flakes of a certain thickness with STEM observation [46]. Even flakes exhibiting a Raman spectrum corresponding to single-layer graphene were found to be composed of tiny flakes of various thicknesses and small holes. This finding argues in favor of introducing CL-mode STEM as an acknowledged method for the diagnostics of graphene and other 2D crystals.

Because the available graphene samples are generally composed of flakes only rarely exceeding micrometer sizes and usually overlapping each other at least partly, we need first and foremost to be able to obtain sufficient contrast between sites differing in thickness by a single layer of carbon atoms. As we see in Figure 17, this demand is met at about 100 eV in the transmission mode, whereas this kind of contrast is not available in the BSE signal.

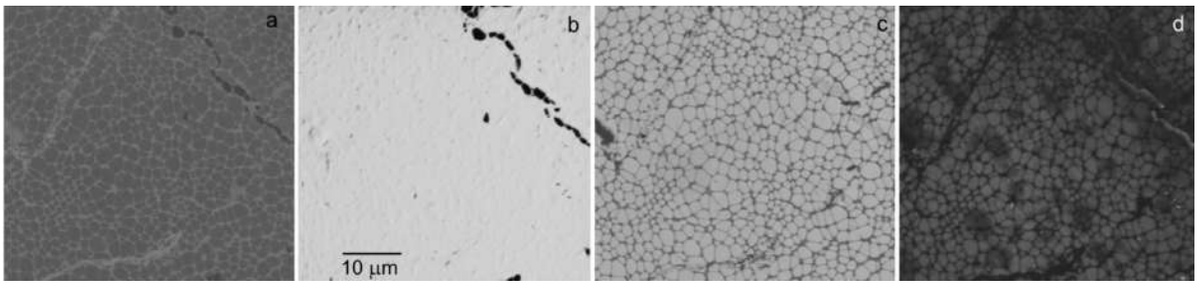

Figure 17. CVD graphene samples deposited on lacey carbon lying on a copper mesh, commercially available sample declared as three- to five-layer graphene: reflected signal for 1 keV (a) and 100 eV (b) landing energies and transmitted signal for 1 keV (c) and 100 eV (d).

One sort of commercially available graphene is a polycrystalline, CVD prepared material deposited on lacey carbon with eyes of up to 1 or 2 μm in diameter, which was used in our study. In Figure 18, we see the layer-by-layer contrast at higher magnification in a standard vacuum microscope, together with a detailed frame showing the polycrystalline structure of individual domains, though of continuous single-layer graphene (1LG hereinafter). These samples have been used for the measurement of the electron transmissivity through various numbers of graphene layers, assuming that the total area of nucleation centers visible in Figure 18a is negligible when averaging the transmitted signal over the lacey eye, and similarly, the existence of the domains does not influence the result.

We can notice in Figure 18d the electron penetration through the sample even at 4 eV. In fact, transmitted current was measurable down to or even below 1 eV. This enabled us to measure the transmissivity across the full energy scale from kiloelectronvolts to 1 eV. The result in Figure 19 was surprising in view of the expected increase in the inelastic mean free path of electrons below about 50 eV, which is not only generally observed [47] but also results from

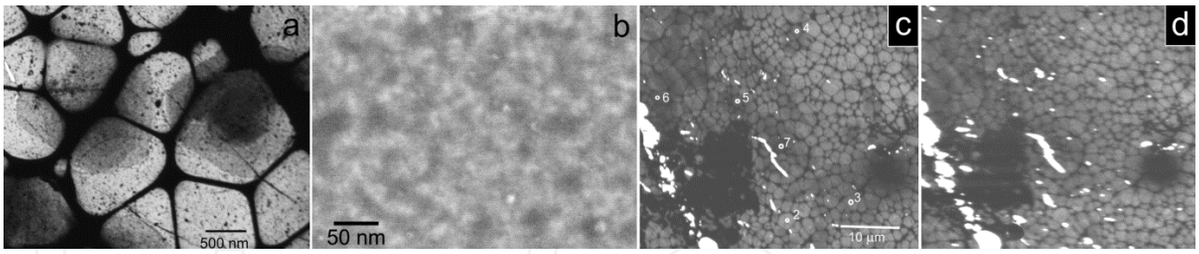

Figure 18. CVD graphene (see Figure 17) in transmitted electrons at higher magnification, 220 eV (a) and 1 keV (b), and at lowest energies, 40 eV (c) and 4 eV (d).

calculations [48]. The explanation should be sought in the fact that graphene in flakes sufficiently exceeding units of nanometers in size does not have an energy gap between the valence and conductance bands meeting at the Dirac point [49]. This causes interband transitions as the inelastic scattering mechanism working down to arbitrarily low energy losses in scattering events.

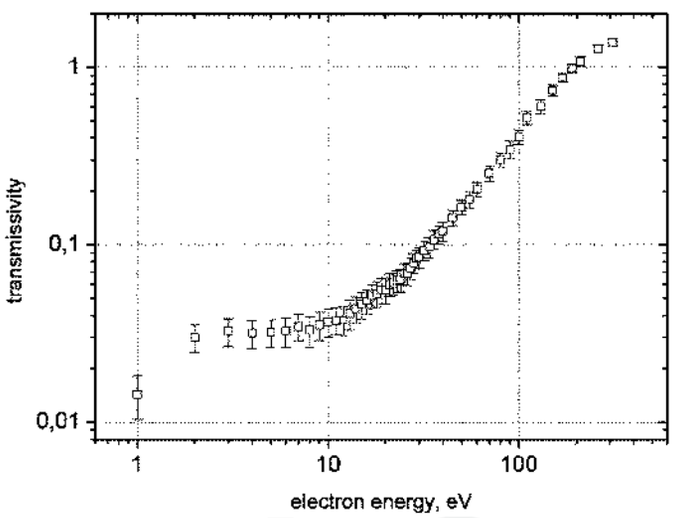

Figure 19. Energy dependence of the transmissivity of slow electrons through single-layer graphene.

In Figure 19, we see the transmissivity apparently exceeding 100% above 200 eV. This effect is caused by SE released inside the sample with original direction of movement toward the bottom surface where they are emitted and accelerated toward the detector together with the transmitted primary electrons. The excess current is then balanced from the earth. A detailed measurement of the electron transmissivity has been performed for up to 7LG. The ratio of transmissivities 1LG/7LG was found to be largest at 40 eV (over 6), so this energy is recommended for the reliable counting of graphene layers [18].

Electron microscopy of graphene below 10 eV was also examined in the reflection mode in a low-energy electron microscope (LEEM) [50]. The BSE signal was found oscillating in such a way that n layers of graphene (grown on various surfaces or free standing) produce n-1 minima in the reflectivity between 0 and 8 eV [50,51]. We have also verified this relation in STEM and

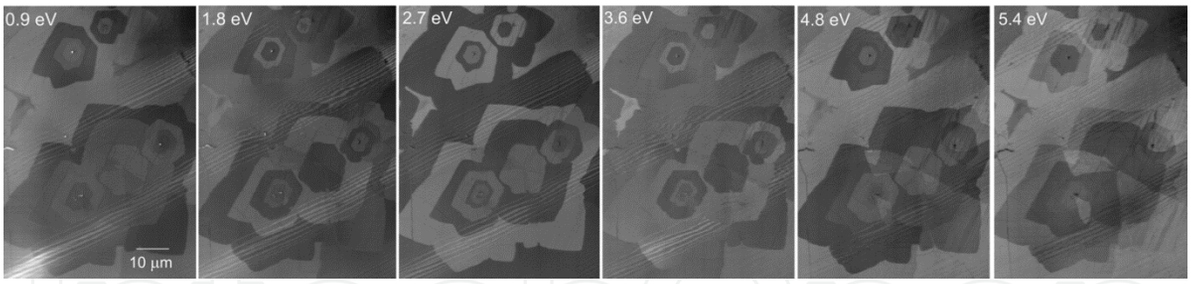

Figure 20. Multilayer graphene deposited by the CVD technique on a Cu foil, CL mode micrographs taken for the primary energy 6 keV.

were even able to confirm experimentally the second band of oscillations predicted by calculations in the range between 13 and 20 eV [27]. Oscillations are demonstrated in Figure 20 on a stack of multiple layers of graphene.

Finally, let us return to the "radiation damage" created by very slow electrons, mentioned above in connection with the decomposition of the resin in which the tissue section was embedded. Electrons below 40 or 50 eV were found to effectively clean the graphene samples increasing their transmissivity: a dose of 1.5 Ccm^{-2} of 40 eV electrons increased the transmissivity of 1LG 2.5 times [18]. With graphene as a single atomic layer, there are no possible doubts about the mechanism of this radiation damage — if the sample is not bored, the only alternative is the removal of adsorbed gases, which was observed even under standard vacuum conditions. We suppose the removal of the hydrocarbon molecules instead of their decomposition normally generating the carbonaceous contamination, as happens immediately when increasing energy to, say, 200 eV. This kind of in situ surface cleaning promises a method for some surface studies performed outside UHV.

In Figure 21, the cleaning of graphene with slow electrons is shown on decreased reflectivity and increased transmissivity of longer bombarded parts of the fields of view.

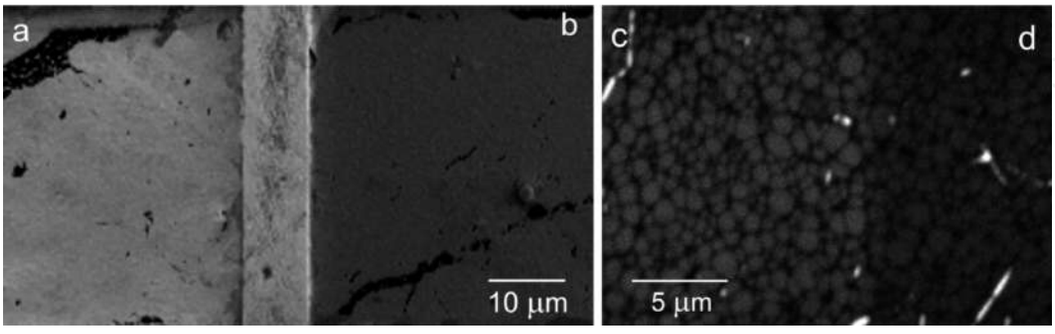

Figure 21. Demonstration of the cleaning effect of bombardment with very slow electrons, single-layer graphene, CL mode at 30 eV: original state shown in reflected (a) and transmitted (d) signal, decreased reflectivity (b), and increased transmissivity (c) after impact of about 1 Ccm^{-2} of 30 eV electrons.

An observation of graphene samples grown on substrates at very low energies also makes it possible to distinguish between overlayer and underlayer growth of the second layer. A

decision is made according to the comparison of micrographs taken at few hundreds of electronvolts, when all the "wedding cake" of stacked layers is visible, with a frame at units of electronvolts when we see only the topmost layer [27].

5. Conclusions

During a little more than 20 years of laboratory existence and nearly a full decade since the introduction of a commercial device, the cathode lens mode has slowly ceased to be considered a methodological novelty. If any future review of the method is to be written, its content will probably be limited to a particular type of samples and place the emphasis on models of contrast mechanisms rather than the mere comparison of the traditional and new appearance of micrographs. However, this time the older approach has been chosen. We have seen above that not all effects observed even when examining quite common samples have already been satisfactorily explained. This chapter aims to encourage colleagues capable of creating the desired physical models.

Acknowledgements

This chapter mostly summarizes the results of research performed by the Group of Microscopy and Spectroscopy of Surfaces at the Institute of Scientific Instruments of the CAS in Brno, headed by Dr. Ilona Müllerová, who began CL mode implementation in an SEM and continuously manages the project. The presented data and micrographs have mostly been collected by former Ph.D. students of the group: Dr. Miloš Hovorka, Dr. Šárka Mikmeková, Dr. Eliška Mikmeková, Dr. Filip Mika, Dr. Zuzana Pokorná, and Dr. Ivo Konvalina. Thanks are also due to Dr. Aleš Paták, Mr. Jiří Sýkora, and Mr. Pavel Klein. Some of the samples have been provided by Dr. Jana Nebesářová (Biology Centre, České Budějovice), Professor Kenji Matsuda (University of Toyama, Japan), Professor Bohuslav Mašek (University of Western Bohemia, Plzeň), and Dr. Baowen Liu (UNIST, Ulsan, South Korea). In recent years, the program has been supported by the project TE01020118 of the Technology Agency of the Czech Republic (Competence Centre: Electron Microscopy) and, in part, by MEYS CR (LO1212).

Author details

Luděk Frank*

Address all correspondence to: ludek@isibrno.cz

Institute of Scientific Instruments, Czech Academy of Sciences, Brno, Czech Republic

References

[1] Brüche E, Johannson H. Elektronenoptik und Elektronenmikroskop. Naturwissenschaften. 1932;20:353–358. DOI: 10.1007/BF01504926

[2] Recknagel A. Theorie des elektrischen Elektronenmikroskops für Selbststrahler. Zeitschrift für Physik. 1941;117:689–708. DOI:10.1007/BF01668875

[3] Zworykin VK, Hillier J, Snyder RL. A scanning electron microscope. ASTM Bulletin. August 1942:15–23. DOI: 10.1520/STP10082B

[4] Paden RS, Nixon WC. Retarding field scanning electron microscopy. Journal of Physics E: Scientific Instruments. 1968;1:1073–1080. DOI: 10.1088/0022-3735/1/11/305.

[5] Müllerová I, Lenc M. The scanning very-low-energy electron microscopy (SVLEEM). In: Proceedings of the 2nd Workshop of the European Microbeam Analysis Society, Electron Microbeam Analysis, Mikrochimica Acta Supplement 12; May 1991; Dubrovnik. Wien: Springer; 1992. p. 173–177.

[6] Müllerová I, Frank L. Use of the cathode lens in scanning electron microscope for low voltage applications. Mikrochimica Acta. 1994;114/115:389–396. DOI: 10.1007/BF01244565

[7] Müllerová I, Frank L. Very low energy microscopy in commercial SEMs. Scanning. 1993;15:193–201. DOI: 10.1002/sca.4950150403

[8] Müllerová I, Frank L. Scanning low energy electron microscopy. In: Hawkes PW, editor. Advances in Imaging and Electron Physics, Vol. 128. Amsterdam: Elsevier; 2003. p. 309–443. DOI: 10.1016/S1076-5670(03)80066-6

[9] Müllerová I, Frank L. Very low energy scanning electron microscopy. In: Méndez-Vilas A, Diaz J, editors. Modern Research and Educational Topics in Microscopy. Badajoz: Formatex; 2007. p. 795–804.

[10] Frank L, Hovorka M, Konvalina I, Mikmeková Š, Müllerová I. Very low energy scanning electron microscopy. Nuclear Instruments and Methods in Physics Research Section A. 2011;645:46–54. DOI: 10.1016/j.nima.2010.12.214

[11] Müllerová I, Hovorka M, Mika F, Mikmeková E, Mikmeková Š, Pokorná Z, Frank L. Very low energy scanning electron microscopy in nanotechnology. International Journal of Nanotechnology. 2012;9:695–716. DOI: 10.1504/IJNT.2012.046749

[12] Frank L, Hovorka M, Mikmeková Š, Mikmeková E, Müllerová I, Pokorná Z. Scanning electron microscopy with samples in an electric field. Materials. 2012;5:2731–2756. DOI: 10.3390/ma5122731

[13] Jaklevic RC, Davis LC. Band signatures in the low-energy-electron reflectance spectra of fcc metals. Physical Review B. 1982;26:5391–5397. DOI: 10.1103/PhysRevB.26.5391

[14] Pokorná Z, Frank L. Mapping the local density of states by very-low-energy scanning electron microscope. Materials Transactions. 2010;51:214–218. DOI: 10.2320/matertrans.MC200921

[15] Pokorná Z, Mikmeková Š, Müllerová I, Frank L. Characterization of the local crystallinity via reflectance of very slow electrons. Applied Physics Letters. 2012;100:261602. DOI: 10.1063/1.4729879

[16] Frank L, Nebesářová J, Vancová M, Paták A, Müllerová I. Imaging of tissue sections with very slow electrons. Ultramicroscopy. 2015;148:146–150. DOI: 10.1016/j.ultramic.2014.10.009

[17] Nebesářová J, Vancová M. Preparation of different biological objects for low voltage electron microscope. In: Proceedings of the 16th International Microscopy Congress, Vol. 1; 3–8 September 2006; Sapporo. Sapporo: Publication Committee of IMC16; 2006. p. 500.

[18] Frank L, Mikmeková E, Müllerová I, Lejeune M. Counting graphene layers with very slow electrons. Applied Physics Letters. 2015;106:013117. DOI: 10.1063/1.4905221

[19] Beck S, Plies E, Schiebel B. Low-voltage probe forming columns for electrons. Nuclear Instruments and Methods in Physics Research Section A. 1995;363:31–42. DOI: 10.1016/0168-9002(95)00254-5

[20] Plies E, Degel B, Hayn A, Knell G, Neumann J, Schiebel B. Experimental results using a "low-voltage booster" in a conventional SEM. Nuclear Instruments and Methods in Physics Research Section A. 1999;427:126–130. DOI: 10.1016/S0168-9002(98)01560-5

[21] Frosien J, Plies E, Anger K. Compound magnetic and electrostatic lenses for low-voltage applications. Journal of Vacuum Science and Technology B. 1989;7:1874–1877. DOI: 10.1116/1.584683

[22] Lenc M, Müllerová I. Electron optical properties of a cathode lens. Ultramicroscopy. 1992;41:411–417. DOI: 10.1016/0304-3991(92)90220-E

[23] Lenc M, Müllerová I. Optical properties and axial aberration coefficients of the cathode lens in combination with a focusing lens. Ultramicroscopy. 1992;45:159–162. DOI: 10.1016/0304-3991(92)90047-N

[24] Lencová B. Electrostatic lenses. In: Orloff J, editor. Handbook of Charged Particle Optics. 1st ed. Boca Raton: CRC Press; 1997. p. 177–221.

[25] Frank L, Müllerová I. Strategies for low- and very-low-energy SEM. Journal of Electron Microscopy. 1999;48:205–219.

[26] Káňová J, Zobač M, Oral M, Müllerová I, Frank L. Corrections of magnification and focusing in a cathode lens-equipped scanning electron microscope. Scanning. 2006;28:155–163. DOI: 10.1002/sca.4950280304

[27] Mikmeková E, Frank L, Müllerová I, Li BW, Ruoff RS, Lejeune M. Study of multi-layered graphene by ultra low energy SEM/STEM. Diamond and Related Materials, in press. DOI: 10.1016/j.diamond.2015.12.012.

[28] Mikmeková E, Frank L. Examination of graphene with very slow electrons. In: Proceedings of the 6th Nanocon International Conference 2014; 5–7 November 2014; Brno. Brno: Tanger; 2015. p. 741–746.

[29] Frank L, Mikmeková Š, Pokorná Z, Müllerová I. Scanning electron microscopy with slow electrons. Microscopy and Microanalysis. 2013;19[S2]:372–373. DOI: 10.1017/S1431927613003851

[30] Matsuda K, Ishida Y, Müllerová I, Frank L, Ikeno S. Cube-phase in excess Mg-type Al-Mg-Si alloy studied by EFTEM. Journal of Materials Science. 2006;41:2605–2610. DOI: 10.1007/s10853-006-7819-6

[31] Matsuda K, Ishida Y, Müllerová I, Frank L, Ikeno S. Chemical analysis of the cube phase in Al-Mg-Si alloy by EFTEM. In: Proceedings of an International Conference on Solid-to-Solid Phase Transformations in Inorganic Materials 2005, Vol. 1; 29 May–3 June 2005; Phoenix. Warrendale: TMS; 2005. p. 371–376.

[32] Bauer E. Low energy electron microscopy. Reports on Progress in Physics. 1994;57:895–938. DOI: 10.1088/0034-4885/57/9/002

[33] Strocov VN, Starnberg HI. Absolute band-structure determination by target current spectroscopy: Application to Cu(100). Physical Review B. 1995;52:8759–8766. DOI: 10.1103/PhysRevB.52.8759

[34] Bartoš I, van Hove MA, Altman MS. Cu(111) electron band structure and channeling by VLEED. Surface Science. 1996;352–354:660–664. DOI: 10.1016/0039-6028(95)01204-4

[35] Pejchl D, Müllerová I, Frank L. Unconventional imaging of surface relief. Czechoslovak Journal of Physics. 1993;43:983–992. DOI: 10.1007/BF01595290

[36] Chang THP, Nixon WC. Electron beam induced potential contrast on unbiased planar transistors. Solid State Electronics. 1967;10:701–704. DOI: 10.1016/0038-1101(67)90099-8

[37] Sealy CP, Castell MR, Wilshaw PR. Mechanism for secondary electron dopant contrast in the SEM. Journal of Electron Microscopy. 2000;49:311–321.

[38] El Gomati MM, Wells TCR, Müllerová I, Frank L, Jayakody H. Why is it that differently doped regions in semiconductors are visible in low voltage SEM? IEEE Transactions on Electron Devices. 2004;51:288–292. DOI: 1109/TED.2003.821884

[39] Schönjahn C, Broom RF, Humphreys CJ, Howie A, Mentink SAM. Optimizing and quantifying dopant mapping using a scanning electron microscope with a through-the-lens detector. Applied Physics Letters. 2003;83:293–295. DOI: 10.1063/1.1592302

[40] Müllerová I, El Gomati MM, Frank L. Imaging of the boron doping in silicon using low energy SEM. Ultramicroscopy. 2002;93:223–243. DOI: 10.1016/S0304-3991(02)00279-6

[41] Rodenburg C, Jepson MAE, Bosch EGT, Dapor M. Energy selective scanning electron microscopy to reduce the effect of contamination layers on scanning electron microscope dopant mapping. Ultramicroscopy. 2010;110:1185–1191. DOI: 10.1016/j.ultramic.2010.04.008

[42] Mika F, Frank L. Two-dimensional dopant profiling with low-energy SEM. Journal of Microscopy. 2008;230:76–83. DOI: 10.1111/j.1365-2818.2008.01957

[43] Frank L, Müllerová I. The injected-charge contrast mechanism in scanned imaging of doped semiconductors by very slow electrons. Ultramicroscopy. 2005;106:28–36. DOI: 10.1016/j.ultramic.2005.06.004

[44] Delong A, Kolařík V, Martin DC. Low voltage transmission electron microscope LVEM-5. In: Proceedings of the 14th International Congress on Electron Microscopy, Vol. 1; 31 August–4 September 1998; Cancun. Bristol: IOP Publishing; 1998. p. 463–464.

[45] Drummy LF, Yang J, Martin DC. Low-voltage electron microscopy of polymer and organic molecular thin films. Ultramicroscopy. 2004;99:247–256. DOI: 10.1016/j.ultramic.2004.01.011

[46] Mikmeková E, Bouyanfif H, Lejeune M, Müllerová I, Hovorka M, Unčovský M, Frank L. Very low energy electron microscopy of graphene flakes. Journal of Microscopy. 2013;251:123–127. DOI: 10.1111/jmi.12049

[47] Seah MP, Dench WA. Quantitative electron spectroscopy of surfaces: A standard data base for electron inelastic mean free paths in solids. Surface and Interface Analysis. 1979;1:2–11. DOI: 10.1002/sia.740010103

[48] Fitting HJ, Schreiber E, Kuhr JC, von Czarnowski A. Attenuation and escape depths of low-energy electron emission. Journal of Electron Spectroscopy and Related Phenomena. 2001;119:35–47. DOI: 10.1016/S0368-2048(01)00232-8

[49] Warner JH, Schäffel F, Bachmatiuk A, Rümmeli MH. Graphene, Fundamentals and Emergent Applications. 1st ed. Amsterdam: Elsevier; 2013. Chapter 3. DOI: 10.1016/B978-0-12-394593-8.00001-1

[50] Hibino H, Kageshima H, Maeda F, Nagase M, Kobayashi Y, Yamaguchi H. Microscopic thickness determination of thin graphite films formed on SiC from quantized oscillation in reflectivity of low-energy electrons. Physical Review B. 2008;77:075413. DOI: 10.1103/PhysRevB.77.075413

[51] Feenstra RM, Srivastava N, Gao Q, Widom M, Diaconescu B, Ohta T, Kellogg GL, Robinson JT, Vlassiouk IV. Low-energy electron reflectivity from graphene. Physical Review B. 2013;87:041406. DOI: 10.1103/PhysRevB.87.041406

Chapter 4

Microstructure Evolution in Ultrafine-grained Magnesium Alloy AZ31 Processed by Severe Plastic Deformation

Jitka Stráská, Josef Stráský, Peter Minárik, Miloš Janeček and Robert Král

Additional information is available at the end of the chapter

http://dx.doi.org/10.5772/61611

Abstract

Commercial MgAlZn alloy AZ31 was processed by two techniques of severe plastic deformation (SPD): equal channel angular pressing and high pressure torsion. Several microscopic techniques, namely light, scanning and transmission electron microscopy, electron backscatter diffraction, and automated crystallographic orientation mapping were employed to characterize the details of microstructure evolution and grain fragmentation of the alloy as a function of strain imposed to the material using these SPD techniques. The advantages and drawbacks of these techniques, as well as the limits of their resolution, are discussed in detail. The results of microstructure observations indicate the effectiveness of grain refinement by severe plastic deformation in this alloy. The thermal stability of ultrafine-grained structure that is important for practical applications is also discussed.

Keywords: Magnesium, ECAP, HPT, grain refinement, thermal stability

1. Introduction

Due to its low density, magnesium alloys are very attractive materials for structural components in automotive, aerospace and other transport industries with the potential to replace steel or aluminium alloys in various applications [1]. Nevertheless, the use of magnesium alloys in more complex applications is limited because of the problems associated with poor corrosion and creep resistance and above all the low ductility. The limited ductility is a consequence of the hexagonal structure providing the lack of independent slip systems and the large difference in the values of the critical resolved shear stress in different slip systems.

Moreover, the strong deformation textures and stress anisotropy in magnesium alloys reduces significantly the variety of possible industrial applications.

The mechanical and other essential properties determining the application of magnesium alloys may be improved by refining the grain size to the submicrocrystalline or even nanocrystalline level. In the last three decades, a variety of new techniques have been proposed for the production of the ultra-fine grain (UFG) structures in materials. The common feature of all these techniques is the imposition of large straining and consequent introduction of very high density of lattice defects in the material resulting in exceptional grain refinement. Since these procedures introduce severe plastic deformation (SPD) to bulk solids, it became convenient to describe all of them as SPD processing. Several processes of SPD are now available but only two of them receiving the most attention at present time, in particular, equal channel angular pressing (ECAP) and high-pressure torsion (HPT) [2–5].

The practical applications of the UFG materials are limited due to low microstructure stability at elevated temperatures that complicates the processing of final products. Thermal stability depends on many variables, such as stacking fault energy of the material, processing, or properties of grain boundaries [6]. Microstructure stability can be improved by various alloying elements or composite reinforcements.

In order to understand the microscopic mechanisms of grain fragmentation during SPD processing, detailed characterization of the microstructure is needed. The objective of this review paper is to employ a wide variety of standard and enhanced microscopic techniques to characterize the microstructure evolution of the UFG magnesium alloy AZ31 by employing several microscopic techniques, in particular, light microscopy, scanning electron microscopy (SEM), transmission electron microscopy (TEM), electron backscatter diffraction (EBSD), and a new sophisticated microscopic method—automated crystallographic orientation mapping in a TEM (ACOM-TEM).

2. Experiment

The commercial magnesium alloy AZ31 (3 wt. % of Al, 0.8 wt. % of Zn, and 0.2 wt. % of Mn) was used in this investigation. Two most popular techniques of severe plastic deformation were employed for material processing and microstructure refinement, namely equal-channel angular pressing preceded by hot extrusion (EX-ECAP) and high-pressure torsion (HPT).

2.1. Equal-channel angular pressing

Equal-channel angular pressing (ECAP) is one of the most developed and also commercially used SPD procedures. ECAP was invented by Segal et al. in the 1970s and 1980s in the former Soviet Union [7]. Since its invention, ECAP has become well-known and widely used technique. Nowadays, ECAP is a commonly used SPD method applicable in many branches of industries. The main advantage of the ECAP technique is the same cross-sectional dimensions of the specimens before and after pressing. This fact allows repetitive pressing and the

http://dx.doi.org/10.5772/61611

accumulation of strain in the specimen. Furthermore, the ECAP is a quite simple process commonly used worldwide.

The ECAP die consists of two channels with the same cross-section. Generally, the ECAP die is characterized by two angles: Φ, which is formed by these two channels, and the angle Ψ that indicates the outer arc of curvature at the intersection of the two channels (see Figure 1).

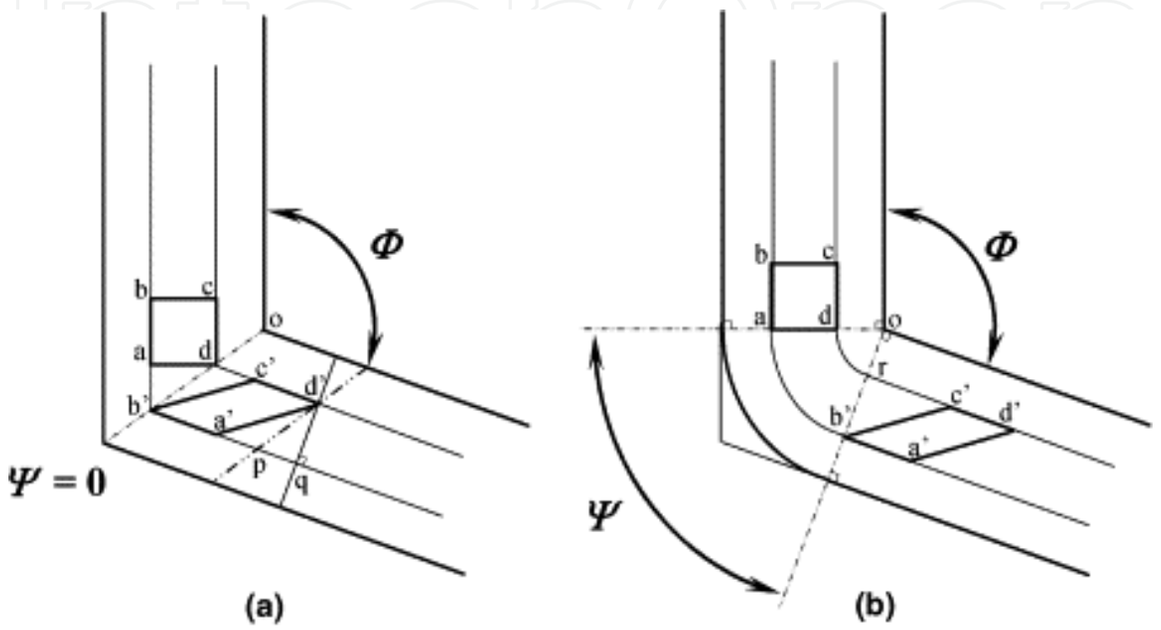

Figure 1. The scheme of pressing of the rectangular sample with the square cross-section through the ECAP die a) with $\Psi = 0$ and b) $\Psi \neq 0$ [8].

The specimen pressed through the ECAP die is deformed by a simple shear in the intersection point of the channels. The imposed strain in each ECAP pass is dependent primarily upon the angle Φ and, to a lesser extent, on the angle Ψ. It can be shown from the first principles that the imposed strain ε_N after N passes is given by a relation in the form [8]:

$$\epsilon_N = \frac{N}{\sqrt{3}}\left[2cotg\left(\frac{\Phi}{2}+\frac{\Psi}{2}\right)+\Psi cosec\left(\frac{\Phi}{2}+\frac{\Psi}{2}\right)\right]. \quad (1)$$

2.2. High-pressure torsion

High-pressure torsion (HPT) is another well-known SPD technique. In this method, the mechanical properties of a material are improved by a high pressure and concurrent torsional straining [9]. HPT was also for the first time applied to metals in the former Soviet Union in the 1980s [10]. The experimental setup of HPT is schematically illustrated in Figure 2.

The typical size of the disk-shaped sample varies from 10 to 20 mm in diameter and about 1 mm in thickness. A disk sample is placed between two anvils where it is subjected to a

compressive pressure of several GPa. Simultaneously, one of the anvils rotates and the torsional strain is imposed to the sample.

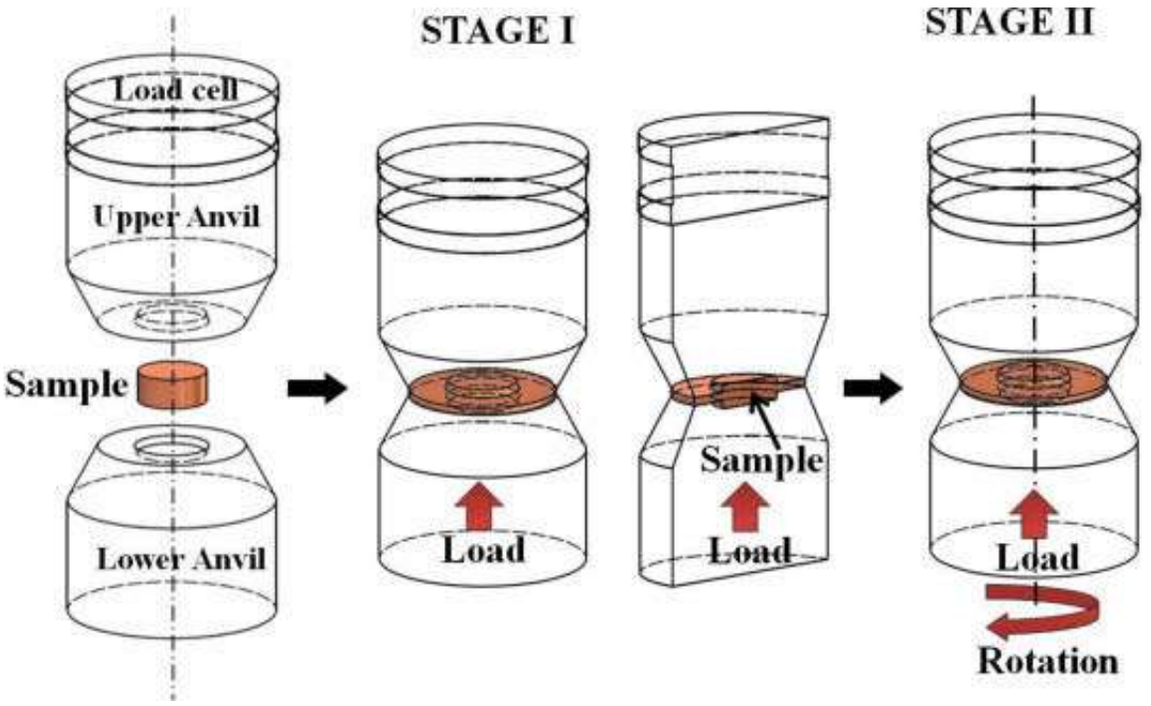

Figure 2. Schematic of the HPT device showing the set-up, compression stage (stage I), and compression-torsion stage (stage II) [11].

The total strain imposed by HPT in the sample can be calculated by different approaches. The first widely used approach (Hencky/Eichinger) can be expressed by the logarithmic relation [12]:

$$\epsilon = ln\left(\frac{2\pi N r h_0}{h^2}\right), \tag{2}$$

where N is the number of rotations, r represents the radius of the sample, and h_0 and h its initial and final thickness, respectively. The second possible approach (von Mises) using a model of simple torsion could be expressed by the following linear relation [13]:

$$\epsilon = \frac{\gamma}{\sqrt{3}} = \frac{r\theta}{\sqrt{3}h} = \frac{2\pi N r}{\sqrt{3}h}, \tag{3}$$

where γ is the shear strain and θ is the rotation angle.

However, the real strain generated in the workpiece during HPT may be different depending mainly on the die geometry and other factors. No unambiguous conclusion was adopted

http://dx.doi.org/10.5772/61611

whether the Hencky or von Mises strain describes better the total strain imposed by HPT. Finite element method (FEM) may be employed to analyze the plastic deformation distribution in specimens processed by HPT. Several authors [14, 15] have used the FEM technique to determine the stress distribution and other parameters, e.g., the influence of the coefficient of friction, torque, etc. Recently, Lee et al. [13] employed a combined analysis of FEM and the model of dislocation cell evolution to describe the local deformation in specimen processed by HPT. The results of this study are shown in Figure 3.

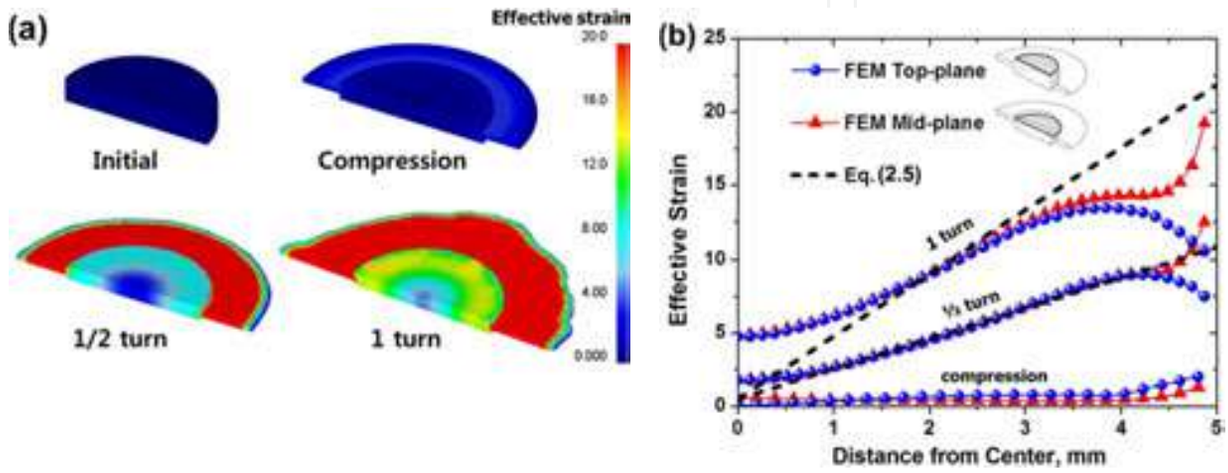

Figure 3: FEM simulation of effective strain imposed by HPT. a) The effective strain distribution of the as compressed specimen (N=0), the specimens after 1/2 (N=1/2) and 1 turn (N=1). b) The effective strain distribution throughout the thickness of the specimens N=0, N=1/2, and N=1 in the top and mid-plane showing the comparison of the FEM simulations [13] with the theoretical strain (Eq. 2.5).

Figure 3. FEM simulation of effective strain imposed by HPT. a) The effective strain distribution of the as compressed specimen (N=0), the specimens after 1/2 (N=1/2) and 1 turn (N=1). b) The effective strain distribution throughout the thickness of the specimens N=0, N=1/2, and N=1 in the top and mid-plane showing the comparison of the FEM simulations [13] with the theoretical strain (Eq. 2.5).

2.3. Material processing

2.3 Material processing

Prior to ECAP, the material was extruded at 350°C with an extrusion ratio of 22. ECAP pressing was performed at 180°C following route B_C, i.e., rotating the sample 90° between the individual passes, with the velocity of 50 mm/min. The angle Φ between two intersecting channels and the corner angle Ψ were 90° and 0°, respectively. Both channels have a square cross section of 10 mm × 10 mm. A series of specimens after N = 1, 2, 4, 8, and 12 passes was processed by ECAP. The as-extruded specimen was also included in the investigation as the reference material (marked N = 0).

Prior to ECAP, the material was extruded at 350°C with an extrusion ratio of 22. ECAP pressing was performed at 180°C following route B, i.e., rotating the sample 90° between the individual passes, with the velocity of 50 mm/min. The angle Φ between two intersecting channels and the corner angle Ψ were 90° and 0°, respectively. Both channels have a square cross section of 10 mm × 10 mm. A series of specimens after N = 1, 2, 4, 8, and 12 passes was processed by ECAP. The as-extruded specimen was also included in the investigation as the reference material (marked N = 0).

Prior to HPT, the material was homogenized at 390°C for 12 hours. After homogenization the disk specimens of the diameter of 19 mm and the thickness of 1-2 mm were cut from the billet. These specimens were processed by quasi-constrained HPT at room temperature for N = ¼, ½, 1, 5, and 15 rotations. In addition to samples subjected to various number N of HPT rotations, a sample that was pressed only between the anvils but not subjected to any HPT rotation (N = 0) was investigated as well.

Prior to HPT, the material was homogenized at 390°C for 12 hours. After homogenization the disk specimens of the diameter of 19 mm and the thickness of 1-2 mm were cut from the billet. These specimens were processed by quasi-constrained HPT at room temperature for N = ¼, ½, 1, 5, and 15 rotations. In addition to samples subjected to various number N of HPT rotations, a sample that was pressed only between the anvils but not subjected to any HPT rotation (N = 0) was investigated as well.

2.4 Experimental techniques of microstructure investigation

2.4.1 Light microscopy

The specimen surface for light microscopy observation needs to be plain, without impurities or scratches. Polypropylene was used for mounting the specimens for better manipulation. Mounted specimens were prepared by three consequent procedures: mechanical grinding, polishing, and etching. In the first step, the specimens were mechanically grinded on watered abrasive papers. Then the specimens were polished on a polishing disc with polishing suspension of grade 3 and 1 μm. Using this procedure, flat specimens with minimum surface scratches were obtained. Finally, the polished samples were etched by a diluted solution of picric acid. The time period of etching has to be optimized to attain the best possible

2.4. Experimental techniques of microstructure investigation

2.4.1. Light microscopy

The specimen surface for light microscopy observation needs to be plain, without impurities or scratches. Polypropylene was used for mounting the specimens for better manipulation. Mounted specimens were prepared by three consequent procedures: mechanical grinding, polishing, and etching. In the first step, the specimens were mechanically grinded on watered abrasive papers. Then the specimens were polished on a polishing disc with polishing suspension of grade 3 and 1 μm. Using this procedure, flat specimens with minimum surface scratches were obtained. Finally, the polished samples were etched by a diluted solution of picric acid. The time period of etching has to be optimized to attain the best possible visibility and no artefacts on the surface [16].

2.4.2. Electron Backscatter Diffraction (EBSD)

Electron backscatter diffraction (EBSD) is a microstructural crystallographic technique for determining crystallographic orientation. Texture, grain size and distribution, the misorientation and shape of individual grains, the types of grain boundaries, and many other microstructural features may be obtained from EBSD results.

The principle of the EBSD method is that the accelerated high-energy electrons interact with the atomic lattice of the crystalline material and form the so-called Kikuchi lines on the screen. The measurement is done automatically with a defined step. The formation of Kikuchi lines is caused by inelastic electron scattering. The inelastically scattered electron wavelength is slightly higher than the wavelength of elastically scattered electrons and the inelastic scattered electron intensity decreases with increasing scattering angle. In certain crystal orientations, some planes satisfy the Bragg condition (with diffraction angle θ), and the inelastically scattered electrons are Bragg diffracted. These electrons are called Kikuchi electrons. Kikuchi electrons move along conical surfaces whose top angle is equal ($\pi - 2\theta$) and the axis of diffraction planes is the normal line. Two hyperbolas are formed by the intersection of the conical surfaces and a screen. The hyperbolas seem like straight lines in the central part of the electron diffractogram and the distance between lines corresponds to the angle 2θ [16].

The SEM FEI Quanta 200 FX equipped with EDAX EBSD camera and OIM software was utilized for EBSD observations. A field emission gun (FEG) of a Schottky type was used as a source of electrons in the microscope. Beam voltage in the range from 500 V to 30 kV is applicable. The acceleration voltage employed was 10 kV.

The samples for EBSD investigation were first mechanically grinded on watered abrasive papers of grade 800, 1200, 2400, and 4000, respectively. Then the specimens were mechanically polished with diamond suspensions for water-sensitive materials of grade 3, 1, and ¼ μm, respectively. The final ion-polishing using a Gatan PIPS device was used to remove the surface layer influenced by polishing.

http://dx.doi.org/10.5772/61611

2.4.3. Transmission Electron Microscopy (TEM)

Transmission electron microscopy (TEM) is a technique that studies the local microstructure of the material using a beam of high-energy electrons. The specimens for TEM have to be very thin (≈ 100 nm depending on the acceleration voltage). An image is formed from the interaction of the electrons transmitted through the specimen and focused on a fluorescent screen or CCD camera.

The sample (thin foil) preparation consists of two steps: mechanical thinning and polishing. The type of polishing depends on the physical and chemical properties of the material.

The specimens of AZ31 alloy were first cut from the billet plane X (perpendicular to the extrusion direction) into slices of the thickness of approximately 1 mm. The slices were mechanically grinded from both sides to the thickness of 100 μm. The 3 mm diameter disks were cut out of the thin slices and dimpled from one side to the thickness of approximately 30 μm using the Gatan dimple grinder. This dimpling technique reduces electrolytic or ion polishing times and ensures that the ultra-thin area is done in the central part of the foil.

Ion polishing is used for materials that cannot be polished electrolytically. It is the case of many Mg alloys including AZ31. Ion polishing is a method of removing very fine quantities of the material. It uses an inert gas (argon) to generate a plasma stream that is emitted to the thinned area of the sample and removes the individual layers of the material. Acceleration energies vary usually from 2 to 4 keV. Ion beam always enters the sample. The penetration depth depends on the angle between the direction of the ion beam and the sample surface. The optimum conditions found for AZ31 were the following: acceleration voltage of 4 kV, angle of incidence of 4°, and room temperature. In the final stage the acceleration, voltage was reduced to 2 kV and the angle of incidence to 2°. The specimen preparation for TEM is finished when a small hole is formed in the foil and the surrounding area is thin enough to allow high-energy electrons to pass through the specimen. The schematic of the Precision Ion-Polishing System (PIPS) used for ion polishing is displayed in Figure 4 [17].

The microstructure observations were made with the TEM JEOL 2000FX at Charles University in Prague. The applied accelerated voltage was 200 kV.

2.4.4. Automated Crystallographic Orientation Mapping in a TEM (ACOM-TEM)

Automated crystallographic orientation mapping in a TEM (ACOM-TEM) is an effective technique for mapping phase and crystal orientation and an alternative to the well-known EBSD attachment SEM based on the Kikuchi lines. ACOM-TEM was first introduced by Schwarzer et al. [18]. This method of microstructural characterization represents a powerful tool especially for UFG or nano-grained materials where the limited resolution of SEM disallows EBSD scans. Its basic principle is similar to EBDS mapping—a selected area is scanned with defined step size and the electron diffraction patterns are collected using an external CCD camera. Off-line, every diffraction pattern is compared to the pre-calculated template and the best match is selected. The main difference with respect to EBSD is that point diffraction patterns are analyzed instead of Kikuchi lines, which significantly increases the

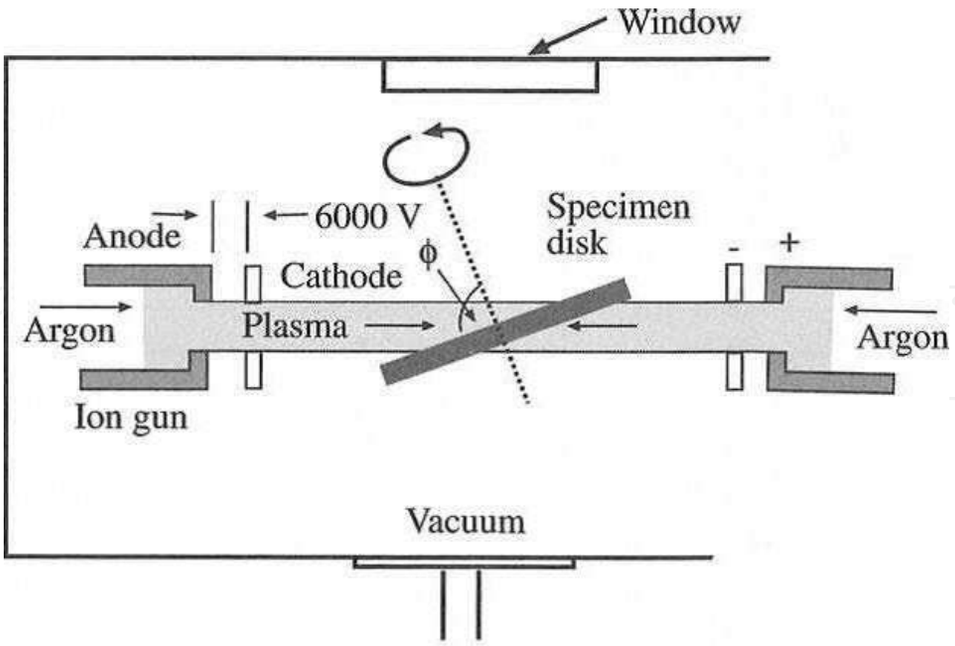

Figure 4. Schematic illustration of Precision Ion-Polishing System (PIPS).

precision of orientation determination. This type of ACOM-TEM device was developed in Grenoble by E. Rauch et al. [19, 20].

The experimental measurements were carried out using a TEM Philips CM200 equipped with a LaB_6 gun at 200 kV at Université Libre de Bruxelles in Belgium. For the data treatment, TSL OIM Analysis 5 was used.

3. Results and discussion

3.1. Microstructure evolution of AZ31 processed by ECAP

3.1.1. Light microscopy

The limited resolution of light microscopy allows to perform only overview images with no structure details. Typical examples of microstructure evolution of extruded specimen and the specimens processed by different number of ECAP passes (N) are shown in Figure 5. The extruded sample microstructure shown in Figure 5a consists of two types of grains—several large grains surrounded by many small grains. The microstructure developed only slightly after the first and the second ECAP pass, the bimodal structure is still observed (see Figure 5b). The microstructure changes begin to be significant in light microscopy after 4 ECAP passes. One can see in Figure 5c that the large grains become smaller. However, the bimodal structure is not observed after 8 and 12 ECAP passes. The homogeneous microstructure of sample after 12 ECAP passes is shown in Figure 5d.

http://dx.doi.org/10.5772/61611

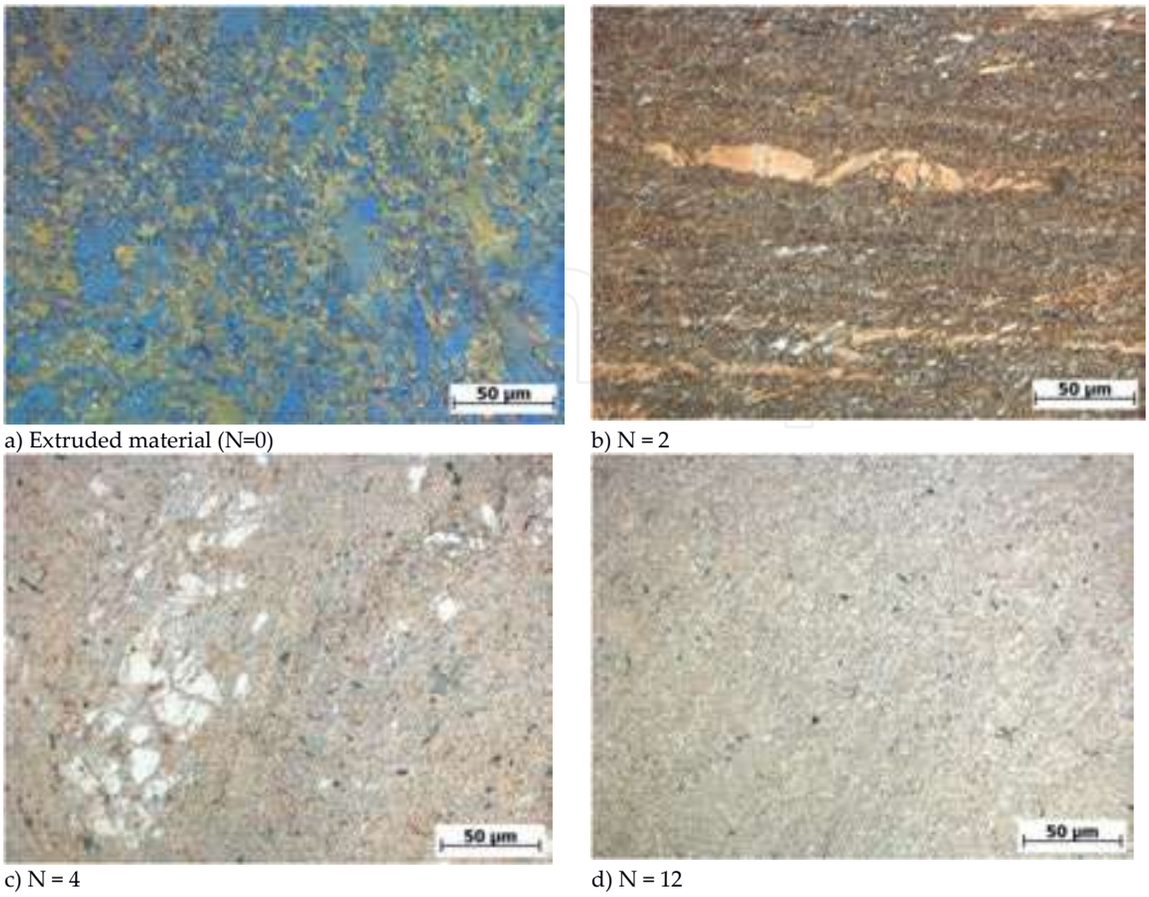

a) Extruded material (N=0) b) N = 2

c) N = 4 d) N = 12

Figure 5: The microstructure of the extruded and ECAPed AZ31 alloy.

Figure 5. The microstructure of the extruded and ECAPed AZ31 alloy.

3.1.2 EBSD

3.1.2. EBSD

Figure 6 shows the microstructure and texture of the extruded AZ31 alloy. The EBSD inverse pole figure map is in the extrusion direction (ED). The microstructure of the initial extruded bar (0P) consists of large grains of 50–100 ≈m mixed with relatively fine grains of 2–5 µm. Most grains have their crystallographic c-axis perpendicular to the extrusion direction (ED), i.e., <10.0> axes parallel to the ED, which is typically found after extrusion of Mg alloys [21].

Figure 6 shows the microstructure and texture of the extruded AZ31 alloy. The EBSD inverse pole figure map is in the extrusion direction (ED). The microstructure of the initial extruded bar (0P) consists of large grains of 50–100 ≈m mixed with relatively fine grains of 2–5 µm. Most grains have their crystallographic c-axis perpendicular to the extrusion direction (ED), i.e., <10.0> axes parallel to the ED, which is typically found after extrusion of Mg alloys [21].

Figure 7 presents the microstructure and texture of the sample after 1 ECAP pass (1P). EBSD measurements were carried out at the mid-part of the cross-section of the billet. Sample coordinate system, i.e., X–Y–Z directions, which is used for representing the texture are illustrated in Figure 7d.

As shown in Figure 7a, the bimodal distribution of grain sizes is still observed in the 1P sample. A new texture component that corresponds to the basal poles rotated about 40° from the initial orientation towards the pressing direction is visible in the 1P sample, Figure 7b. The mentioned orientation change, however, is observed mainly in large grains (grain size> 10 µm). Figure 7c presents the (0001) pole figure of grains smaller than 3 µm in the 1P sample. The intensity of the tilted basal poles is rather weak compared to the pole figure constructed using all grains.

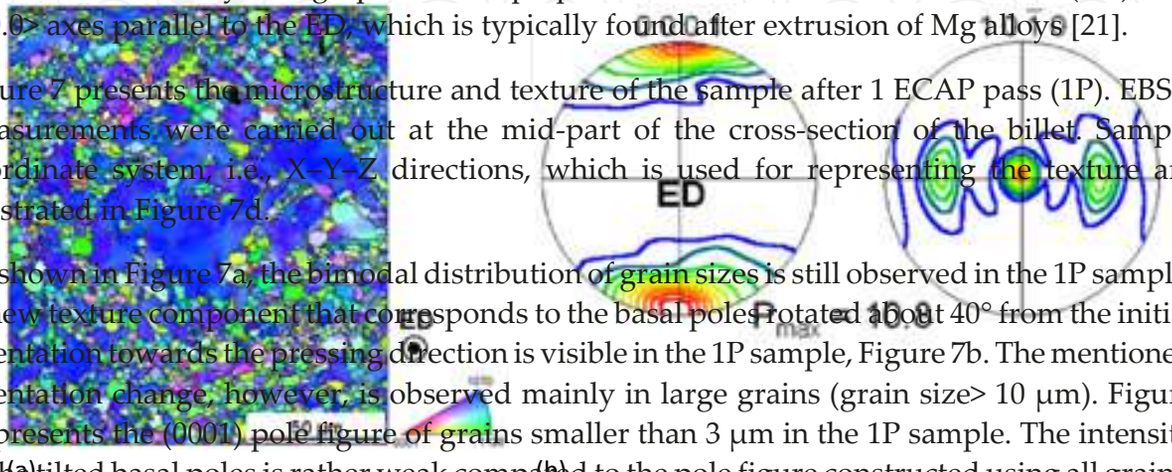

(a) (b)

Figure 6: (a) EBSD orientation map and (b) recalculated pole figures of the extruded bar (0P), measured at the cross-section transverse to the extrusion direction (contour level = 1, 2, …10).

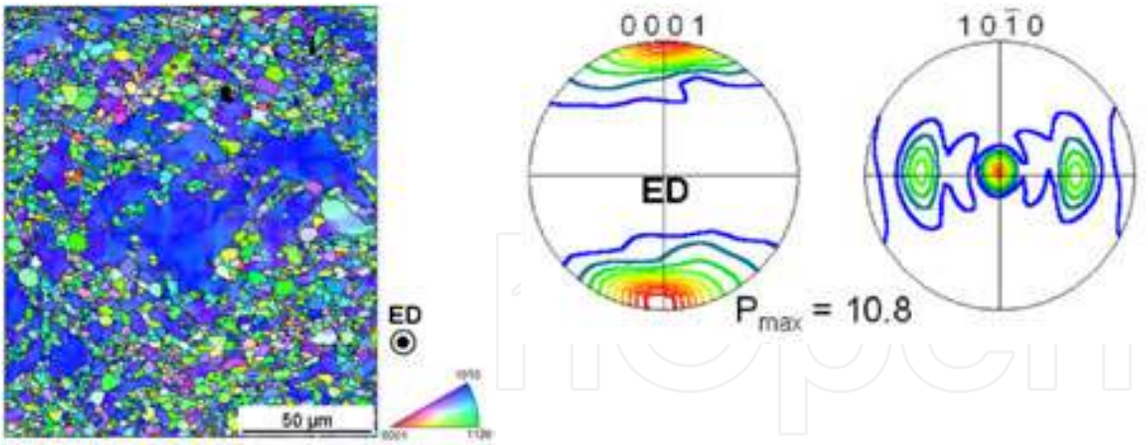

(a) (b)

Figure 6: (a) EBSD orientation map and (b) recalculated pole figures of the extruded bar (0P), measured at the cross-section transverse to the extrusion direction (contour level = 1, 2, …10).

Figure 6. (a) EBSD orientation map and (b) recalculated pole figures of the extruded bar (0P), measured at the cross-section transverse to the extrusion direction (contour level = 1, 2,...10).

Figure 7 presents the microstructure and texture of the sample after 1 ECAP pass (1P). EBSD measurements were carried out at the mid part of the cross-section of the billet. Sample coordinate system, i.e., X-Y-Z directions, which is used for representing the texture are illustrated in Figure 7d.

As shown in Figure 7a, the bimodal distribution of grain sizes is still observed in the 1P sample. A new texture component that is rotated about 40° from the initial orientation towards the pressing direction is visible in the 1P sample, Figure 7b. The mentioned orientation change, however, is observed mainly in large grains (grain size> 10 µm). Figure 7c presents the (0001) pole figure of grains smaller than 3 µm in the 1P sample. The intensity of the tilted basal poles is rather weak compared to the pole figure constructed using all grains. Moreover, the small grains (< 3 µm) with the tilted basal pole are found mainly in neighboring areas around large grains.

These results regarding distinct textures depending on the grain sizes indicate that the shear strain by the first ECAP pass is mainly accommodated within the large grains in accordance with the Hall–Petch relation. The discontinuity of material flow caused by the inhomogeneous deformation seems to be compensated by the occurrence of the dynamic recrystallization in the vicinity of grain boundaries of large grains, such that the sample could be deformed without failure.

Microstructural features of the sample after 2 ECAP passes (not shown here) are very similar to those after 1 ECAP pass, i.e., the bimodal distribution of grain sizes and the orientation change in large grains remain almost unchanged.

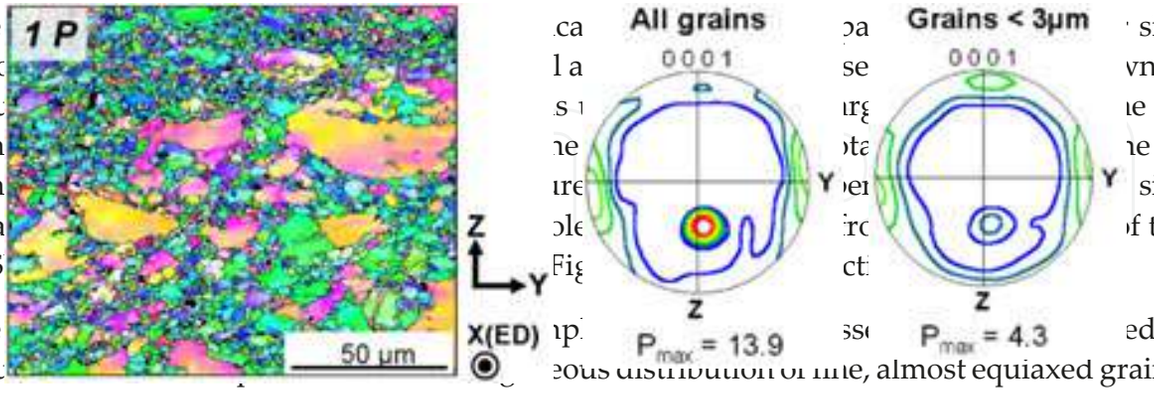

(a) (b) (c)

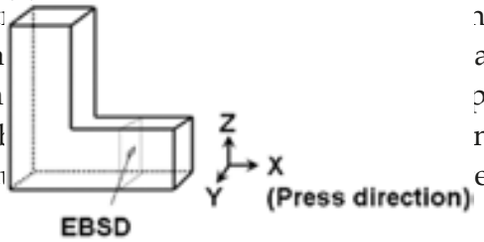

The ca pa size
becc l a se vn in
Figu s ı ırg ıe 1P
sam ne ota ne 4P
sam ure ber size
disa ole ırc of the
EBS Fig ct

The up ss ed in
Figu eous distribution of fine, almost equiaxed grains, i.e., no large grains are visible. Figure 9a shows grain agglomerates with different colors dist ndicates the heterogeneity in texture depending on the loca an be understood as a result of non-uniform deforma-tion ple passes [22]. Though the heterogeneous texture is visil ng to the inhomogeneity is small such that the main textu ed basal pole, Figure 9b.

to the pole figure constructed using all grains. Moreover, the small grains (< 3 μm) with the tilted basal pole are found mainly in neighboring areas around large grains.

These results regarding distinct textures depending on the grain sizes indicate that the shear strain by the first ECAP pass is mainly accommodated within the large grains in accordance with the Hall–Petch relation. The discontinuity of material flow caused by the inhomogeneous deformation seems to be compensated by the occurrence of the dynamic recrystallization in the vicinity of grain boundaries of large grains, such that the sample could be deformed without failure.

towards the pressing direction is visible in the 1P sample, Figure 7b. The mentioned orientation change, however, is observed mainly in large grains (grain size> 10 μm). Figure 7c presents the (0001) pole figure of grains smaller than 3 μm in the 1P sample. The intensity of the tilted basal poles is rather weak compared to the pole figure constructed using all grains. Moreover, the small grains (< 3 μm) with the tilted basal pole are found mainly in neighboring areas around large grains.

These results regarding distinct textures depending on the grain sizes indicate that the shear strain by the first ECAP pass is mainly accommodated within the large grains in accordance with the Hall–Petch relation. The discontinuity of material flow caused by the inhomogeneous deformation seems to be compensated by the occurrence of the dynamic recrystallization in the vicinity of grain boundaries of large grains, such that the sample could be deformed without failure.

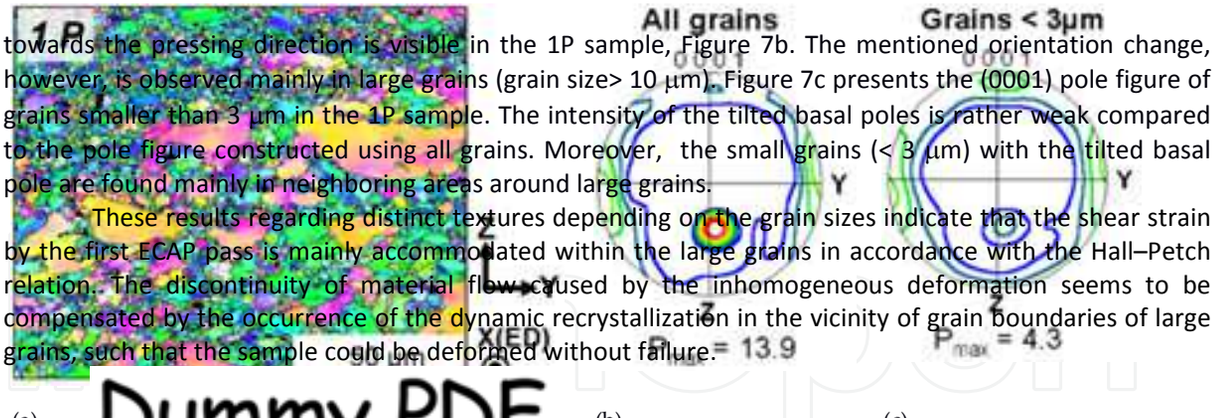

(a) (b) (c)

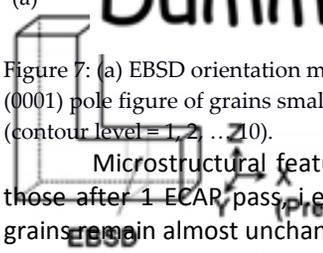

(d)

Figure 7: (a) EBSD orientation map of the sample after 1 ECAP pass, (b) (0001) pole figure calculated using all grains, (c) (0001) pole figure of grains smaller than 3 ◎m, and (d) the scheme of the geometry of specimens for EBSD measurements (contour level = 1, 2, .. 10).

Microstructural features of the sample after 2 ECAP passes (not shown here) are very similar to those after 1 ECAP pass, i.e., the bimodal distribution of grain sizes and the orientation change in large grains remain almost unchanged.

The amount of large grains decreases significantly after 4 ECAP passes (4P), and their size becomes smaller when compared to the initial and the 1P samples (see Figure 8). As shown in Figure 8a with dashed circles, the fine grains usually surround large grains. Unlike the 1P sample, the fine grains (<3 μm) have nearly the orientation of the rotated basal poles in the 4P sample (Figure 8c). It is clear that the texture heterogeneity depending on the grain size disappears after 4 ECAP passes, compared pole figures evaluated from the whole area of the EBSD measurement to that from fine grains, Figure 8b and c, respectively.

Figure 7: (a) EBSD orientation map of the sample after 1 ECAP pass, (b) (0001) pole figure calculated using all grains, (c) (0001) pole figure of grains smaller than 3 μm, and (d) the scheme of the geometry of specimens for EBSD measurements (contour level = 1, 2, .. 10).

Microstructural features of the sample after 2 ECAP passes (not shown here) are very similar to those after 1 ECAP pass, i.e., the bimodal distribution of grain sizes and the orientation change in large

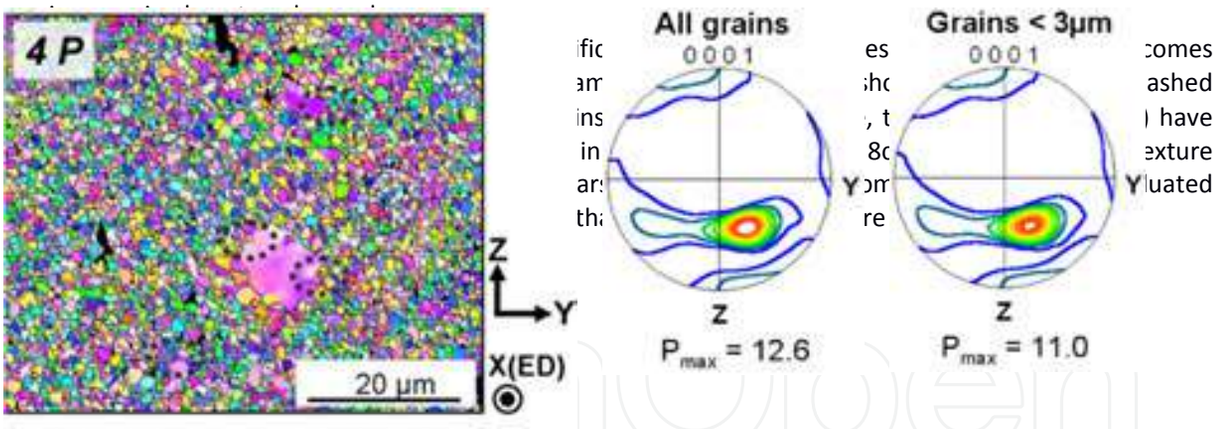

(a) (b) (c)

Figure 8: (a) EBSD orientation map of the sample after 4 ECAP passes, (b)(0001) pole figure of all grains, and (c) grains smaller than 3 ◎m (contour level = 1, 2, … 10).

Figure 8. (a) EBSD orientation map of the sample after 4 ECAP passes, (b)(0001) pole figure of all grains, and (c) grains smaller than 3 μm (contour level = 1, 2,.. 10).

The microstructure and the texture of the sample after 12 ECAP passes (12P) are presented in Figure 9. The 12P sample shows the homogeneous distribution of fine, almost equiaxed grains, i.e., no large grains are visible. Figure 9a shows grain agglomerates with different colors distributed along a diagonal line. This indicates the heterogeneity in texture depending on the location. This texture inhomogeneity can be understood as a result of non-uniform deformation along the ECAP billet after multiple passes [22]. Though the heterogeneous texture is visible, the fraction of the grains relating to the inhomogeneity is small such that the main texture component is found at the rotated basal pole, Figure 9b.

Figure 10 displays size distributions of fine grains (< 10 μm) after different numbers of ECAP passes. The grains smaller than 3 μm present in the extruded sample (0P) become finer (μ 1 lm) after the first ECAP pass. In subsequent ECAP passes no significant change in the size distribution in the range of the relatively fine grains is observed, while the area fraction of grains larger than 10 ≈m decreases gradually with ECAP passes, see Table 1.

The microstructure and the texture of the sample after 12 ECAP passes (12P) are presented in Figure 9. The 12P sample shows the homogeneous distribution of fine, almost equiaxed grains, i.e., no large grains are visible. Figure 9a shows grain agglomerates with different colors distributed along a diagonal line. This indicates the heterogeneity in texture depending on the locations. This texture inhomogeneity can be understood as a result of non-uniform deformation along the ECAP billet after multiple passes [22]. Though the heterogeneous texture is visible, the fraction of the grains relating to the inhomogeneity is small such that the main texture component is found at the rotated basal pole, Figure 9b.

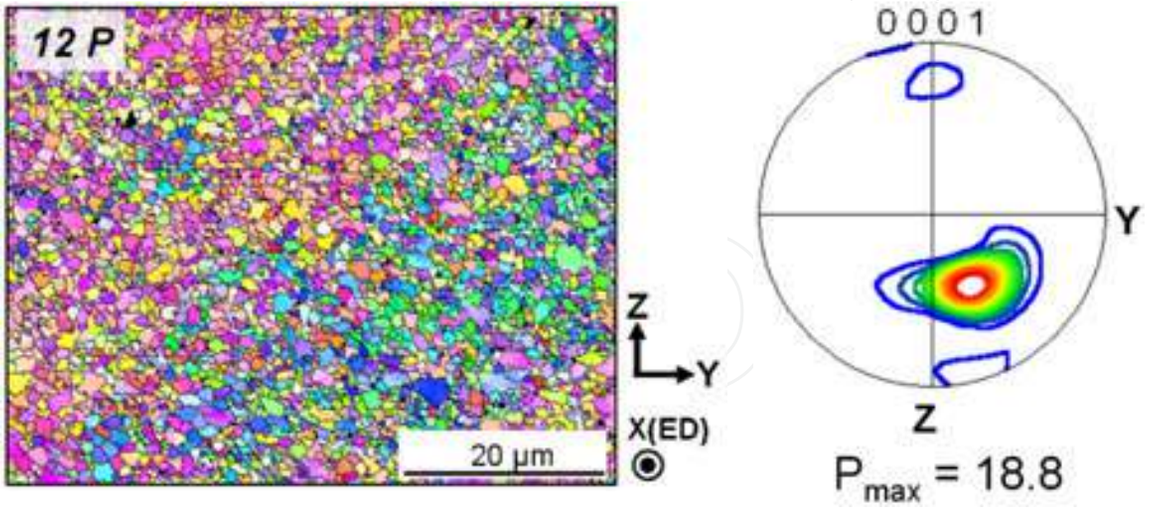

(a) (b)

Figure 9: (a) EBSD orientation map and (b) (0001) pole figure of the sample after 12 ECAP passes (contour level =

Figure 9. (a) EBSD orientation map and (b) (0001) pole figure of the sample after 12 ECAP passes (contour level = 1, 2,... 15).

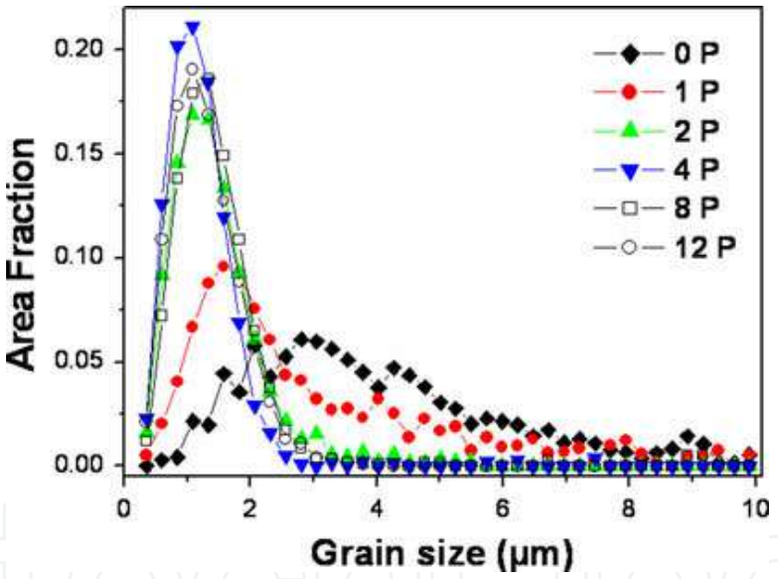

Figure 10. Grain size distributions within the range up to 10 μm and the area fraction of the grains larger than 10 μm as a function of the ECAP pass number.

No. ECAP Passes	0	1	2	4	8
Area fraction of grains > 10μm	17.9%	18.1%	7.9%	2.8%	None

Table 1. Area fraction of large grains as a function of ECAP pass number.

The variation in the fraction of low-angle boundaries (misorientation angle < 15°, LAGB) and high-angle boundaries (misorientation angle > 15°, HAGB) as a function of the ECAP pass

http://dx.doi.org/10.5772/61611

number is shown in Figure 11. The LAGB fraction increases after 1 ECAP pass to μ 50%, and is significantly reduced (≈20%) after two ECAP passes and remains almost unchanged as the number of passes increases above 2. This stabilization of the HAGB formed by 2 ECAP passes indicates that the dislocations generated by ECAP did not reach the level necessary for the formation of dislocation in the cell-structure and further development of HAGB. Since the ECAP in this study was carried out at moderate temperature, the dislocation annihilation process by dynamic recovery occurred fast enough such that the grains could not be further refined after 2 ECAP passes.

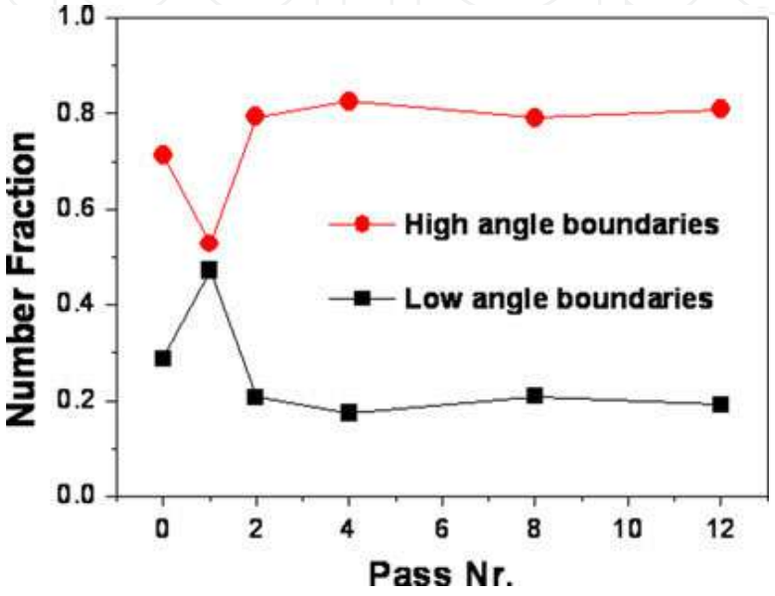

Figure 11. Variation of fraction of the HAGB and LAGB as functions of the ECAP pass number.

3.1.3. TEM

Additional detailed observations using TEM broadened the EBSD research. The samples for TEM observations were cut perpendicular to the pressing direction from the EX-ECAPed billet and prepared by mechanical grinding, dimpling, and ion polishing. The microstructure of extruded samples is bimodal—consists of large grains of 50–100 μm mixed with relatively fine grains of 2–5 μm. Figure 12 shows the area with smaller grains of the average size of few μm. Typical twins are clearly seen in several grains. The (0001) basal texture of individual grains in extruded magnesium alloy observed in EBSD measurements was confirmed by electron diffraction analysis. The contrast of individual grains on this micrograph with typical low-angle grain boundaries confirmed the analysis of diffraction patterns. The area of larger grains had a typical heavily deformed structure with high density of tangled dislocations (not shown here).

Figure 13 presents the microstructure of the specimen after 1 EX-ECAP pass. The bimodal character of the microstructure did not change after the first ECAP pass; the average grain size is only slightly smaller in comparison with the extruded material, see Figure 13a. However,

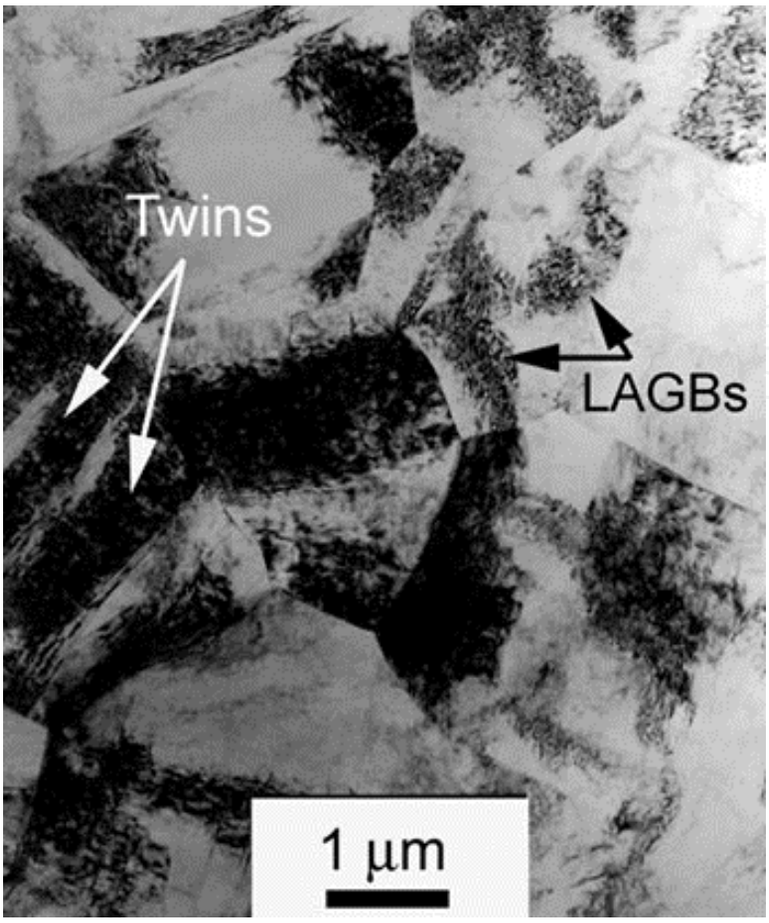

Figure 12. Transmission electron micrograph of extruded AZ31 alloy.

one significant difference between these two micrographs is observed, namely the character of grain boundaries. One can see many high-angle grain boundaries with typical thickness fringe band contrast confirming their almost equilibrium state in this micrograph. On the other hand, several grain boundaries remained in a non-equilibrium state with diffuse fuzzy contrast and many dislocations lying in a grain boundary plane were also observed. Several areas with high density of tangled dislocations with no or only exceptional signs of substructure formation were found in this specimen, see Figure 13b.

Subsequent TEM observation confirmed that the microstructure of EX-ECAPed samples changed only partly with increasing number of ECAP passes—fine grains were refined only slightly while the large grain zones were refined significantly. Typical microstructure of the sample processed by 2 EX-ECAP passes is shown in Figure 14.

Only fine grains of the average grain size in the submicrometer range were observed in the micrographs of the specimens after 8 and 12 ECAP passes. Figure 15a presents the typical microstructure of the sample after 8 passes. One can see that the grains in this micrograph are equiaxed, and the grain size is approximately 800 nm. This material has significantly lower density of dislocations and equilibrium grains boundaries. A few newly recrystallized very small grains with no dislocations and sharp equilibrium boundaries were also found in the

see many high-angle grain boundaries with typical thickness fringe band contrast confirming equilibrium state in this micrograph. On the other hand, several grain boundaries remain equilibrium state with diffuse fuzzy contrast and many dislocations lying in a grain boundary also observed. Several areas with high density of tangled dislocations with no or only excepti substructure formation were found in this specimen, see Figure 13b.

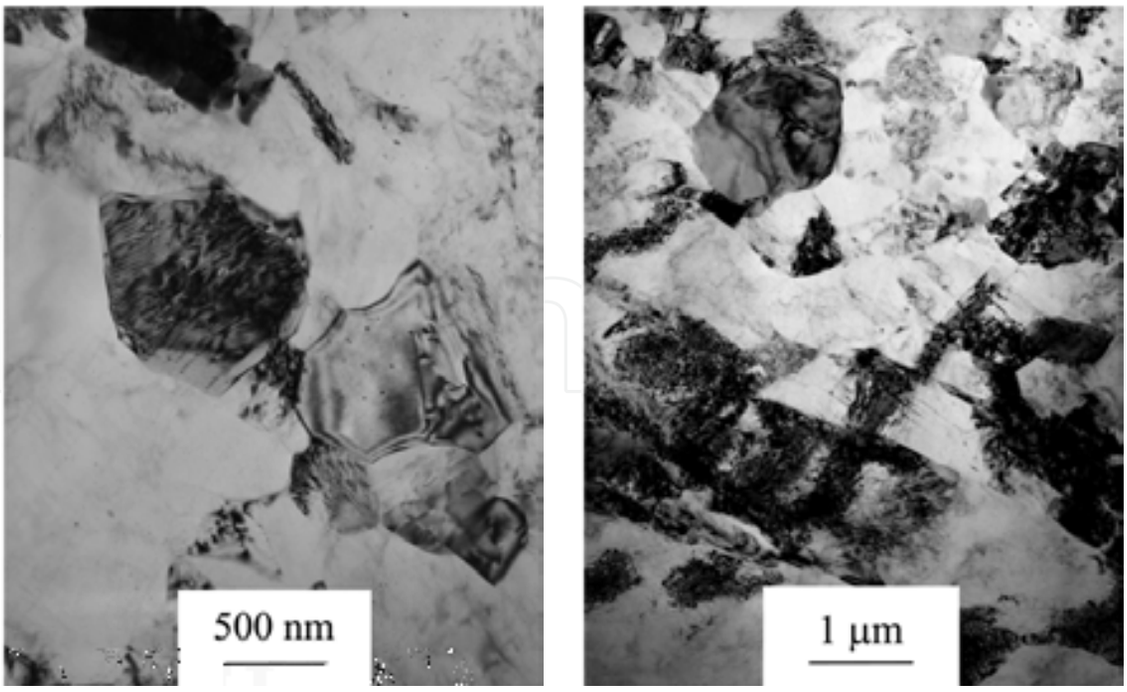

a) b)

Figure 13: Transmission electron micrographs of AZ31 alloy after extrusion and 1 pass of ECA equilibrium and HAGB region and (b) nonequilibrium GB region.

Figure 13. Transmission electron micrographs of AZ31 alloy after extrusion and 1 pass of ECAP, (a) equilibrium and HAGB region and (b) nonequilibrium GB region.

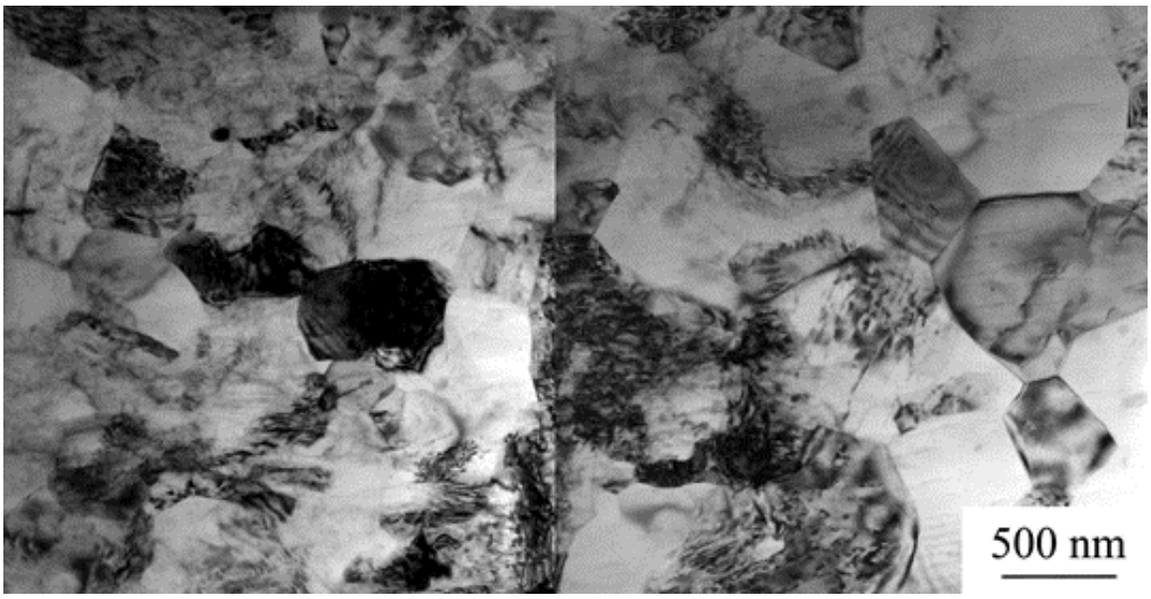

Figure 14. Transmission electron micrograph of AZ31 alloy after extrusion and 2 passes of ECAP.

microstructure after 8 and 12 passes of ECAP as seen in Figure 15b. TEM observations confirm the process of microstructure evolution and its fragmentation as observed by EBSD. In particular, large grains were continuously refined during subsequent ECAP pressing while the fine grains remained almost unchanged.

boundaries were also found in the microstructure after 8 and 12 passes of ECAP as seen in Figure 15b. TE
observations confirm the process of microstructure evolution and its fragmentation as observed by EBS
In particular, large grains were continuously refined during subsequent ECAP pressing while the fine grai
remained almost unchanged.

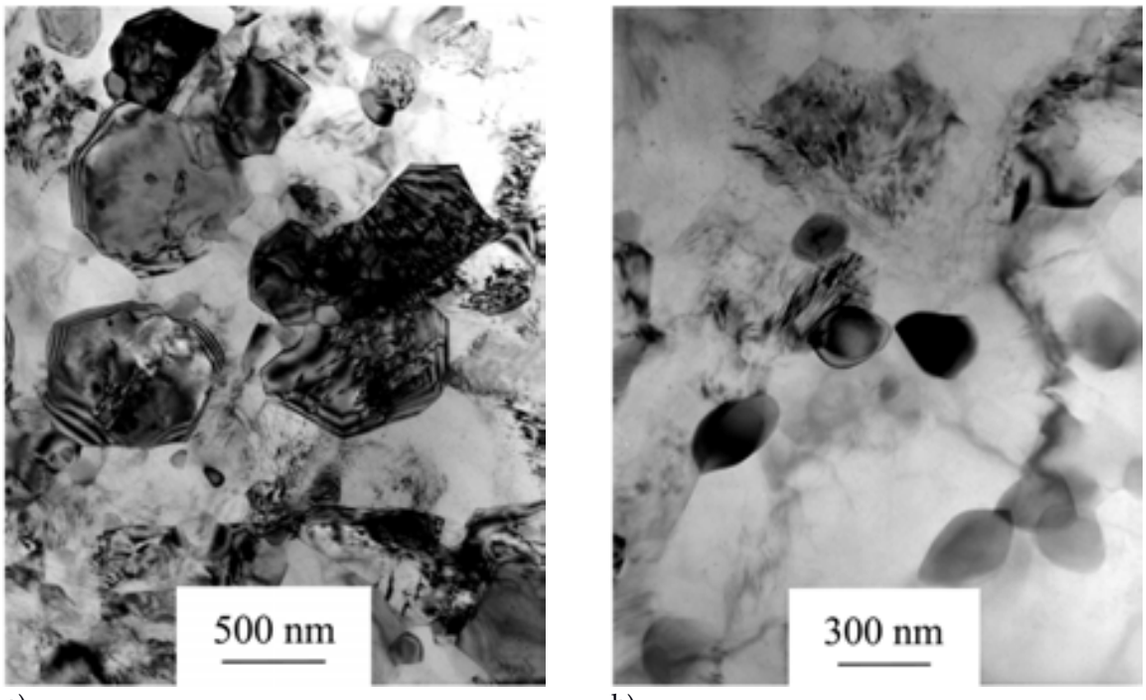

a) b)

Figure 15. Transmission electron micrograph of the AZ31 alloy (a) after 8 passes of EX-ECAP and (b) newly recrystallized small grains after 12 passes of EX-ECAP.

Figure 15. Transmission electron micrograph of the AZ31 alloy (a) after 8 passes of EX-ECAP and (b) newly recrystallized small grains after 12 passes of EX-ECAP.

3

Thermal stability of the UFG structure investigated by EBSD

3.2. Thermal stability of the UFG structure investigated by EBSD

Microscopic techniques, in particular EBSD, can also contribute to the characterization of thermal stability of the UFG structure. The maintenance of the fine-grained structure is of particular importance for many physical properties, e.g., the superplasticity, etc. [23, 24].

Series of specimens for thermal stability investigation were prepared by isochronal annealing at the temperatures 150–500°C for 1 h followed by water-quench. The samples after extrusion and 4 passes of ECAP were chosen as suitable materials because of their UFG and homogeneous microstructure with relatively high dislocation density (see also Figure 8a).

The microstructure and grain size distribution of the specimen in the initial non-annealed condition after extrusion and 4 passes of ECAP are shown in Figure 16a and 16b, respectively. The microstructure is homogeneous comprising of very fine grains with an average size of 0.9 μm. The microstructure and grain sizes of the samples after 1 h of isochronal annealing at 150°C and 170°C (not shown here) are very similar to the non-annealed specimen.

Inhomogeneous grain growth is observed at higher annealing temperatures as displayed at Figure 17. Some grains start to grow at temperatures of 190°C (Figure 17a) and 210°C (not shown here). The fraction of coarse grains increases with increasing annealing temperature. At the temperature of 250°C, some areas with original fine grains are still observed, see Figure 17b. However, the small grains are continuously disappearing at higher annealing temperatures and nearly no small grains are observed after annealing at 400°C, see Figure 17e. Please

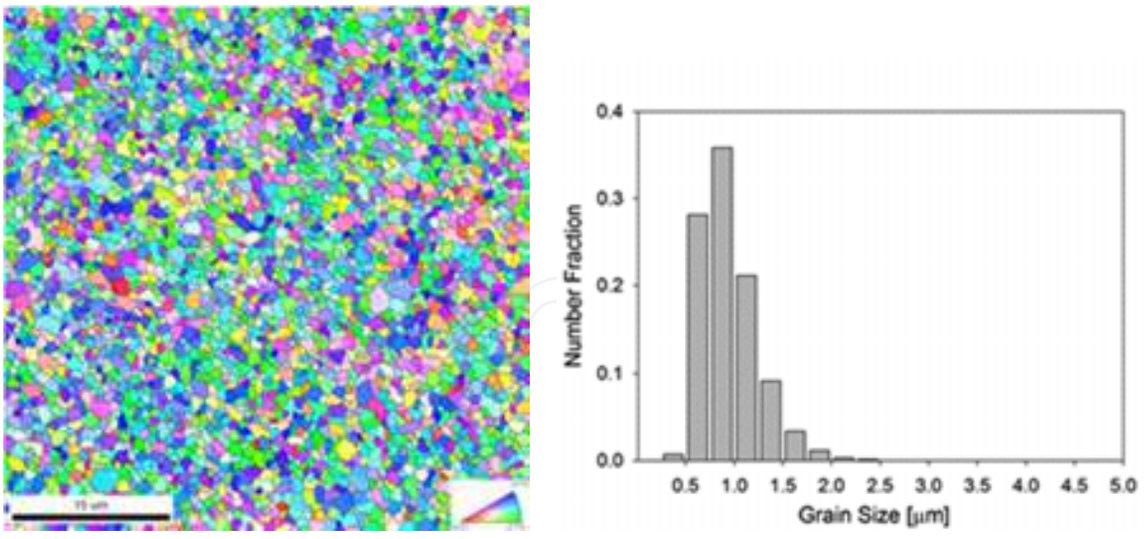

a) b)

Figure 16: Microstructure of the AZ31 sample after extrusion and 4 passes of ECAP, (a) inverse pole figure map and (b) grain size distribution.

Figure 16. Microstructure of the AZ31 sample after extrusion and 4 passes of ECAP, (a) inverse pole figure map and (b) grain size distribution.

Inhomogeneous grain growth is observed at higher annealing temperatures as displayed at Figure 17. Some grains start to grow at temperatures of 190°C (Figure 17a) and 210°C (not shown here). The fraction of coarse grains increases with increasing annealing temperature. At the temperature of 250°C, some areas with original fine grains are still observed, see Figure 17b. However, the small grains are continuously disappearing at higher annealing temperatures and nearly no small grains are observed after annealing at 300°C, see Figure 17c. Please note that magnification of Figure 17d and 17e is two times smaller than the magnification of the previous inverse pole figure maps; simultaneously, four times bigger area of the sample (100 × 100 µm) is depicted in Figure 17d and 17e. Microstructure of the specimens annealed at 450°C and 500°C was observed by light microscopy and displayed in Figure 18.

note that magnification of Figure 17d and 17e is two times smaller than the magnification of the previous inverse pole figure maps; simultaneously, four times bigger area of the sample (100 × 100 µm) is depicted in Figure 17d and 17e. Microstructure of the specimens annealed at 450°C and 500°C was observed by light microscopy and displayed in Figure 18.

Grain size distribution and average grain size of the samples studied by EBSD were calculated from at least 1000 grains to achieve better statistics. Statistical values from the samples studied by light microscopy were calculated from two [illegible] tha[illegible]s intersecting the [illegible]sco[illegible] analysis. The dep[illegible]ber[illegible] is plotted in Figu[illegible]an[illegible]culated from the [illegible]val[illegible]mmarized in Tab[illegible]

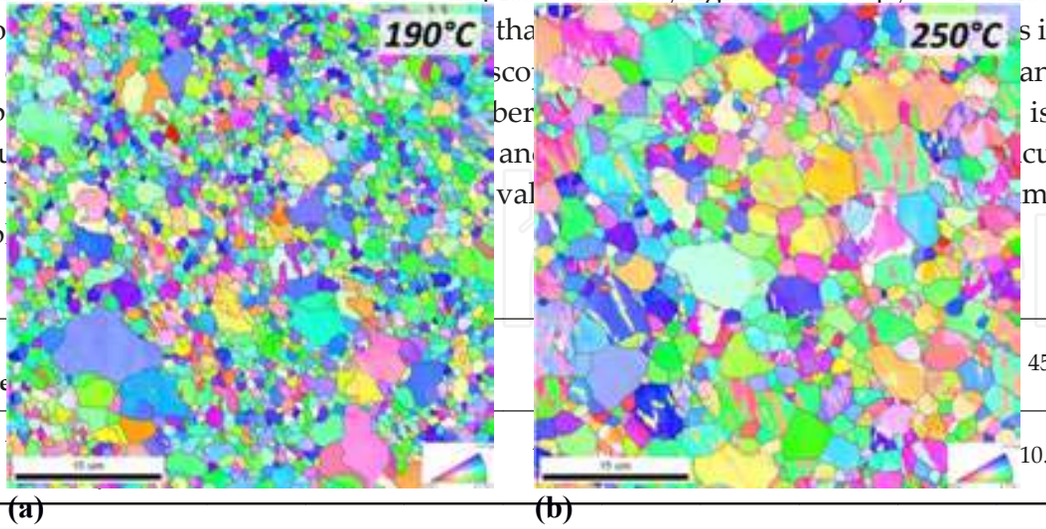

(a) (b)

te	450	500
	10.09	24.53

Table 2. The average grain sizes at different annealing temperatures.

Annealing twins observed after annealing at 250–400°C (see Figures 17b and 17e) were excluded from grain size calculations to achieve true grain size values (twin boundaries were ignored in grain size calculations, i.e., the twin is considered to be a part of the grain). All these

some areas with original fine grains are still observed, see Figure 17b. However, the small grains are continuously disappearing at higher annealing temperatures and nearly no small grains are observed after annealing at 400°C, see Figure 17e. Please note that magnification of Figure 17d and 17e is two times smaller than the magnification of the previous inverse pole figure maps; simultaneously, four times bigger area of the sample (100 × 100 μm) is depicted in Figure 17d and 17e. Microstructure of the specimens annealed at 450°C and 500°C was observed by light microscope and is displayed in Figure 18.

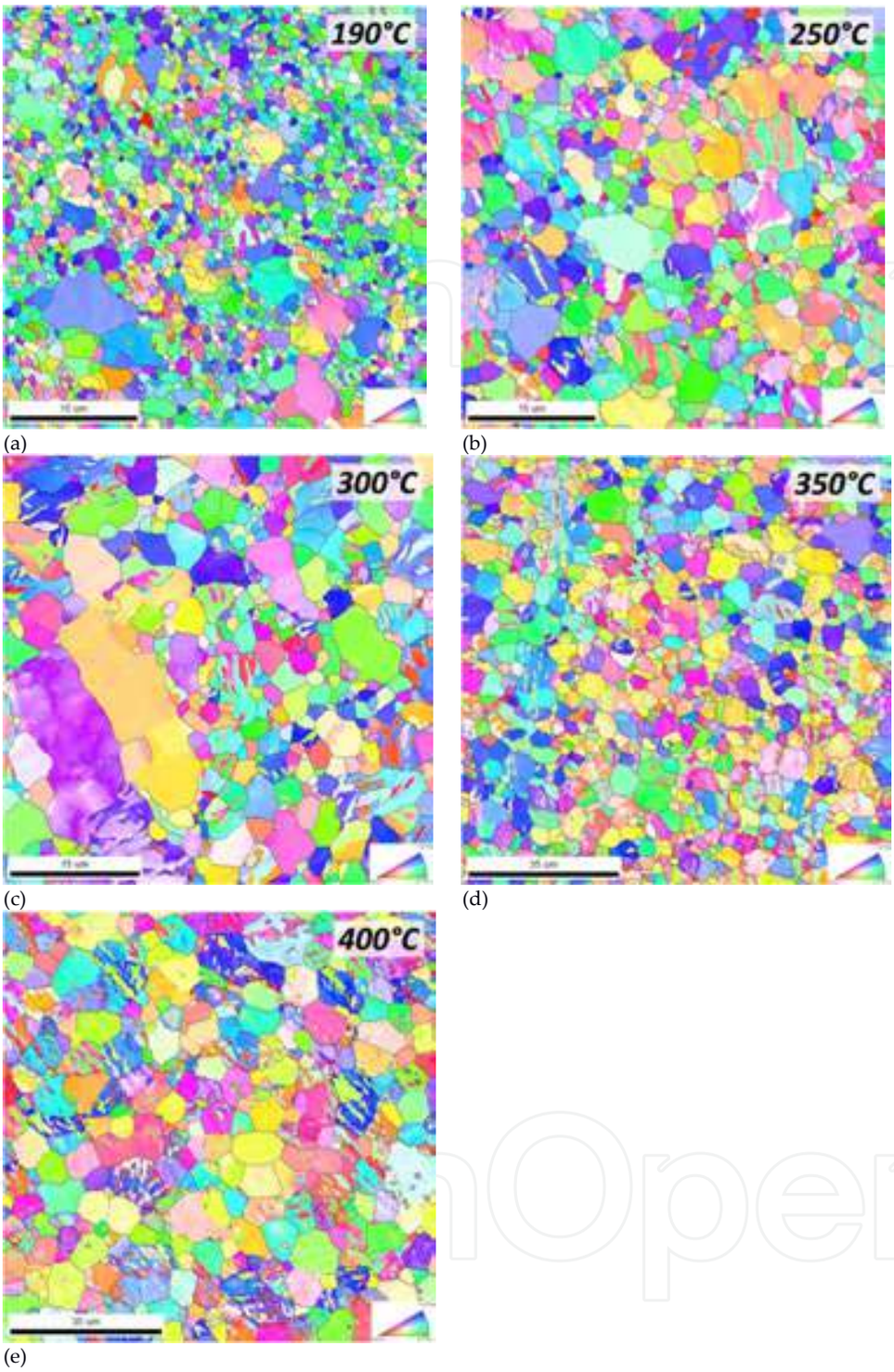

(a) (b) (c) (d) (e)

Figure 17: Microstructure of the AZ31 EX-ECAP specimen after 1 h of isochronal annealing at (a) 190°C,

Figure 17. Microstructure of the AZ31 EX-ECAP specimen after 1 h of isochronal annealing at (a) 190°C, (b) 250°C, (c) 300°C, (d) 350°C, and (e) 400°C (EBSD inverse pole figure maps).

twins were determined as the tensile twins with misorientation angle of 86° [25]. Twin fractions, fraction of twinned grains and the area fraction of twinned grains in samples after annealing at $T \geq 250$ °C are shown in Table 3.

http://dx.doi.org/10.5772/61611

Figure 18. Microstructure of the AZ31 EX-ECAP specimen after 1 h of isochronal annealing at (a) 450°C and (b) 500 °C (light microscope images).

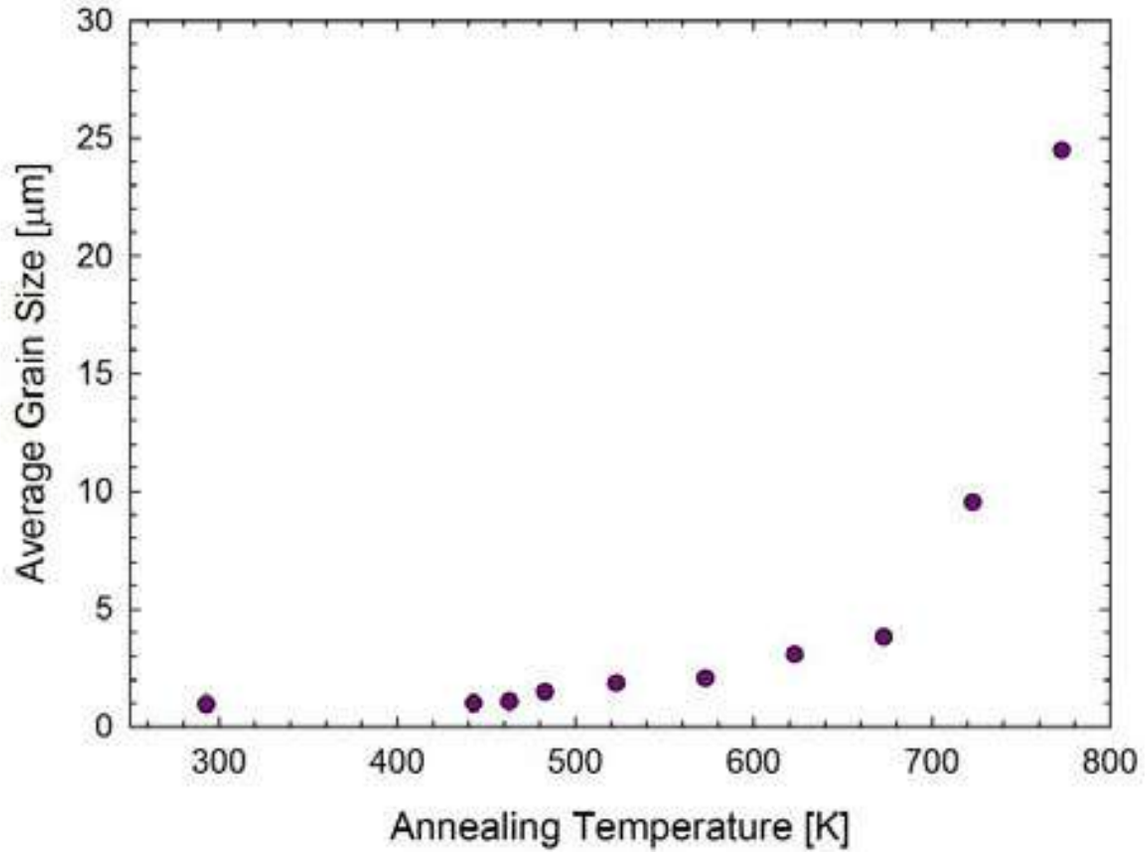

Figure 19. Dependence of the average grain size (number average, excluding twins) of the EX-ECAP AZ31 alloy on annealing temperature after 1 h of isochronal annealing process.

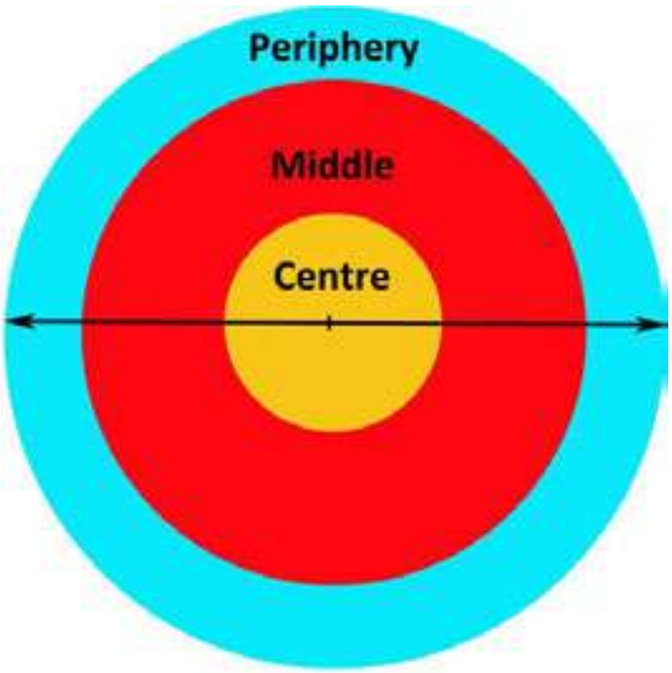

Figure 20. Schematic illustration of three different parts of the disks processed by HPT.

Annealing Temperature	250°C	300°C	350°C	400°C
Twin Fraction	0.13	0.12	0.16	0.14
Fraction of Twinned Grains	0.26	0.26	0.37	0.40
Area Fraction of Twinned Grains	0.55	0.52	0.60	0.71

Table 3. Twinning in isochronally annealed EX-ECAP AZ31 alloy.

3.3. Microstructure evolution in UFG AZ31 processed by HPT investigated by ACOM-TEM

The microstructure of the materials after SPD cannot be often observed by light microscopy because of their very small grain sizes. EBSD is usually a much better and suitable method in this case. However, even EBSD has some limitation in resolution or some "more local" method could be required for microstructure observations. This often occurs in specimens processed by high pressure torsion. This method proved to be more effective in grain refinement than the ECAP due to mainly much larger strains imposed on the HPT disk during processing and also lower temperatures of processing as compared to ECAP [2, 9]. TEM is a well-known technique that usually solves the problem. ACOM-TEM is a very sophisticated method, alternative to EBSD, which enables to study extremely fine-grained materials. We used this technique for microstructure observations of the most deformed parts of HPT specimens. Due to the inhomogeneous character of strain imposed to the material by HPT, disks processed by HPT could be divided into three parts: center, middle, and periphery (see Figure 20).

Due to relatively low imposed strain after one HPT rotation, EBSD is sufficient to be employed for microstructure observation. Figures 21a and 21b show deformed microstructures of the

http://dx.doi.org/10.5772/61611

central and middle parts of the specimen after 1 turn studied by EBSD. The areas investigated by EBSD could be relatively big—in our case it was the area 100 × 100 μm. The step size of these measurements was 100 nm. Figure 21a displays a heavily deformed microstructure of the central part of the specimen with a lot of multiple twinning. The microstructure of the middle part of the sample after 1 HPT rotation, shown in Figure 21b, consists of several large elongated grains with no twins and a lot of new grains of the average size of few microns.

The same middle part of this specimen was studied using ACOM-TEM and the typical results are displayed in Figure 22a. Measurements were done with step size 20 nm, which is five times smaller than the step size of the EBSD measurements. ACOM-TEM measurements confirmed heterogeneous microstructures with large elongated grains and a lot of small grains. The microstructure of the peripheral part (see Figure 22b) is homogeneous with very small grains only (≈ 100–300 nm).

The same middle part of this specimen was studied using ACOM-TEM and the typical results are displayed in Figure 22a. Measurements were done with step size 20 nm, which is five times smaller than the step size of the EBSD measurements. ACOM-TEM measurements confirmed heterogeneous microstructures with large elongated grains and a lot of small grains. The microstructure of the peripheral part (see Figure 22b) is homogeneous with very small grains only (≈ 100–300 nm).

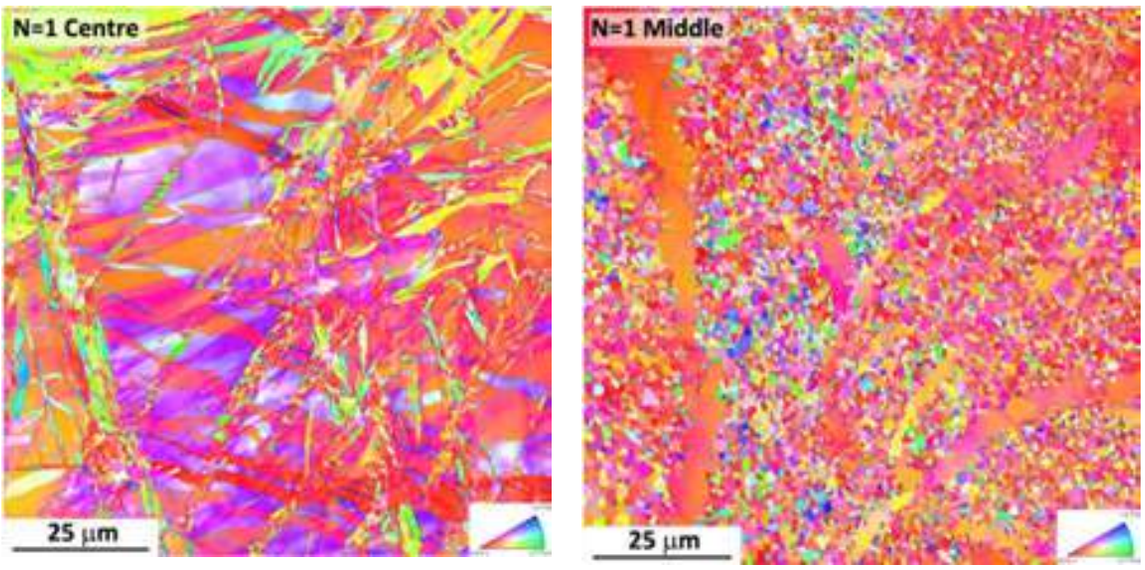

(a) (b)

Figure 21: EBSD IPF image of microstructure of the AZ31 sample after 1 turn of HPT, (a) central part and (b) middle part.

Figure 21. EBSD IPF image of microstructure of the AZ31 sample after 1 turn of HPT, (a) central part and (b) middle part.

The sample, after 5 turns of HPT, was investigated using ACOM-TEM in the middle and the peripheral part of the disk. The microstructure of the middle part (see Figure 23a) is comparable with the middle part of the sample after 1 HPT rotation; it consists of large elongated deformed grains and a lot of small grains surrounding the bigger grains. The microstructure of the peripheral part of the disk after 5 HPT turns, shown in Figure 23b, is composed mainly of very small grains. However, few remaining grains with the size of several microns could be still observed in the peripheral part. The ACOM-TEM is a very local method where the relatively small part of a thin foil could be investigated. Thus, the statistics of measurements of heterogeneous microstructure is not sufficient. Preparation and investigation of more TEM foils is needed to improve the statistics (despite each image consisting of observations at four different zones of a foil).

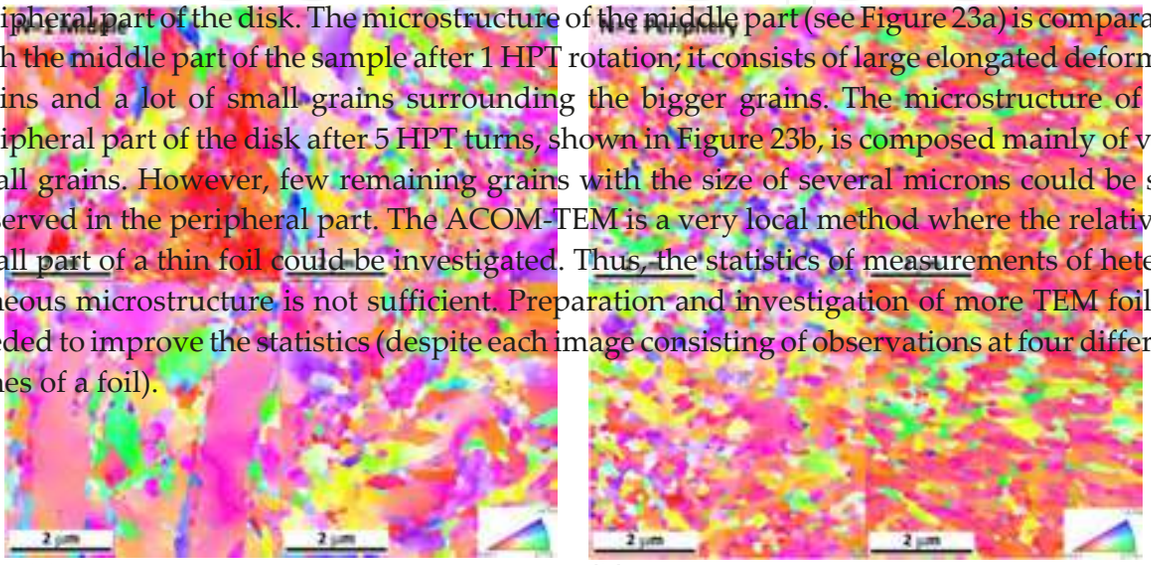

(a) **(b)**

Figure 22: ACOM-TEM image of the microstructure of the AZ31 sample after 1 turn of HPT, (a) middle part and (b) periphery.

Figure 21: EBSD IPF image of microstructure of the AZ31 sample after 1 turn of HPT, (a) central part and (b) middle part.

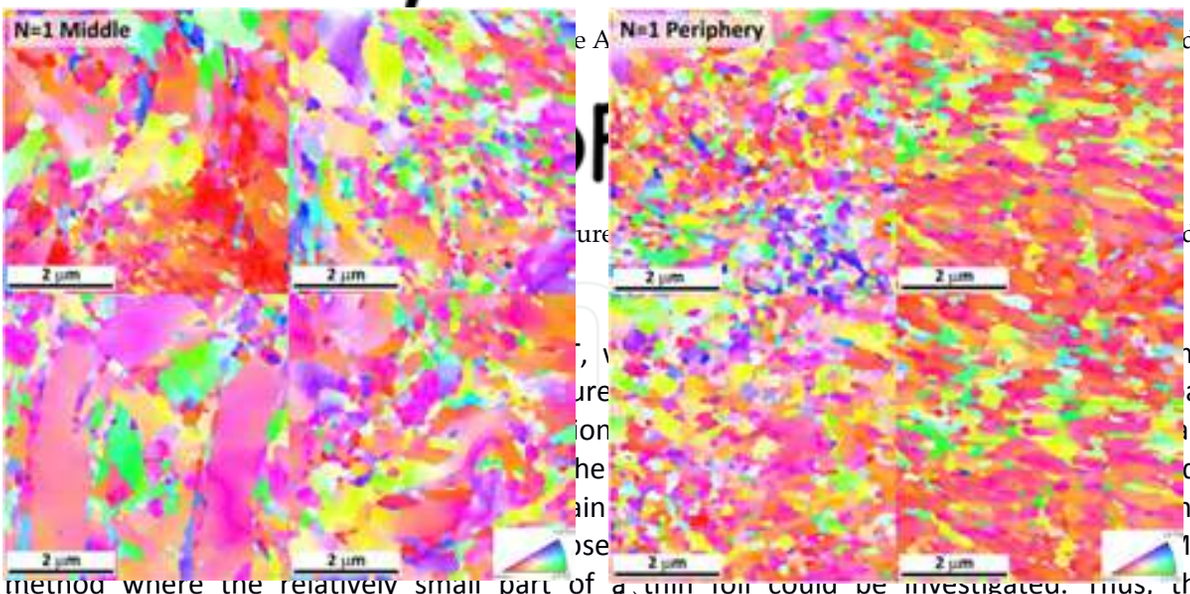

(a) (b)

Figure 22: ACOM-TEM image of the microstructure of the AZ31 sample after 1 turn of HPT, (a) middle part and (b) periphery.

The sample, after 5 turns of HPT, was investigated using ACOM-TEM in the middle and the peripheral part of the disk. The microstructure of the middle part (see Figure 23a) is comparable with the middle part of the sample after 1 HPT rotation; it consists of large elongated deformed grains and a lot of small grains surrounding the bigger grains. The microstructure of the peripheral part of the disk after 5 HPT turns, shown in Figure 23b, is composed mainly of very small grains. However, few remaining grains with the size of several microns could be still observed in the peripheral part. The ACOM-TEM is a very local method where the relatively small part of a thin foil could be investigated. Thus, the statistics of measurements of heterogeneous microstructure is not sufficient. Preparation and investigation of more TEM foils is needed to improve the statistics (despite each image consisting of observations at four different zones of a foil).

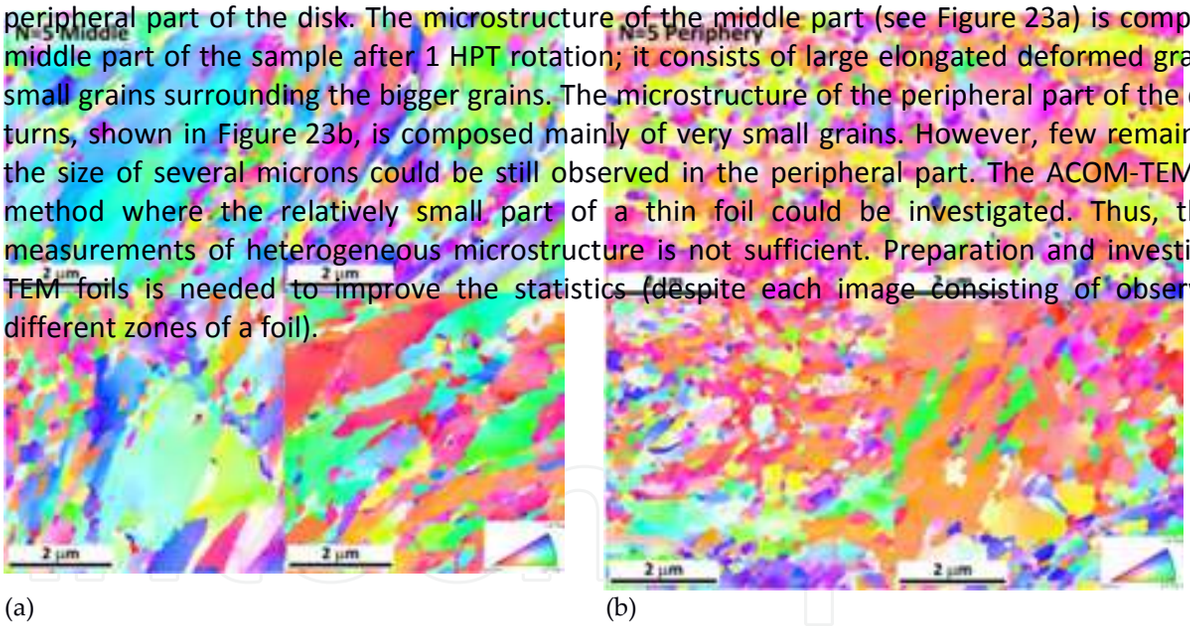

(a) (b)

Figure 23: ACOM-TEM image of the microstructure of the AZ31 sample after 5 turns of HPT, (a) middle part and (b) periphery.

Figures 24a and 24b display the microstructure of the middle and peripheral part of the disk after 15 HPT rotations, respectively. The microstructure of both parts is more homogeneous than the microstructure of the same parts of the disk after 5 HPT turns.

Grain size distributions of extremely fine grained microstructure of the peripheral parts of the disks after 1 and 15 HPT rotations (see Figure 25) show that about 60%, and nearly 70%, of

Figure 23: ACOM-TEM image of the microstructure of the AZ31 sample after 5 turns of HPT, (a) middle part and (b) periphery.

http://dx.doi.org/10.5772/61611

Figures 24a and 24b display the microstructure of the middle and peripheral part of the disk after 15 HPT rotations, respectively. The microstructure of both parts is more homogeneous than the microstructure of the same parts of the disk after 5 HPT turns.

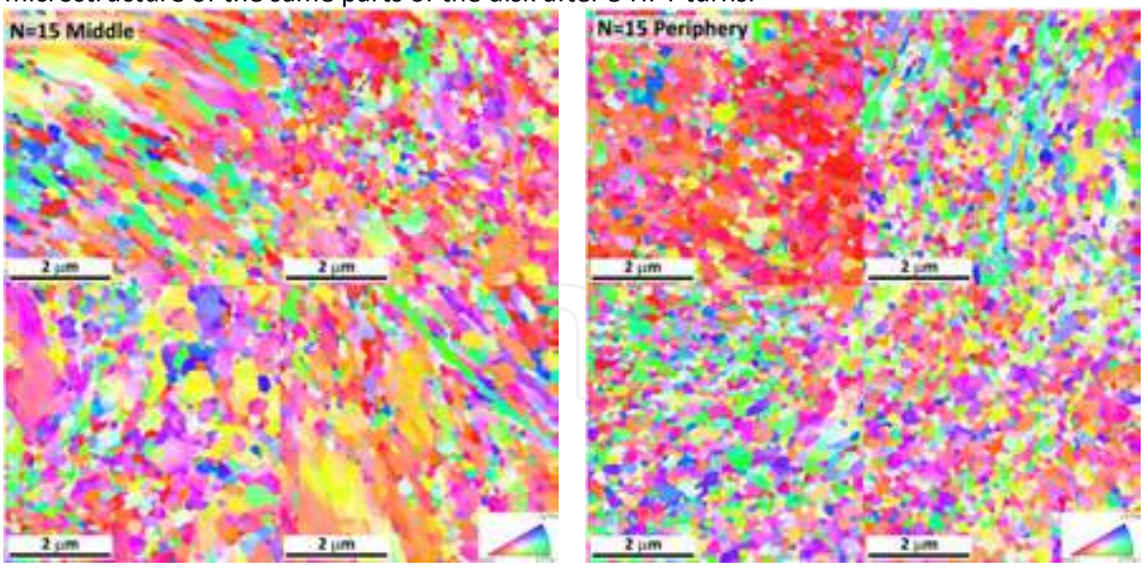

(a) (b)

Figure 24: ACOM-TEM image of the microstructure of the AZ31 sample after 15 turns of HPT, (a) middle

Figure 24. ACOM-TEM image of the microstructure of the AZ31 sample after 15 turns of HPT, (a) middle part and (b) periphery.

grains, respectively, have a diameter of 100–200 nm that proves clearly the efficiency of grain refinement by HPT.

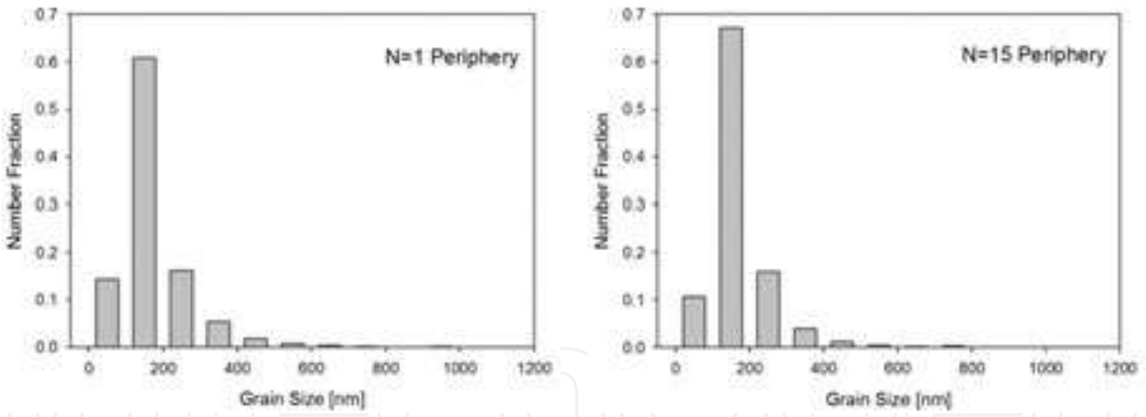

a) b)

Figure 25: Grain size distribution of the peripheral part of the disk after (a) 1 and (b) 15 rotations of HPT.

Figure 25. Grain size distribution of the peripheral part of the disk after (a) 1 and (b) 15 rotations of HPT.

4 Conclusions

4. Conclusions

Microstructure evolution in ultra-fine grained magnesium alloy AZ31 prepared by severe plastic deformation was investigated by several experimental techniques. The following conclusions may be drawn from this investigation:

- Due to limited resolution light microscopy may be employed to investigate the initial stages of grain fragmentation, i.e., the specimens processed by low number of ECAP passes or low number of HPT turns and especially in zones around the disk centers;
- EBSD proved to be a very powerful technique for the investigation of various stages of grain refinement. It allows to characterize not only the grain fragmentation, but also to determine other microstructural features as the grain size distribution and the grain boundary character distribution (the fraction of LAGBS vs. HAGBs), as well as the texture evolution with strain imposed to the material by ECAP and/or HPT;
- TEM allows to characterize the details of the microstructure, namely the dislocation arrangements, grain boundary character (equilibrium vs. nonequilibrium grain boundaries), twins, twin and other special boundaries, etc.;
- The special technique of ACOM-TEM may be used to characterize the terminal stages of grain

- Due to limited resolution light microscopy may be employed to investigate the initial stages of grain fragmentation, i.e., the specimens processed by low number of ECAP passes or low number of HPT turns and especially in zones around the disk centers;
- EBSD proved to be a very powerful technique for the investigation of various stages of grain refinement. It allows to characterize not only the grain fragmentation, but also to determine other microstructural features as the grain size distribution and the grain boundary character distribution (the fraction of LAGBS vs. HAGBs), as well as the texture evolution with strain imposed to the material by ECAP and/or HPT;
- TEM allows to characterize the details of the microstructure, namely the dislocation arrangements, grain boundary character (equilibrium vs. nonequilibrium grain boundaries), twins, twin and other special boundaries, etc.;
- The special technique of ACOM-TEM may be used to characterize the terminal stages of grain refinement (saturation) with grain sizes approaching to nanometer range (grain size < 100 nm), which is typical for peripheral zones of specimens processed by multiple turns of HPT;
- Complex microstructure characterization by different techniques of electron microscopy allows to understand the microscopic mechanisms of grain refinement, grain fragmentation, structure stability, as well as other important properties of ultra-fine grained materials processed by severe plastic deformation.

Acknowledgements

This work was financially supported by the Czech Science Foundation under the project GB14-36566G.

Author details

Jitka Stráská, Josef Stráský, Peter Minárik, Miloš Janeček* and Robert Král

*Address all correspondence to: janecek@met.mff.cuni.cz

Charles University in Prague, Department of Physics of Materials, Prague, Czech Republic

References

[1] Gupta M, Sharon NML. Magnesium, Magnesium Alloys, and Magnesium Composites. 1st ed. Wiley; 2011.

[2] Langdon TG. Twenty-five years of ultrafine-grained materials: Achieving exceptional properties through grain refinement. Acta Mater. 2013;61:7035–7059. DOI: 10.1016/j.actamat.2013.08.018.

[3] Estrin Y, Vinogradov A. Extreme grain refinement by severe plastic deformation: A wealth of challenging science. Acta Mater. 2013;61:782–817. DOI: 10.1016/j.actamat.2012.10.038.

[4] Horita Z, Matsubara K, Makii K, Langdon TG. A two-step processing route for achieving a superplastic forming capability in dilute magnesium alloys. Scr. Mater. 2002;47:255–260. DOI: 10.1016/S1359-6462(02)00135-5.

[5] Matsubara K, Miyahara Y, Horita Z, Langdon TG. Developing superplasticity in a magnesium alloy through a combination of extrusion and ECAP. Acta Mater. 2003;51:3073–3084. DOI: 10.1016/S1359-6454(03)00118-6.

[6] Gubicza J, Chinh NQ, Dobatkin SV, Khosravi E, Langdon TG. Stability of Ultrafine-Grained Microstructure in Fcc Metals Processed by Severe Plastic Deformation. Key Eng. Mater. 2011;465:195–198. DOI: 10.4028/www.scientific.net/KEM.465.195.

[7] Segal VM, Reznikov VI, Drobyshevskiy AE, Kopylov VI. Plastic working of metals by simple shear. Russ. Metall. 1981;1:99.

[8] Iwahashi Y, Wang J, Horita Z, Nemoto M, Langdon TG. Principle of equal-channel angular pressing for the processing of ultra-fine grained materials. Scr. Mater. 1996;35:143–146. DOI: 10.1016/1359-6462(96)00107-8.

[9] Zhilyaev AP, Langdon TG. Using high-pressure torsion for metal processing: Fundamentals and applications. Prog. Mater. Sci. 2008;53:893–979. DOI: 10.1016/j.pmatsci.2008.03.002.

[10] Kuznetsov RI, Bykov VI, Chernyshev VP, Pilyugin VP, Yefremov NA, Pasheyev AV. Plastic Deformation of Solid Bodies Under Pressure: 1. Equipment and Methods. Preprint 4/85, Sverdlovsk: IFM UNTs AN SSSR; 1985.

[11] Song Y, Yoon EY, Lee DJ, Lee JH, Kim HS. Mechanical properties of copper after compression stage of high-pressure torsion. Mater. Sci. Eng. A. 2011;528:4840–4844. DOI: 10.1016/j.msea.2011.02.020.

[12] Degtyarev MV, Chashchukhina TI, Voronova LM, Patselov AM, Pilyugin VP. Influence of the relaxation processes on the structure formation in pure metals and alloys under high-pressure torsion. Acta Mater. 2007;55:6039–6050. DOI: 10.1016/j.actamat.2007.04.017.

[13] Lee DJ, Yoon EY, Park LJ, Kim HS. The dead metal zone in high-pressure torsion. Scr. Mater. 2012;67:384–387. DOI: 10.1016/j.scriptamat.2012.05.024.

[14] Kim HS. Finite element analysis of high pressure torsion processing. J. Mater. Process. Technol. 2001;113:617–621. DOI: 10.1016/S0924-0136(01)00709-9.

[15] Yoon SC, Horita Z, Kim HS. Finite element analysis of plastic deformation behavior during high pressure torsion processing. J. Mater. Process. Technol. 2008;201:32–36. DOI: 10.1016/j.jmatprotec.2007.11.204.

[16] Vrátná J. Physical Properties of Ultrafine-grained Polycrystals of Magnesium Based Alloys [thesis]. Prague: Charles University in Prague; 2010.

[17] Williams DB, Carter CB. Transmission Electron Microscopy: A Textbook for Materials Science. 2nd ed. New York: Springer, 2009. ISBN 9780387765020.

[18] Schwarzer RA, Zaefferer S. An Inexpensive CCD Camera System for the Recording and On-Line Interpretation of TEM Kikuchi Patterns. Mater. Sci. Forum. 1994;157-162:189–194. DOI: 10.4028/www.scientific.net/MSF.157-162.189.

[19] Rauch EF, Veron M. Coupled microstructural observations and local texture measurements with an automated crystallographic orientation mapping tool attached to a TEM. Mater. Werkst. 2005;36:552–556. DOI: 10.1002/mawe.200500923.

[20] Rauch EF, Dupuy L. Rapid spot diffraction patterns idendification through template matching. Arch. Metall. Mater. 2005;50:87–99.

[21] Bohlen J, Yi SB, Swiostek J, Letzig D, Brokmeier HG, Kainer KU. Microstructure and texture development during hydrostatic extrusion of magnesium alloy AZ31. Scr. Mater. 2005;53:259–264. DOI: 10.1016/j.scriptamat.2005.03.036.

[22] Agnew SR, Mehrotra P, Lillo TM, Stoica GM and Liaw PK. Crystallographic texture evolution of three wrought magnesium alloys during equal channel angular extrusion. Mater. Sci. Eng. A. 2005;408:72–78. DOI: 10.1016/j.msea.2005.07.052.

[23] Valiev RZ, Islamgaliev RK, Alexandrov IV. Bulk nanostructured materials from severe plastic deformation. Prog. Mater. Sci. 2000;45:103–189. DOI: 10.1016/S0079-6425(99)00007-9.

[24] Valiev RZ, Estrin Y, Horita Z, Langdon TG, Zechetbauer MJ, Zhu YT. Producing bulk ultrafine-grained materials by severe plastic deformation. JOM. 2006;58:33–39. DOI: 10.1007/s11837-006-0213-7.

[25] Aghababaei R, Joshi SP. Micromechanics of tensile twinning in magnesium gleaned from molecular dynamics simulations. Acta Mater. 2014;69:326–342. DOI: 10.1016/j.actamat.2014.01.014.